Microstructure Control and Property Prediction in Inductively Coupled Selective Laser Melting

by

Aniket Chandrashekhar Jadhav

A dissertation submitted in partial fulfillment
of the requirements for the degree of
Doctor of Philosophy
(Mechanical Sciences and Engineering)
in the University of Michigan-Dearborn
2022

Doctoral Committee:

Professor Pravansu Mohanty, Chair
Assistant Professor Tanjore V Jayaraman
Associate Professor German Reyes-Villanueva
Professor Ya Sha Yi

Dedication

In the loving memory of Shankarrao M. Jadhav, Shailaja S. Jadhav, Shivajirao N Breed, Parvati S. Breed, Vishnu N. Kadam, Vijaya V. Kadam, Madhukar A. Rane & Ramesh M. Jadhav

Acknowledgements

I would like to express my gratitude to my Professor Dr. Pravansu Mohanty for giving me this unique opportunity to learn and work at the Additive Manufacturing Processes Laboratory in the field of Powder Bed Fusion Processes. I would also like to thank Dr.Tanjore V Jayaraman, Dr.German Reyes-Villanueva and Dr. Ya Sha Yi for agreeing to be a part of my Dissertation Committee and for their valuable time and support.

This study wouldn't be as constructive without the support of my teammate Ramcharan Palacode Visveswaran. It has been a pleasure working under his able guidance and support. I am thankful to Dr. Vikram Varadaraajan, Sharan Kumar Nagendiran and Neeraj Karmarkar for their constant support in every way possible. I would also like to thank Mayuresh Savargaonkar for his expertise and help in the field of Machine Learning.

My family has always been my strongest motivation for me to achieve greater things. I would like to thank each and every one of them for believing in me throughout this journey. My friends here in the states have been my extended family. I am grateful for their support for I would have not made it this far without all of them.

Last but not the least, I would like to thank my parents Mr. Chandrashekhar S Jadhav and Mrs. Uma C Jadhav for their unparalleled love and support. It is their blessings and belief that motivate me through thick and thin.

Thankyou *Tai* for everything you have been to me. I miss you everyday!

Table of Contents

List of Figures

List of Tables

Abstract

Metal Additive Manufacturing has earned significant industrial and research inclination in the recent years given faster production times and less wastage of material as compared to subtractive or traditional manufacturing. However, issues and concerns regarding quality, and process control, repeatability and consistency with Additive Manufacturing is still under works.

With more demand for tailored manufacturing suitable for specific end-applications, controlling physical properties by modifying process parameters or by inclusion of complimentary processes to Additive Manufacturing has been well known. This proposed study aims at delivering an effective way of addressing the thermal distribution control in a Powder Bed Fusion process for Selective Laser Melting of 316 Stainless Steel. Selective heating of the powder bed through a co-axially integrated induction system with a conventional laser setup is proposed based on literature survey, simulation data and baseline experiments. A system suitable for the proposed concept is designed, fabricated, and assembled. Extensive experimental trials are conducted to study the effect of the auxiliary heating source on the microstructure and the variation in physical properties of the built deposits.

Effect of controlling the cooling rate of the melt pool on the resulting mechanical properties is reviewed and discussed. Machine Learning to help predict physical properties and control the process flow given the complex nature, is proposed through a Digital Twin. Analytical data generated through the depositions is used to model the training and testing of the Digital Twin and

a framework for a more comprehensive study of the same is laid. A proof of concept demonstrating the use of induction in controlling the microstructure is achieved as well as initial efforts towards the Digital Twin are also successfully achieved.

Chapter 1 Introduction

Additive Manufacturing (AM), as defined by American Society for Testing and Materials (ASTM) is "a process of joining materials to make objects from 3D model data, usually layer upon layer, as opposed to subtractive manufacturing methodologies" [1]. A comparatively new process, it eliminates machining operations such as milling, lathing, turning, wire EDM, carving, etc. [2]. ASTM further categorizes Additive Manufacturing into seven categories. They are- Binder Jetting, Directed Energy Deposition, Material Extrusion, Material Jetting, Powder Bed Fusion, Sheet Lamination and vat photo polymerization [1]. The advantages of Additive Manufacturing over conventional manufacturing range from building economical products with no need for costly tools, molds or punches, automated manufacturing process with the use of readily available supplies, minimal to no post-process requirements with the potential to recycle waste material generated from the process, minimal inventory risk and improved working capital management [3].

Additive Manufacturing has undergone a 3-phase evolution. In the first, product designers, architects and artists started making use of AM for building prototypes, design mockups given the processes ease of manufacturing multiple copies of the same design at a relatively low cost. With the extensive use of less expensive materials, the manufacturing time and cost were significantly controlled and that led to improvement in the product development efficiency. The second phase saw the use of AM techniques in manufacturing finished goods. Also referred to as the "Direct

Digital Manufacturing", the second phase saw 3D printers being used for manufacturing goods to be used in test marketing. This included making multiple prototypes of different sizes, shapes and colors to be market tested. In the third phase, where we currently are, 3D printers are owned by the final consumers to meet their professional requirements [3].

Among the listed families of Additive Manufacturing processes, Powder Bed Fusion (PBF) is one of the first commercialized process and has been a subject of research interest. The L-PBF, a layer-by layer process capable of producing complex objects directly from a computer-generated geometry model, was first developed and commercialized by Dr.Carl Deckard and Dr.Joseph Beaman at the University of Texas, Austin in 1986. At the time when prototypes were manufactured at the machine shops using conventional manufacturing techniques like casting, machining, and joining, part production delays were a concern given the factors such as availability of skilled machinists, tool path planning, fixture procurement, etc. would take up most of the time. Additive Manufacturing redefined the principles of manufacturing techniques and approach with direct manufacturing of metal parts [4]. This has been one of the most important milestones of Additive Manufacturing changing it from a process for "rapid prototyping" to a process for "rapid manufacturing" [5]. Dr. Suman Das, in 1990, designed and built a high temperature laser powder bed fusion process system capable of withstanding temperatures as high as 1000° C. Through this system, he was able to manufacture fully dense miniature missile parts made from Ti6Al4V. The years 1999 to 2002 witnessed rapid growth of Additive Manufacturing in the medical field. Engineered organs and implants were 3D printed and coated with the patient's own cells with a minimal or no risk of rejection by the immune system. Mini functional kidney capable of filtering blood and diluting urine was developed using the 3D Printing technology. The first SLS (Selective Laser Sintering) machine was developed in 2006 whereas the Urbee, the world's first 3D printed

environment-friendly car was manufactured in 2011 following the first 3D Printed Aircraft completed in a mere 7-day period for a budget of £5000 in 2010 [6].

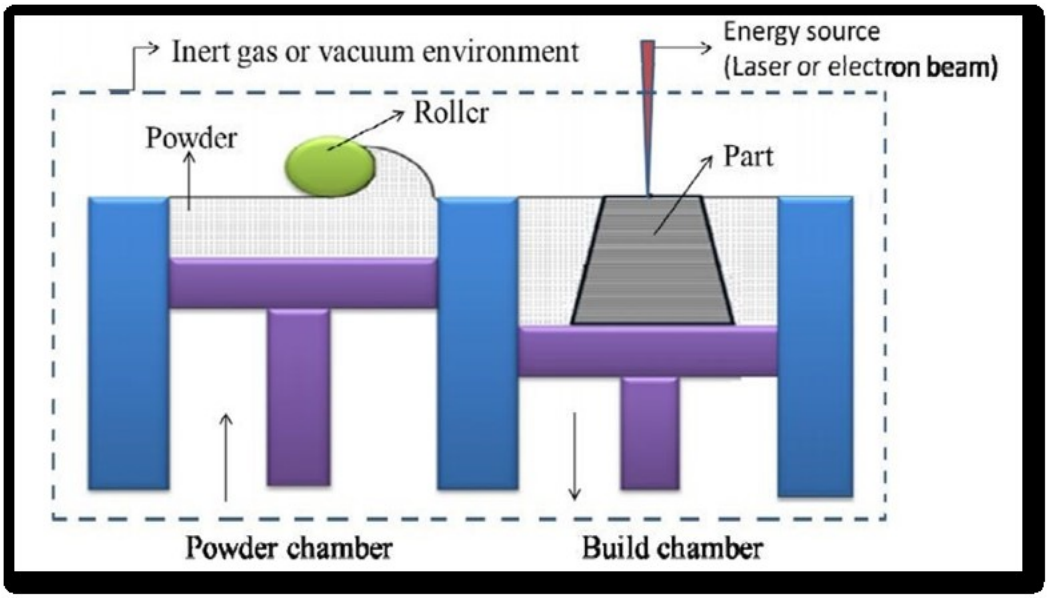

Figure 1.1: Powder Bed Fusion Process [7]

Figure 1.1 represents a typical Powder Bed Fusion process. All PBF processes have a basic working principle that makes use of a thermal source to consolidate the powder together. A new layer of powder is then spread uniformly on top of the previously fused powder layer by means of a roller and/or a spreader. This process is repeated until the desired part is completed in a layer-by-layer manner. Modifications to this basic principle in terms of the heating source under use, type of material, etc. are then made as per the application requirements. These modifications yield different names to the same underlying process of Powder Bed Fusion [1] [2]. Powder Bed Fusion is a process used to produce objects from powdered materials using one or more lasers to selectively fuse or melt the particles at the surface, layer by layer, in an enclosed chamber [1]. Consolidation in this process mainly can be induced in five different ways: solid state sintering, liquid state sintering, chemical induced binding, partial melting, and full melting. However, due

to the slow scan speed requirements of solid-state sintering to maintain high temperatures for sufficient time to allow diffusion of atoms, this technique proves inefficient with respect to economic manufacturing. Given these limitations, Powder Bed Fusion still allows high complexity components to be manufactured with the powder material acting as support structures throughout the process. Consolidation by partial melting (usually referred to as Selective Laser Sintering) and full melting (usually referred to as Selective Laser Melting) are mostly (±95%) used for processing Polyamide-12, a typical nylon grade. SLS and SLM for metal use is still limited to Stainless Steel and a few grades of Tool Steel whereas Titanium (Ti6Al4V) and Aluminum have started finding industrial applications [8]. Laser Sintering is a short-time interval process (in the order of milliseconds). As a result of this, binding through partial melting of the powder becomes a practical approach. This is done usually by applying a laser source to locally melt the lower melting point powder of the combination of the powder to be sintered. This, then wets the higher melting point powder and binds it together to form a sintered layer. Inter-particle wetting done by this two-phase approach is important to avoid the "balling phenomena" [9]. Due to the partial melting of the powder, a more liquid phase is present along the surface and the grain boundaries of the powder. This gives rise to a sintering-pool consisting of a liquid-solid mixture. The high intensity Laser with a faster scan speed causes rapid solidification of the sintering pool. As metal SLS demands higher temperatures for the binding mechanism to take place, severe oxidation might be involved. Oxidation of such laser processed metals leads to the formation of metal-ceramic interfaces in the sintering pool lowering the liquid-solid wettability and causing balling. Therefore, the balling phenomena occurs when the laser melted powder does not wet the remaining solid powder and the underlying substrate layer due to the contaminated layer of metal oxide present in the pool [10].

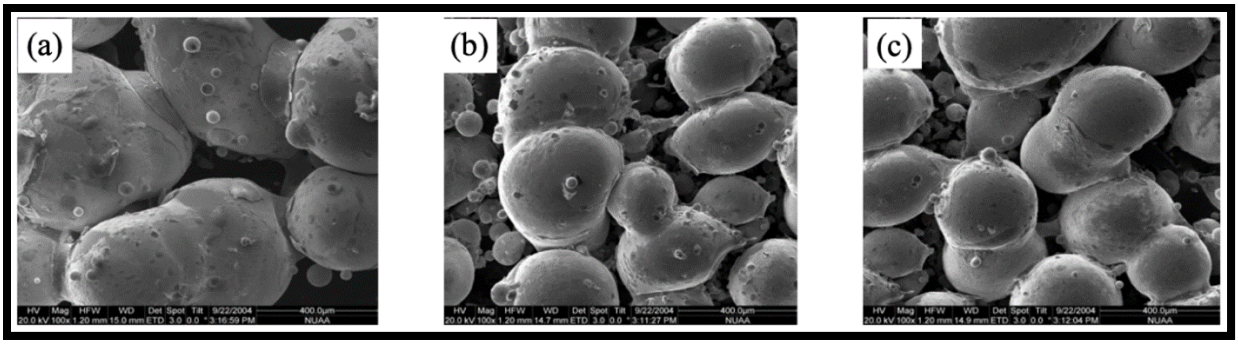

Figure 1.2: SEM images of balls formed at a fixed laser power of 300W but different scan speeds of (a) 0.05m/s, (b) 0.08m/s, and (c) 0.1m/s [10]

Laser Powder Bed Fusion processes have found their extensive applications in the aerospace, medical, automotive and many other high-tech industries. Increasing awareness about the benefits of metal manufacturing through the L-PBF process in the global manufacturing sector has clearly been visible through the increasing sales of these systems with every passing year. Research in and for L-PBF has also been actively carried out since the early 2000s after universities and industrial enterprises started getting accessible resources towards such systems. The advent of high-power fiber lasers have also had a valiant contribution in the significant and important transition from “partial melting” to “complete melting” of metals with more energy density input being made available to make the L-PBF systems more robust and optimized. Also, because of this, the ability to achieve finished parts with “insignificant” post-processing thus resulting into a wider range of applicable metal powder materials have become possible. With the expiry of key patents in L-PBF around 2013-15, more development and research carried out by different companies and research institutes have offered better and advances solutions to address

underlying concerns and limitations of the process. However, the L-PBF is a complex process and needs a comprehensive knowledge about the design and parameters of the system as well as the basic physical principles of the L-PBF process itself. Due to this, appropriate handling of the powder, choice of process parameters and scanning strategies collectively define the overall output efficiency of the L-PBF process [4].

1.1 Flow of Study

Chapter 1 gives a basic introduction and a brief history of metal Additive Manufacturing processes, especially the Laser-Powder Bed Fusion process and the advancements the process has seen over the years. It also talks briefly about the fundamentals of the L-PBF process and some of the challenges that are currently being addressed for the process.

Chapter 2 defines the various systems that are involved and play a major role in the smooth functioning of a typical L-PBF system and gives a brief understanding of the workflow and schematic of the process.

Chapter 3 addresses the significance of the thermal distribution in a powder bed fusion process. It also highlights different consolidation mechanisms that are practiced for manufacturing metal builds through SLS and SLM. The effects of an uncontrolled or uneven thermal distribution on the resulting output of the part in terms of its final mechanical and physical properties, defects in the built parts, etc. are discussed. Owing to this, the significance of the control of this thermal distribution, its direct effect on the microstructural evolution and grain growth,

leading to enhancements in the material and part properties is discussed. In addition, various techniques to address this thermal distribution have also been discussed.

Chapter 4 discusses the growing importance and application of stainless steels in Additive Manufacturing. It briefly highlights the different classes of stainless steels based on their chemical compositions. The advantages of these chemical compositions and their use in metal AM is also discussed. In the end, the choice of material for the proposed study is summarized given the characteristics of the material system and the direct challenges it possesses for its use in the proposed study.

Chapter 5 realizes the concept of the proposed study after taking into consideration the various limitations surrounding the process. It proposes a concept divided in four different stages and begins an initial discussion of the use of induction by highlighting the basics of the phenomena of induction. It then proposes a coil design through simulation study backed by comprehensive theory for induction heating. It steadily introduces the various factors defining the very purpose of this study and tests different stainless-steel materials as potential choice of material for the current and future study.

Chapter 6 marks the beginning of the Induction assisted Selective Laser Melting (ISLM) system development and testing. The chapter walks through the various aspects of the proposed study right from fabrication to assembly, testing and validation. It also talks about the various sub-systems that are integrated for the smooth functioning of the ISLM system to generate a proof-of-concept. It takes into

consideration various design factors that form the basis of the working of the system and makes the system ready for depositions and experiments in the following chapter.

Chapter 7 starts by documenting various protocols for the smooth functioning of the assembled system for its safe and effective use for depositions and experiments. The chapter gives a brief overview of the various programming controls and sub-system functioning setup required to run the experiments on the ISLM system. The system finally is used to deposit samples and run experiments based on a design of experiments drafted for the study. Once the deposits are made, the chapter walks through the various characterization techniques put to use to study the resulting properties of the build and the characteristic features of the proposed ISLM system. The data obtained through the experiments and analysis forms as a basis for building the Digital Twin.

Chapter 8 proposes the use of Machine Learning algorithms for porosity prediction observed in the deposits made through ISLM and its SLM counterparts. Four different approaches to address the use of ML are discussed with their corresponding results. A future framework is laid for developing a more robust Digital Twin by extensively branching out into the various potentials of Machine Learning.

Chapter 9 summarizes the entire ISLM study and highlights the scope and the merit of the work done as a part of this research. It also discusses various opportunities, applications and improvement windows for the betterment of the ISLM system as a whole and realizes the potential publications arising through the findings of the research work.

Chapter 2 Basics of the Laser Powder Bed Fusion

The high flexibility associated with the L-PBF process allowing the creation of complex geometries with unique structures allow for combining many components into a single functional build with tailored gradient structures and spatially varying material compositions. These advantages of the process help in finding and promoting a high-rise growth in the technology and a widespread application in various sectors of different industrial fields [11].

While the process finds itself different names like Selective Laser Melting (SLM), Direct Metal Laser Sintering (DMLS), Direct Metal Laser Melting (DMLM) and Laser Metal Fusion (LMF), L-PBF works on a simple concept of adding powder layer by layer according to the 3D design. Integrating various disciplines of science such as condensed matter physics, thermodynamics, material science, quantum physics, fluid mechanics, computational physics, electrical engineering, programming, design, industrial engineering and mechanical engineering, the L-PBF process can also be defined as a superposition and interaction of various subprocesses like the absorption and reflection of laser radiation by a dispersed medium, heat and mass transfer, phase transformations, a moving interface between different phases, gas and fluid dynamics, chemical reactions, solidification and evaporation, shrinkage, deformation, etc. Figure 2.1 shows an overview of the workflow of a L-PBF process right from the CAD design to the finished build.

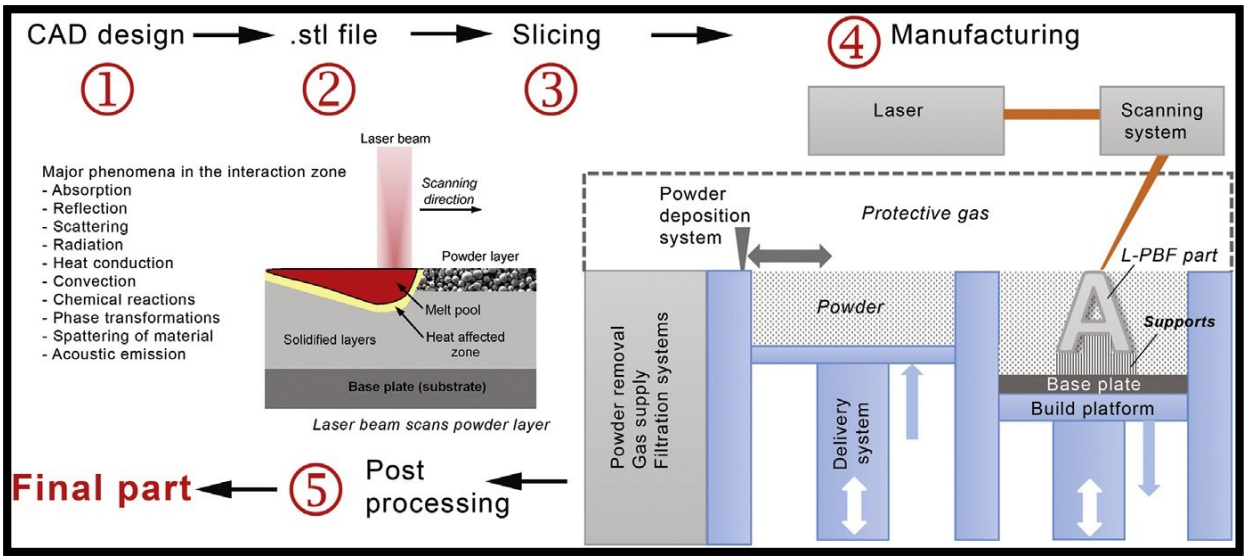

Figure 2.1: Workflow and schematic of a L-PBF process [11]

Pre-determined parameters of the L-PBF process are the properties of the material in use such as the density, melting point, thermal conductivity, particle size distribution, and laser beam properties. The variable process parameters are laser power, beam spot diameter, scan speed, powder layer thickness, inert gas atmosphere and the gas flow rate, etc. On the other hand, parameters having a significant impact on the quality of the L-PBF build can be further categorized into four groups namely “Machine-based”, “Material-based”, “Process Parameters” and “Post-treatment Parameters”. Their inter-dependency is not always clear, non-linear but still important. This is mainly due to the reason that there is no direct change in the output of the process by the change of one parameter. However, changing one parameter leads to a change in several other parameters and on the collective output of all the parameters affecting the quality and consistency of the build leading to undesirable and unpredicted results [11].

The process starts by a single-track formation by the interaction of the laser beam with a pre-spread and a defined layer thickness of powder on a base plate undergoing melting and solidification.

This single track becomes the fundamental unit of the part to be built. Numerous such single tracks together form a layer then following the layer-by-layer process to completely build a part [11].

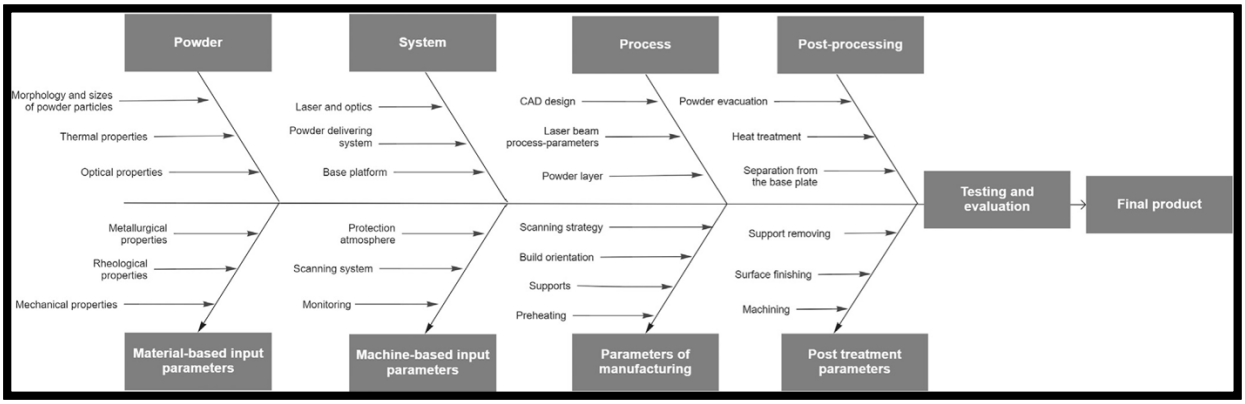

Figure 2.2: Main parameters influencing quality of SLM components [11]

2.1 Laser System

Most of the modern L-PBF systems make use of a continuous wave (CW) Yb-fiber laser with a 1070 ± 10nm as the thermal energy source to melt the defined powder region on the powder bed. In a typical fiber laser, a doped silica fiber is excited by a diode source. Two Bragg Gratings namely the High Reflective (HR) and Low Reflective (LR) work as mirrors to the linear laser cavity to generate the laser emissions. The active medium receives the diode pump energy through multimode fibers spliced to the multiclad coil. As a result of this, the laser cavity are directly created in the active fiber. A single mode passive fiber usually with a core diameter of a few micrometers allows the single spatial mode propagation of the laser emission, the profile of which is approximately Gaussian. The laser beam is then transformed into a high-quality collimated beam by using an appropriate collimator [11].

The laser radiation on metals is absorbed in a very thin layer at the surface by the free electrons also known as “electron gas”. This radiation only penetrates a few atomic diameters (1-2 atomic

diameters) making the metals opaque and shiny. Usually, the reflectivity of metals is very high for a wide wavelength range. This reflectivity goes on decreasing with an increase in absorption as the wavelength becomes shorter [11].

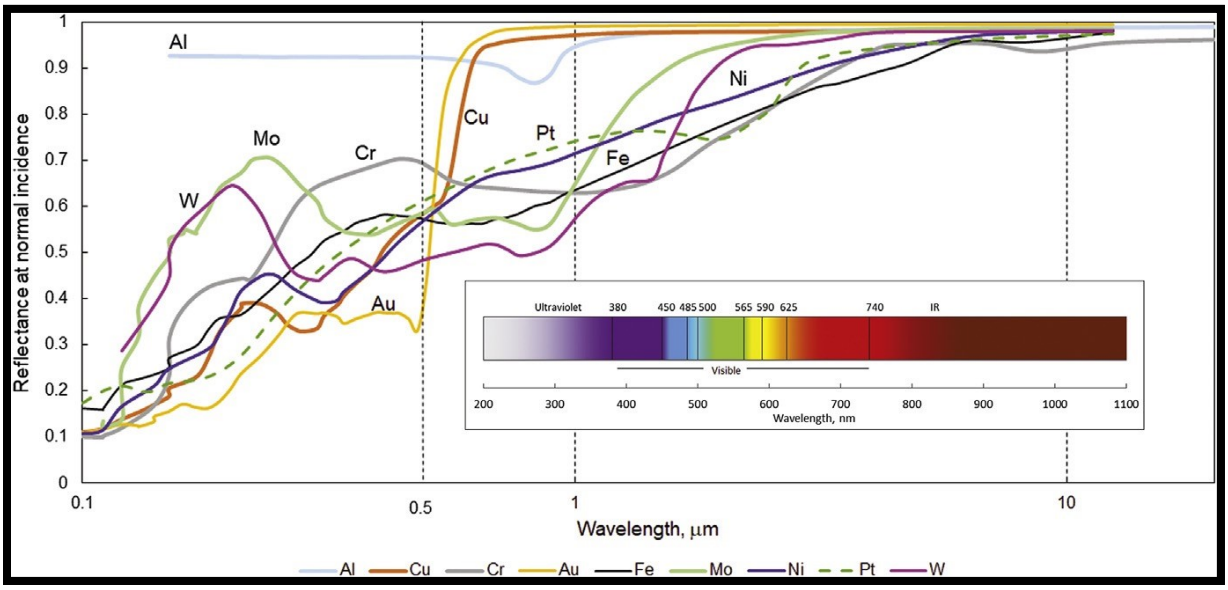

Figure 2.3: Normal-incidence reflectivity of selected metals as function of wavelength. [11]

2.2 Scanning System

After the collimated beam passes through the collimator and the beam expander, it then enters the scanning system. One of the two scanning systems with “active” or “passive” optics are put to use as the laser beam deflects out of the orthogonal scanners by the two mirrors. In case of a passive optics, the spherical lens only helps in focusing in a spherical plane leading to large distortions at the edges of the processing fields caused due to the defocusing of the laser beam in this region. To avoid this, the position of the focused spot must depend linearly on the product of the focal length (F) and the tangent of the deflection angle (θ). F-theta lenses do not change the size of the small laser spots over the scanning plane within the entire working field. However, F-theta lenses for

larger working fields need to be big and so become costly and unpractical as maintaining small focused spot size needs conformity with numerical aperture which, in turn, requires larger laser beam diameters and scan mirrors. Owing to this, active 3-axis scanning systems with "active" optics have started finding acceptance in the L-PBF process [11].

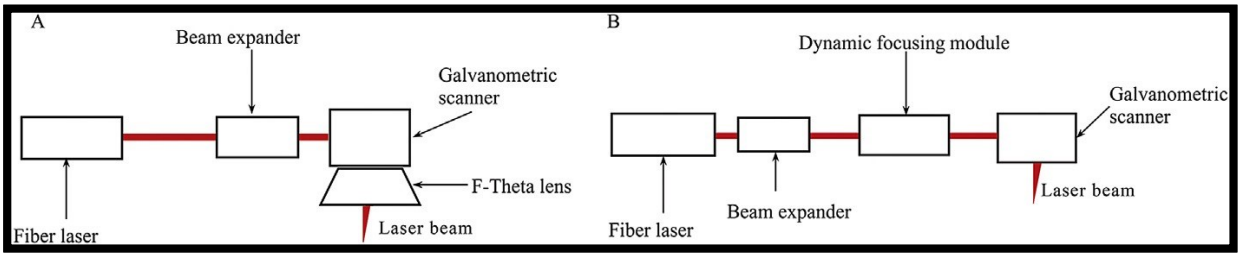

Figure 2.4: Scanning systems with "passive" (A) and "active" (B) optics [11]

2.3 Powder Deposition System

The powder delivery system applies a homogenous and equally thick layer of powder on the baseplate mounted to the build platform of the powder bed. The recoating systems can be classified into various types depending on the recoater in use: soft blade recoaters with rubber or carbon fiber brush, hard blade recoater from hard tool steel and rollers from hard tool steel.

Soft recoaters help spread a very thin layer of powder over the substrate on the build platform. Owing to their flexible nature, in case of a collision with the part during the build process, these blades do not damage the build and maintain the continuity of the process. They are useful for manufacturing delicate and cellular structures. Hard blade recoaters made from tool steel or ceramic do not allow for any of the slightest deformation of the metal part that is being built. In case of a collision of this type of a recoater, the process needs to be stopped thereby eliminating the defective component [11].

2.4 Baseplate and Build Platform

The substrate or the baseplate onto which the L-PBF part is fabricated is directly attached or mounted to the build platform. The substrate material should ideally match the powder material to allow for the weldability of the first layer of powder onto the baseplate. Platforms with pre-heating systems are used to avoid or reduce the residual tensile stresses that may be induced inside the part that is being built [11].

2.5 Powder Removal and Gas Supply

L-PBF parts need to be cooled down to take into account the pre-heating and the higher temperatures associated with them. The next step is to clean the baseplate of any unused powder and to remove or detach the baseplate from the built platform for any post-process treatments that may be required. The unused powder can be removed from the build platform in many ways: manually by the operator of the L-PBF system, a semi-automatic system making use of a vacuum technology and collecting the powder for further processing and a completely automatic system where the excess and unused powder is collected and sieved to eliminate any debris and ready the powder for reuse or recycle.

Given the large surface area of the powder particles, in order to avoid oxidation of the part being built under constantly high temperatures, the chamber is always maintained in an inert gas atmosphere [11].

Intensive evaporation and ejection of the powder material occurs due to the laser-material interaction. A constant flow of a uniform shielding inert gas over the powder layer helps remove the by-products of this process. On one hand, an insufficient shielding gas flow can cause defects

in the L-PBF built parts while on the other hand, an excess flow of the shielding gas easily blows of the powder from the bed eventually causing defects in the built parts. As a result of this, a uniform and stable shielding gas flow is an important process parameter of the L-PBF process [11].

In conclusion, the parameters that affect the quality, consistency, and performance of the L-PBF parts include machine parameters that define the system, such as laser type and wavelength, build volume and operational temperature, etc. In addition, they also include variable or controlled parameters such as laser power, scan speed, powder layer thickness, ambient inert atmosphere, protective gas flow rate, material, etc. [11]. A combination of these parameters and factors make the L-PBF process capable of manufacturing unique and complex geometries with utmost flexibility.

Chapter 3 Thermal Distribution in the Powder Bed

3.1 Consolidation Mechanisms

3.1.1 Selective Laser Sintering

Liquid Phase Sintering and partial melting are the consolidation mechanisms that are followed in SLS, as mentioned briefly in the previous chapter. This binding mechanism includes partially melting the powder material while the other part remains solid. The capillary forces arising due to the partial liquefaction of the powder material force the powder to spread itself instantaneously in the still solid powder particles. Due to this, higher scan velocities become possible. The material that melts maybe different than the one that remains solid. The former “lower melting point” material is then called the binder and the “higher melting point” material is called the structural material. Different ways to bind these two materials exist. They are as follows:

- Mixture of two-component powder (separate binder and structural powder particles).
- Using a composite powder that has a micro-composite structure containing the structural and binder material.

- Using coated particles in which the binding material is applied as a coating on the structural material. The binder material absorbs all the incident laser radiation. This induces the intended melting of the binder.

In all of the above methods, the binding material may be permanent with the part or may be removed later through de-binding cycles. In either of the situations, a post-sintering process (thermal heat treatment or HIP) for densification of parts maybe necessary. Partial melting of powder materials is also achievable in cases where there is only a single-phase powder i.e., no distinct binder or structural material. In such cases, the SLS experimental parameters are optimized in a way to partially melt the powder. The heat source (laser) in such a situation only provides heat to sufficiently melt the shell of the particle while the core of the particle remains solid. As a result of this, neck formation between different grains of the particles take place which binds the powder particles together.

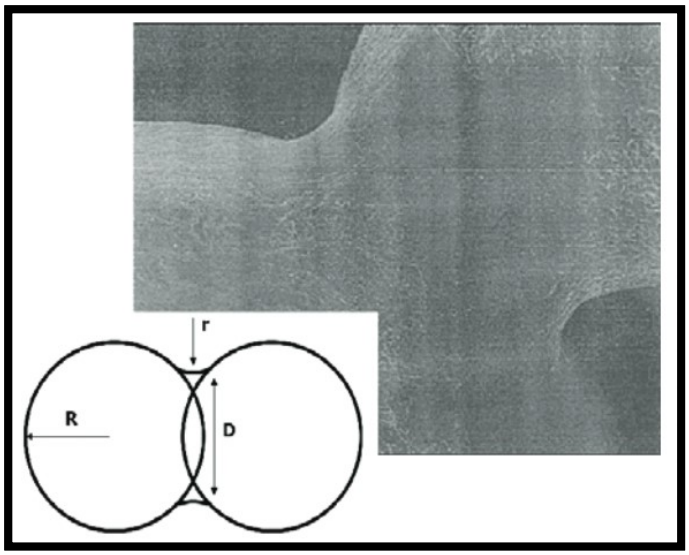

Figure 3.1: Typical neck formation between two grains of stainless steel [8]

Partial melting can also be achieved with powders having a bi-modal distribution i.e., small particles are melted while the bigger particles remain solid. Partial melting proves more beneficial as compared to Complete or Full Melting mechanism. It is because drastically higher laser scan speeds and scan spacing become possible during partial melting of the powder particles even when aiming for full dense parts. The economic advantage thus possible is considerable against the need for post-densification of sintered parts.

One of the challenges faced during the consolidation is controlling the flow of the heat-source. The molten pool formed due to partial melting needs to wet the previously deposited layer as well for it to solidify and form a uniform layer. Also, during this, it must also form a flat upper surface for the next layer of powder to be spread and sintered. Since partial melting of the powder takes place at higher scan speeds, the only conditions acting upon the powder to be sintered are the thermal distribution, capillary and gravitational forces. This leads to porosity in the parts. Therefore, to achieve sufficient wetting of the previously deposited layer, excess energy needs to be supplied. This excess energy and the peak temperature has its effects on the topmost surface of the sintered part. Thermal gradients are formed in the melt pool. Due to this, there is a potential to form convective motions to reduce these gradients. Temperature gradients at the surface along with temperature dependent surface tensions can cause rapid motions known as the thermos-capillary flow or the Marangoni flow. It is defined as the ratio of the speed by which the surface temperature gradient (dT/dx) changes due to convection or conduction (w is the linear size of the pool and K is the thermal diffusivity) [12].

3.1.2 Selective Laser Melting

The melting and binding mechanism involved in the complete melting of metal powders is majorly dependent on the following factors:

- Surface Tension
- Viscosity
- Wetting
- Thermocapillary effects
- Evaporation
- Oxidation [12]

In case of Selective Laser Melting (SLM), there is a leading edge to the melting pool. This leading edge under the influence of the surface tension advances into the powder in the area around the Heat Affected Zone (HAZ). This advancement gives rise to a possibility of the powder around the HAZ, which is already at a temperature just below the solidus temperature, to be wetted by the melt pool's leading edge. The wetting or not of this solid powder and if it is wetted, its dragging into the molten pool adds further complications in the consolidation process. As a result of this, a compromise is always needed to balance either the good wetting or re-melting of the previously deposited layer along with the topmost layer solidifying sufficiently flat and the powder bed not being disturbed too much ahead or around the dynamic HAZ. This adds a large constraint on metals and powder preparations for parts being fabricated through SLM.

In conclusion to the discussion of the consolidation phenomena and the effects of the process parameters on the same, a higher laser absorption in the powder bed reduces the variation in absorption throughout the powder bed. Smaller layer thickness with finer sized powder particles

eases out the need to over-heat the layers if re-melting of the previous layers is necessary. This becomes possible due to its large surface-to-volume ratio. However, all the above leads to the inability of consolidation at faster processing speeds [8].

3.2 Thermal Fluctuations and Its Effects

The basic mechanism of consolidation in any Additive Manufacturing process lies in the rapid heating and rapid solidification of the material being deposited, melted or sintered. The heat source providing the necessary temperature rise is Laser for SLS and SLM. During this process of rapid heating and solidification, the material to be sintered/melted undergoes many thermal excursions. As a result of this, residual stresses are induced in the part that is being built. The steep temperature gradient across the powder bed leads to different thermal expansions throughout the depth of the heating. The laser beam that is incident on the powder and the previously deposited layer coincides with the upper surface of the layer without initially melting the powder and the previous layer. This causes thermal stresses to be induced which causes bending of the upper layer of the part due to continuous heating. Initially, the layer under direct interaction of the laser bends in a direction away from the laser. This is known as counter bending. However, with continuous heating, the bending moment opposes the laser heat and starts bending towards the laser source and the mechanical properties of the material are reduced. During cooling, once the laser source is removed, the yield stress and Young's Modulus return but to much higher levels inducing plastic re-straining. This phenomena through which thermal stresses are induced is known as the Thermal Gradient Mechanism [13] [14].

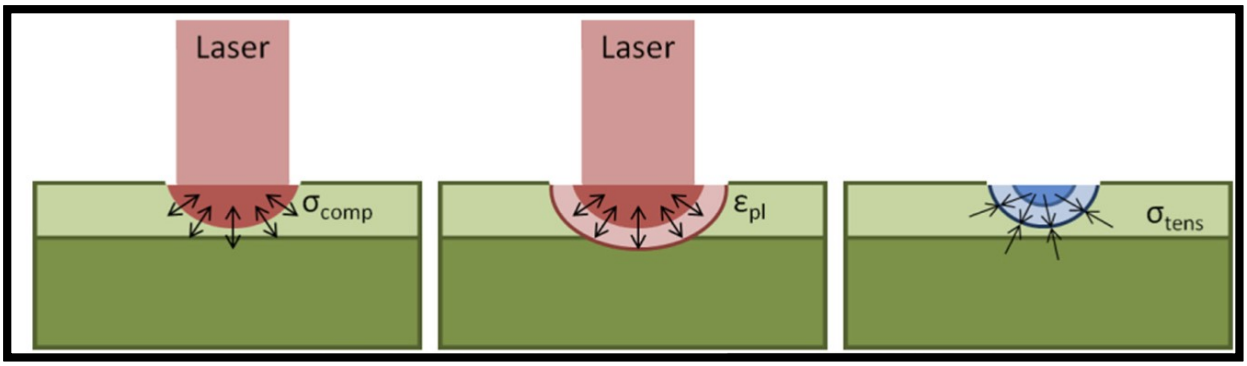

Figure 3.2: Stages of Thermal Gradient mechanism where σcomp, σtens and Ɛpl are the compressive stresses, tensile stresses and plastic strain respectively [14]

3.3 Residual Stresses and Its Effects

Residual stresses in any object or component are primarily induced due to non-uniform plastic deformations throughout the cross section of the component. This happens mainly during phase transformations, mechanical processing and due to the presence of thermal gradients. In practice, every component and object induces some kind of residual stresses throughout its processing i.e., these residual stresses have chemical, mechanical and thermal origins.

Residual stresses can then be categorized as per their length scales. They are represented in Fig 3.3, as Type I, II and III. Type I are macro-stresses induced during material processing due to plastic deformations and they usually equilibrate over the size of the component or the structure. Type II are micro-intergranular stresses ranging over a length approximately 3 to 10 times of the grain size. Differences in the microstructure of polycrystalline materials during phase transformations in a multiphase or a single-phase material mainly due to the anisotropy of the grains lead to residual stresses that fall under the Type II category [4].

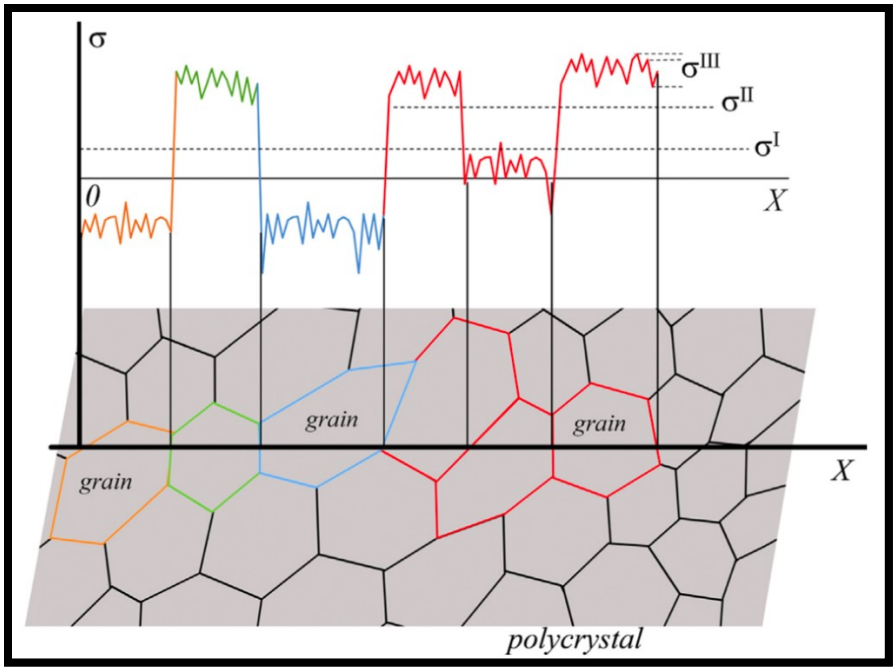

Figure 3.3: Residual stresses in a polycrystalline material categorized as per their length scales [4]

Whereas Type III stresses are intra-granular and are typically due to the coherency at the interfaces and dislocation stress fields. Manufacturing processes such as machining, metal injection molding and even Additive Manufacturing induce residual stresses in the components that they fabricate. In a powder bed fusion process, these can be induced due to part shrinkage, deformations during processing, phase transformations and due to temperature variations [4].

3.3.1 Residual Stresses in L-PBF

The fundamentals of a L-PBF process involving a high-speed, high-energy density laser causing rapid heating, melting, solidification and rapid cooling gives rise to thermal gradients. As this is repeated in a "layer by layer" nature throughout the entire process, high anisotropic stresses resulting in a specific microstructure evolution can be observed in parts printed through L-PBF.

In certain cases, these microstructures coupled with high residual stresses can result in delamination and/or cracking during the processing stage [4].

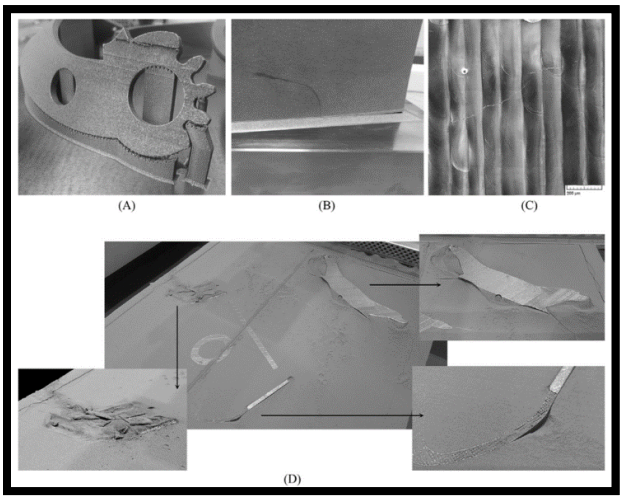

Figure 3.4: Defects in L-PBF parts during manufacturing: (A) delamination from the supports and deformation during processing Ti6Al4V alloy; (B) delamination from the base plate and macrocracking in massive Ti6Al4V solid sample; (C) cracks at the top surface of Ti-Al single layer; (D) general view of redistribution of powder bed during manufacturing: delamination from support and deformation resulting in contact with recoater: deformation of massive part (top image in D) and vibration of fine parts (bottom images) [4]

However, these defects are not limited to the processing stage only. They can develop even when the part is being removed from the build plate cracking the build. When residual stresses cause problems like cracking and delamination, these cannot be fixed in the post-production processes and the part built needs to be discontinued and process parameters need to be optimized. This affects the quality control, economic viability and the processes' reliability for adoption as a mass manufacturing technology. As a result, a stress induced distortion of only a couple of microns can be detrimental for the processes' industrial application. The fatigue and corrosion behaviors of the material and the part built also change depending on the magnitude of these residual stresses [4].

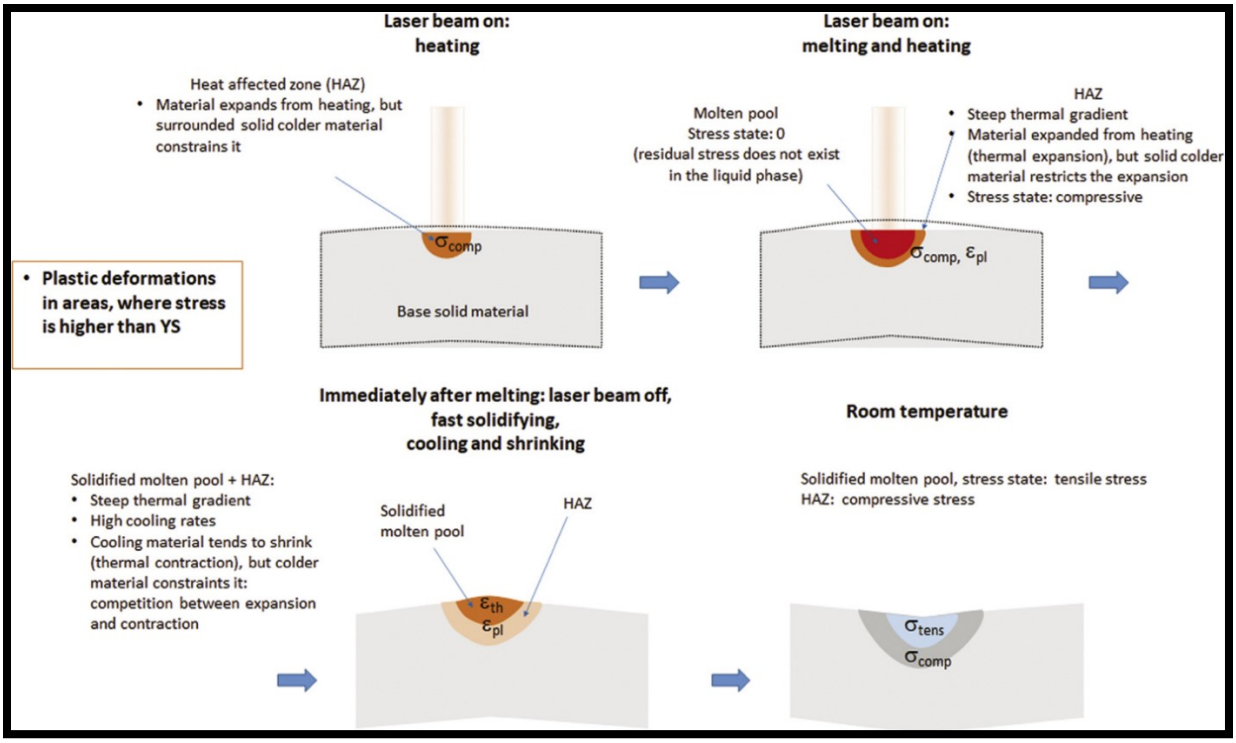

Figure 3.5: Residual stress during L-PBF process [4]

3.3.2 General Residual Stress Distribution

Following the very process of AM, the residual stress distribution in AM occurs repetitively layer by layer finally yielding a macroscopic level residual stress. The formation of the melt pool and the temperature surrounding it plays an important role in formation of these residual stresses along with other process parameters. Higher scan speeds help in lowering the maximum temperature by increasing the overall length of the melt pool while high laser powers cause the melt pool size to grow and increases the maximum temperature surrounding the melt pool. The experimental observations of the temperature distribution along a line from the center of the melt pool towards its tail end is as shown in the following figure. The plateau near the tail indicates the solidification zone [15].

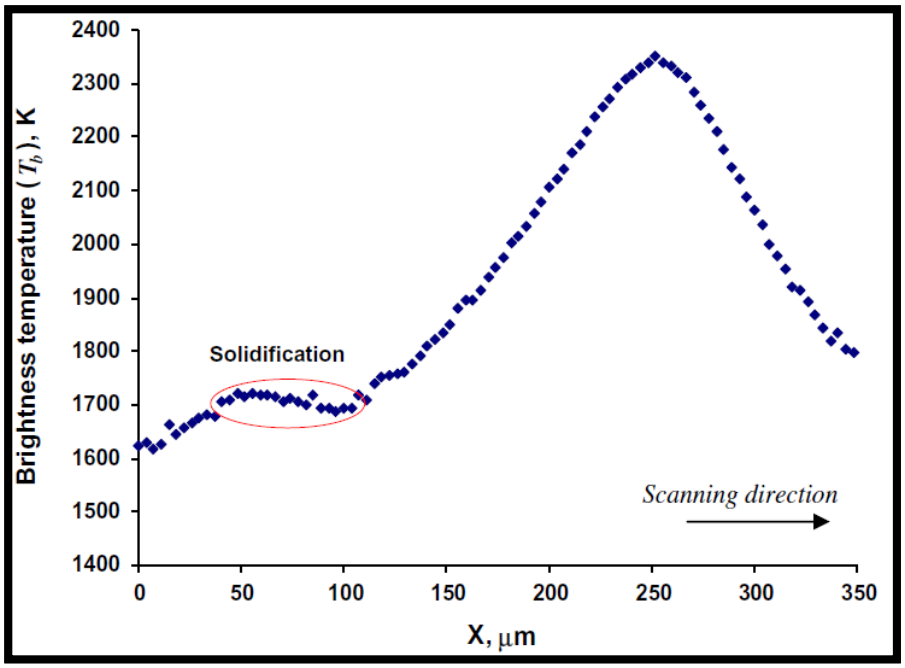

Figure 3.6: Experimentally measured temperature distribution along the central line spanning from behind the tail of the melt pool (X=0) towards just in front of the melt pool (X=350) [15]

Modelling efforts of the melt pool in the process show the interaction of the laser beam penetrating deep into the material and forming a keyhole weld type melt pool. The recoil pressure from the laser-material interaction and evaporation pushes the melt backwards and the surface tension lifts the melt pool above the level of the layer. It clearly indicates the interaction of individual powder particles with the laser and its effects after its drawn in the melt pool leading to instabilities [15].

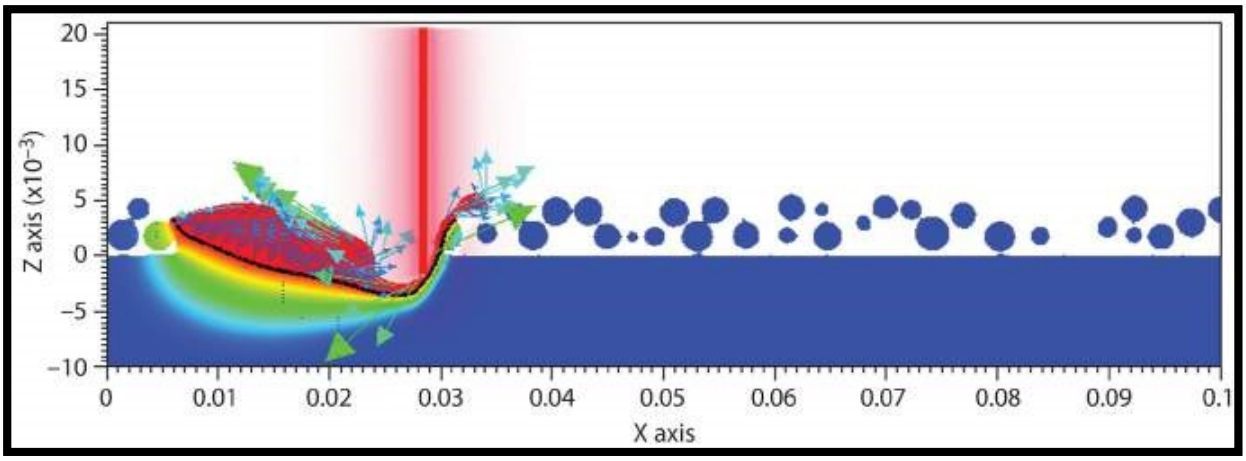

Figure 3.7: Realistic modeling of the melt pool shape, melt flow and formation of the scan track [15]

In conclusion, these residual stresses, deformations, temperature gradients and / or cooling rates can be reduced by:

- higher laser powers
- slower scan speeds
- thicker layers
- use of preheating methods in the powder bed [15].

3.4 Microstructure Evolution in Additive Manufacturing

The complex thermal cycle during a typical AM process involves rapid heating of the material due to the absorption of energy from the laser (or any other heat source involved) followed by a rapid solidification of the molten pool after the energy source moves further away. This process of rapid heating and cooling, as discussed earlier, keeps repeating itself causing the fusion of the succeeding layers to the previously molten layers keeping the volume element still exposed to heat. As a result of this, meta-stable microstructures are usually formed in the resulting deposits.

Therefore, the AM microstructure becomes a result of this complex thermal cycle owing to the temperature gradients present throughout the process. These temperature gradients are primarily dependent on the energy density and the scan speed followed by other process parameters such as the layer thickness, preheating temperature of the powder bed, if any, etc. In addition to this, the difference in the heat conduction of the powder material and the solidified molten track also affects the temperature gradients, in turn, affecting the resulting microstructure. As a result, the microstructure may vary within a deposit or part manufactured through AM.

3.4.1 Grain Growth and Property Enhancement in AM

With the growing research in AM, industries have now started favoring laser processing techniques that provide them the ability to manufacture materials and products with different mechanical properties by means of tailoring the microstructure at different levels to best suit the application requirements.

The laser interaction with the material under use for a typical AM process leads to the formation of a molten pool. This molten pool can be formed in two modes i.e., “Conduction” or “keyhole”. A shallow and wide shape of the molten pool formed due to local melting is a characteristic of the conduction mode whereas a narrow and deep molten pool formed due to the high energy intensity is a characteristic of the keyhole mode. However, given the high quality and control of the heat input with fewer defects makes the conduction mode of molten pool formation a more popular choice in laser processing. During the solidification stage, the molten pool border acts as nucleation sites for new grains to grow towards the laser incidence point. The intensive competitive grain growth at this stage nucleates into different grains with preferable growth directions different

for different grains, the most favored of it being the one with respect to the thermal gradient at the solid-liquid interface. This means that the grain growth rate is higher for those that are parallel to the thermal gradient vectors in the molten pool [16].

The elliptical shape of the melt pool extends from the point of laser incidence as the laser scans through with increasing speeds. Heat transfer in the melt pool through conduction takes place from the bottom of the melt pool. This pass of heat transfer then leads to the initiation of the solidification and crystallization stages. As a result, the solidification and crystallization stages can be controlled by controlling this heat transfer. This makes the heat transfer from the molten pool to the bottom of the cooled solid deposit the most key highlight of the selective laser melting process.

The basic principles of solidification and crystallization for a typical L-PBF process are very similar to a standard welding process. The only significant difference between the two being that in a L-PBF process, the maximum temperature of the liquid melt pool is much higher, and the size of the melt pool is much smaller as compared to the one observed in the welding process. In L-PBF, the solidification process needs to find the correct balance between the energy input and the dissipated energy into the previously solidified layer. The resulting microstructure is a combination of the thermal gradient, G and the growth rate, R [17].

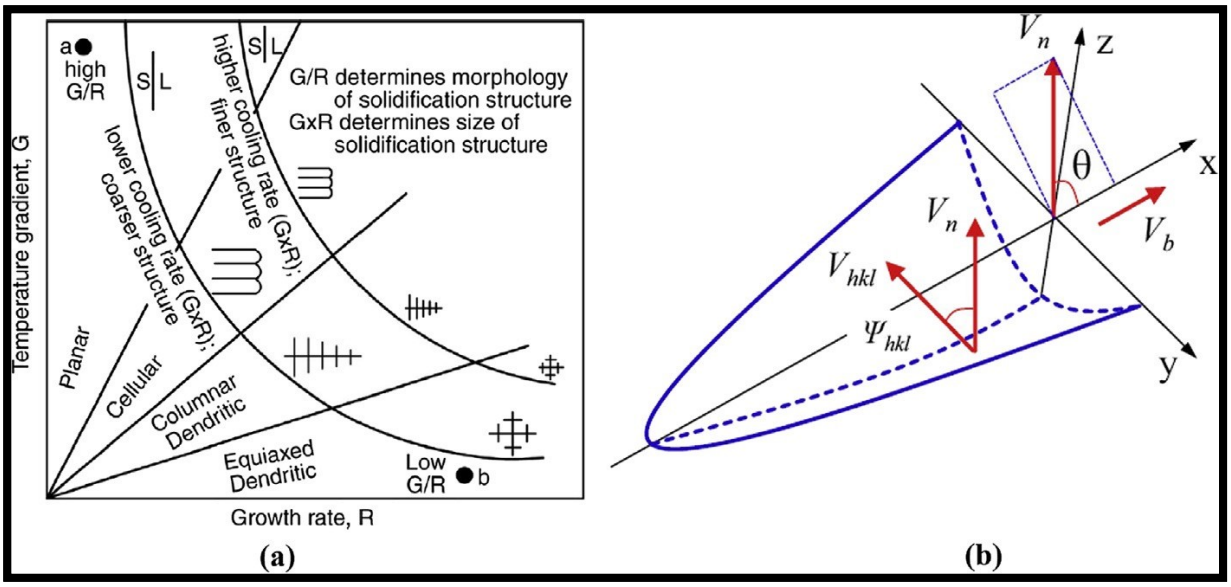

Figure 3.8:(a) Influence of temperature gradient G and growth rate R on the morphology of solidification microstructure, (b) Schematic representation of the melt pool illustrating angular relationships between the scanning velocity V_b, the solidification interface normal V_n, and the dendrite growing direction V_{hkl} [17]

Epitaxial nucleation and cellular or cellular / dendritic crystallization are experimentally observed in alloys manufactured through the L-PBF process. Austenitic stainless steels are the best examples to study the microstructures obtained through the L-PBF material solidified and cooled without any phase transformation happening in the solid state. AISI 316L stainless steel has been the most investigated austenitic stainless steel for microstructural research for the L-PBF process. Typical microstructure formed in 316L stainless steel can be seen in Figure 3.9 where higher cooling rates during laser melting of the powder and the resulting higher thermal gradients form cellular colonies [17].

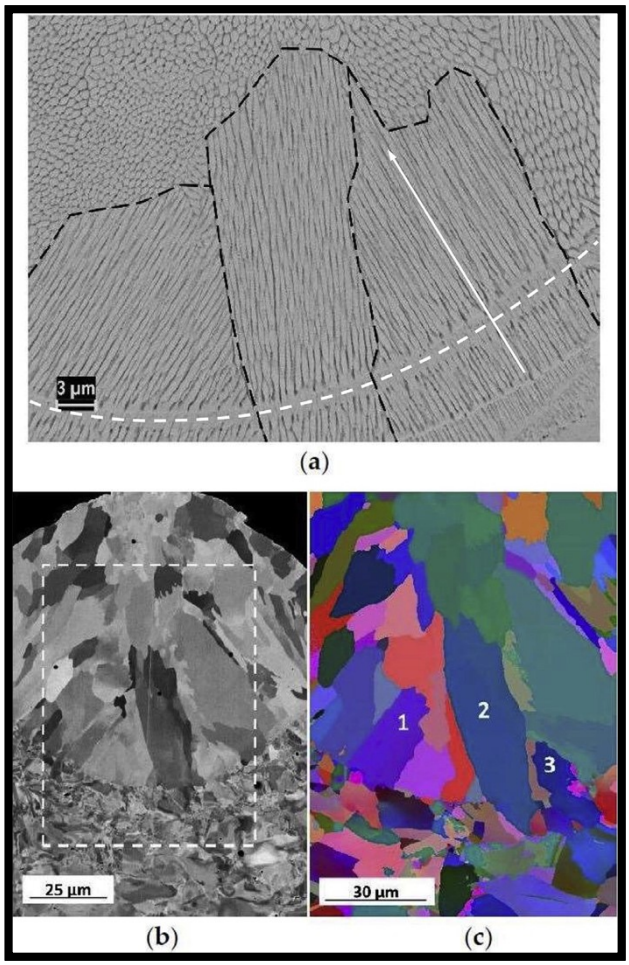

Figure 3.9: (a) Microstructure of L-PBF 316L stainless steel. Fusion boundary is marked as a dashed line, a white arrow indicates cells and colony growth direction; (b) cross-section of the L-PBF 316L single track; (c) an electron back-scattering diffraction (EBSD) orientation map of the marked region in (b). Colonies 1, 2, and 3 epitaxially nucleated from the substrate. [17]

The cells within the same colony have the same crystallographic orientation due to this epitaxial nucleation. The cellular structures formed during the solidification of 316L in a L-PBF process are usually associated with the micro-segregation of Cr and Mo at the cell walls. Studies also suggest that the dislocation structures originating in AM are a result of thermal distortions during printing, which are primarily an outcome of the melt pool dynamics and thermal cycling [17].

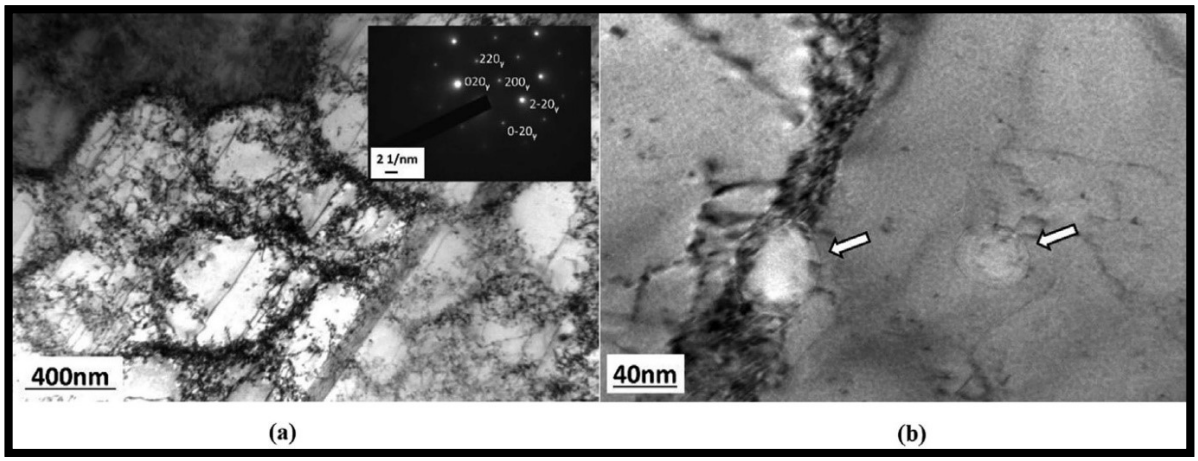

Figure 3.10: Microstructure of as-built L-PBF sample 316L austenitic steel, TEM images: (a) the bright-field image of the cellular structure with high dislocation density structure; (b) round oxide particles indicated by arrows [17].

At times these temperatures during the thermal cycles are high enough to intensify diffusional processes in the already solidified previous layers. These result in thermally activated solid-state phase transformations, phase composition changes, and other microstructural changes that occur in-situ during the printing process. In other words, the powder material undergoes an in-situ heat treatment during the manufacturing process itself [17].

A similar study on the Ti6Al4V alloy used for an AM process also shows that the columnar grain growth is a result of directional cooling and the thermal history of the material. An increase in the laser power decreases the length of these columnar grains which eventually are replaced by large equiaxed grains. This is also evident from the fact that there is a decrease in the temperature gradient from the first layer throughout the height of the built part. This occurs due to the higher laser power causing very high temperatures at the surface of the top layer and then remains to be hot during the sintering of the consequent layers. As can be seen from Fig.3.11, a columnar grain growth is obtained from the depositions as a part of the study. This grain growth is a result of

conduction of heat through the walls of the part built and the build temperature which is maintained constant throughout the process. The microstructure layer obtained between the band layers is the basket-weave widmanstatten structure. The widmanstatten structure is known to enhance material properties such as fracture toughness, creep notched fatigue resistance and fatigue crack growth resistance [18].

To tailor the mechanical properties, the grain size and orientation can be controlled by controlling the laser parameters however this leads to changes in some process properties such as the highest temperature inside the melt pool, dimension of the melt pool and even the mode (conduction or keyhole). This opens windows for defects and pores thus ruining the quality and the build of the deposit [16].

In conclusion, the complete thermal history of the L-PBF process is complex and is heavily dependent on its process parameters. Often due to this complexity of solidification and thermal history, L-PBF materials show anisotropic properties and therefore, as a result, require heat treatment after the manufacturing process. However, these heat treatment processes need to guarantee that the desired microstructures and properties need to be retained and / or developed as an outcome of these processes [17].

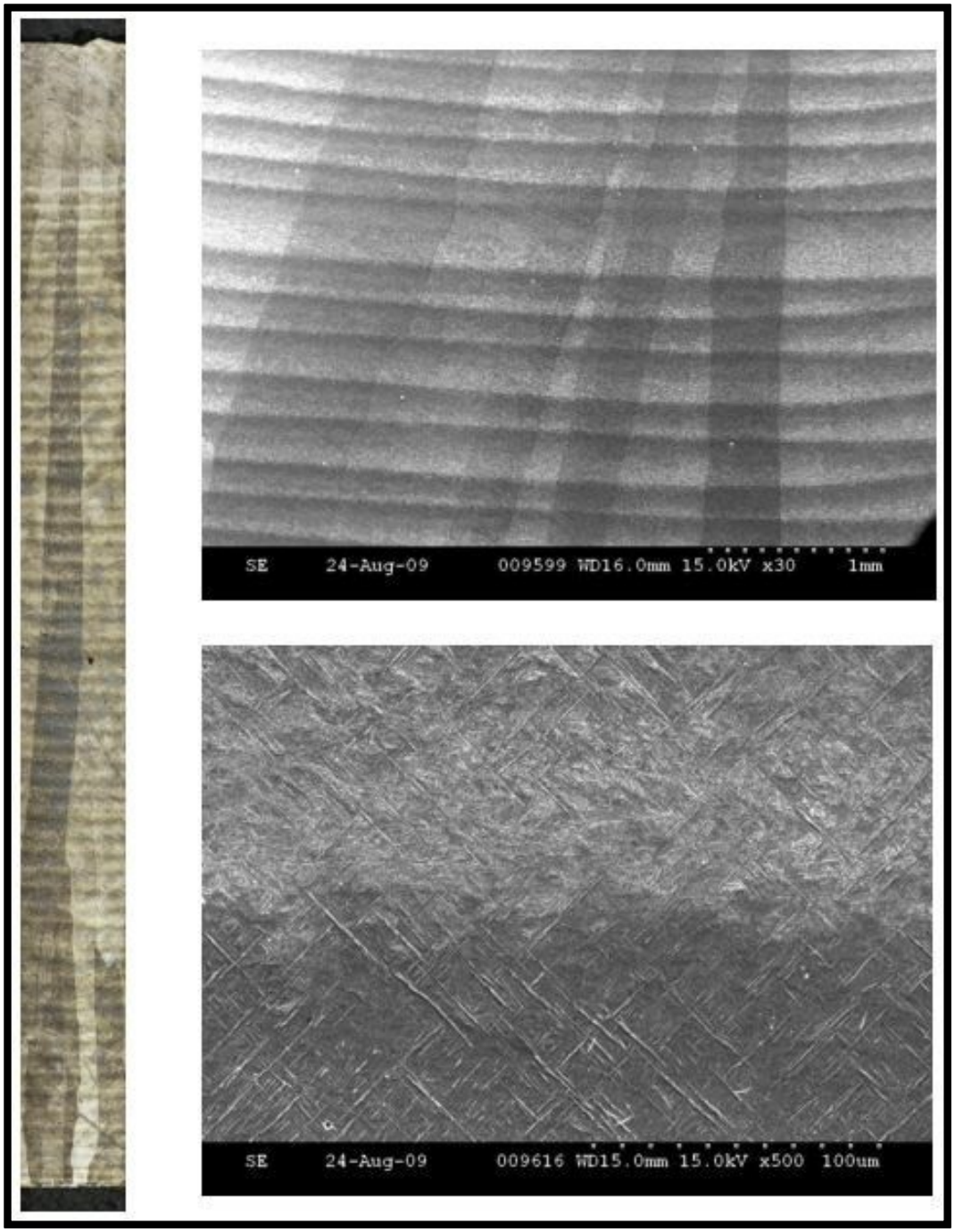

Figure 3.11: (a) Optical micrograph of the entire deposit showing the columnar grain growth for Ti6Al4V (left), (b) SEM image at 30X of columnar grains throughout entire deposited length and width.(top right) and (c) SEM image showing the widmanstatten st

3.5 Control of Thermal Distribution in L-PBF

3.5.1 Heat Treatment

Post-process stress relief heat treatment is a common practice for parts built through the L-PBF process. This is usually done before the parts are detached from the baseplate. This helps in avoiding any distortions that may be formed as an outcome of the heat treatment process. Upto 70-90 % of the residual stresses can be relieved from the L-PBF parts by implementation a suitable heat treatment process. However, such stress-relieving heat treatments are not always desirable as they, at times, can lead to undesirable phenomena such as carbide precipitation observed in Nickel alloys. Also, despite the use of these widespread heat treatment processes, they do not always help in relieving the tensile residual stresses completely. Due to this, an AM specific heat treatment process needs to be found and approved to avoid unwanted microstructural changes. Moreover, these changes are sometime process parameter dependent which make it even more challenging to apply a general heat treatment solution to L-PBF or AM built parts [4].

3.5.2 Mechanical Treatment

The process by which the surface of the built parts is impacted by high-speed shots of metallic, ceramic or glass beads, known as shot peening, is said to improve fatigue properties. The combination of an optimal heat treatment process with shot peening can allow the introduction of uniform compressive stresses in L-PBF parts. Laser Shock Peening (LSP), a surface modification technique, thus finds its application for AM parts. The technique proves useful by reducing the magnitudes of the tensile stresses by introducing compressive stresses to the surface of the parts. The effectiveness of LSP is directly dependent on its process parameters such as the laser energy,

shot overlap, laser spot size, laser pulse duration, etc. The added benefit of the LSP technique is the closure of the near-surface porosity. Its high operational cost, however, limits its widespread use [4].

3.5.3 Ultrasonic Impact Treatment (UIT)

The process of applying high-frequency ultrasonic oscillations to the built component to reduce the residual tensile stresses as well as to introduce compressive stresses is known as Ultrasonic Impact Treatment. It is also known as high frequency mechanical impact. Studies have also shown an improvement in the surface roughness, microhardness, and near-surface porosity through UIT for L-PBF parts.

Most of these post-process treatments on L-PBF parts for controlling, relieving and / or reducing the induced residual tensile stresses are quite capable yet ineffective of completely reversing the deformations caused due to these residual stresses. Furthermore, they increase both, manufacturing time and cost hindering the very objective of “rapid manufacturing” through the L-PBF process [4].

3.5.4 In-Situ Stress Relief

Various advances have been made for in-situ thermal gradient management. These consist of preheating the powder bed and / or the powder, changing scanning patterns to control the thermal gradient and the cooling rates.

3.5.4.1 Baseplate and Build Chamber Preheating

Thermal gradients inducing residual stresses are a result of huge temperature differences between the melt pool and the surrounding powder at the ambient temperature. Preheating the baseplate, powder bed and / or the build chamber helps in reducing this temperature difference and thus helps in avoiding or minimizing the residual stresses. Studies have shown a reduction in the residual stresses for as much as 40% by preheating the baseplate of the powder bed. However, preheating the baseplate and the powder bed also increases the chances of the powder oxidizing and reducing the reusability and deteriorating the mechanical properties of the part thus built. Also, controlling the preheating temperature to values below the powder sintering temperatures is equally important so that the overall efficiency of the process is not affected. Preheating has a significant impact not only on the stress levels of the material but also on the desired density, microstructure, and mechanical properties [4].

3.5.4.2 Process Parameter Optimization

Laser power input, powder layer thickness, hatch distance and scan speeds have a regulatory effect on the generation of residual stresses in parts manufactured through L-PBF. Studies have demonstrated a decrease in the residual stresses by increasing the laser power and slowing down the scan speeds. Higher laser powers and slower scan speeds increase the melt pool size and the maximum temperature around it while simultaneously lowering the temperature gradient or the cooling rate. Thus, optimizing the laser power and scan speeds can help reducing these stresses and maintain the desired part density.

However, a generalized parameter adjustment approach cannot be applied to L-PBF without taking into consideration factors like the part geometry and powder layer thickness. Depending on the geometry of the part to be built, customized scanning strategy per layer may need to be incorporated. Pre-determining the high-stress zones in the desired geometry of the build and increasing the layer thickness for these pre-determined zones can reduce the residual stresses by almost 8.5%, a study shows. Another approach towards achieving non-porous builds with thicker layer emphasize on higher energy input to sufficiently melt the thicker powder layers and remelt the previously solidified layers. On the other hand, while increasing layer thickness reduces the residual stresses, it increases the tendency of formation of inter-layer defects with increased porosity in the builds thus lowering the resulting mechanical properties of the finished parts.

In conclusion, a justified compromise needs to be achieved in reducing the residual stresses while optimizing the process parameters without significant effect on the resulting properties, completely dense overall builds without defects such as cracks and delamination [4].

Chapter 4. Stainless Steels and Their Use for L-PBF

The widespread applications of stainless steels in different sectors of the industry are a clear representation of its importance. Over the years, the development of numerous grades of stainless steels have increased rapidly. These grades of stainless steels with widely varying compositions have been sufficiently attractive to merit the trouble of standardization.

As the microstructure of the metal always has a prominent effect on the final properties, stainless steels can be categorized based on their microstructures at room temperatures. Since each of this grade is different based on their compositional, microstructural, and crystallographic factors. As a result of this, depending on their thermal history and the composition, stainless steels are found in different crystallographic and microstructural forms. i.e., BCC (α-δ) ferritic, FCC (γ) austenitic and BCC or BCT (α′) martensitic. Each one of them is briefly described below [19] [20].

4.1 Classification of Stainless Steels

4.1.1 Ferritic Stainless Steels

Ferritic stainless steels are grades of steel with ferrite as their predominant metallurgical phase. They are usually alloyed with Chromium ranging between 11–12.9 wt% with minimal to no addition of Nickel as it is one of the most priced alloying elements. The minimal addition of Ni thus helps in maintaining the economic stability of ferritic stainless steels as compared to

compositions of steels with higher Ni content. In terms of applications, ferritic steels fall behind of their austenitic counterparts. This is primarily due to poor ductility and poor weldability, susceptibility to embrittlement and poor formability [19]. There are also high temperature ferritic grades with improved resistance to high resistance. They are typically alloyed with higher Carbon content as compared to standard ferritic stainless steels to increase creep strength and with Silicon and Aluminum to improve oxidation resistance [20].

4.1.2 Austenitic Stainless Steels

Austenitic stainless steels are the largest groups of austenitic grades. They can be further categorized into five groups namely: Cr-Mn grades, Cr-Ni grades, Cr-Ni-Mo grades, high performance austenitic grades and high temperature austenitic grades. Excellent corrosion resistance, good weldability and formability are some of the principal properties of austenitic stainless steels. Their good impact strength at lower temperatures have found vast cryogenic applications.

4.1.2.1 Cr-Mn Grades

Also referred to as the “200 grades”, the Nickel content in these grades is on the lower end. Nickel is replaced with Manganese and nitrogen which helps in maintaining the austenitic microstructure [20].

4.1.2.2 Cr-Ni Grades

Sometimes referred as the 18-8 stainless steels, the Cr-Ni grades are the “general purpose” grades alloyed with Chromium and Nickel but no Molybdenum. At times, they are alloyed with Nitrogen to improve the strength or with Sulphur to make them good machinable alloys. Niobium or Titanium is also added at times to increase their high temperature mechanical properties [20]. The Cr-Ni-Mo are just enhanced alloys of the Cr-Ni grades with improved corrosion resistance with the addition of Mo ranging between 2-3wt.% Mo.

4.1.2.3 High Performance Austenitic Grades

Developed with an intent for use in high demanding environments, the Chromium content in these grades vary between 17 and 25%, Nickel between 14 and 25% while Molybdenum between 3 and 7%. These are usually alloyed with Nitrogen to improve the corrosion resistance while some are alloyed with copper to improve resistance against acidic environments [20].

4.1.2.4 High Temperature Austenitic Grades

Primarily designed to operate at temperatures above 550°C i.e., the point after which creep strength becomes a deciding factor, high temperature austenitic stainless steels are designed to provide long service life at high temperatures. They are often characterized by higher Chromium and Nickel content without any presence of Molybdenum [20].

4.2 Steels in Additive Manufacturing

Recently, large amounts of steels are processed through Additive Manufacturing. The different mix of microstructures and phases of stainless steels provides the flexibility of achieving tailored microstructures for steels through Additive Manufacturing as it is through conventional manufacturing techniques. However, the varying time-temperature profiles these steels are subjected to through a typical AM process make their microstructure differ significantly as well. This ranges from steels constituting very fine grains, highly morphological and crystallographically textured grain structures to non-equilibrium microstructures in their as manufactured states through AM [21].

All of the literature related to the investigation of austenitic stainless steels in Additive Manufacturing is almost exclusive to 316L stainless steel with a few reports for 304L stainless steel. Austenitic stainless steels, now routinely manufactured through AM, specifically Selective Laser Melting, were partially successful in the early 2000s due to the Balling phenomena commonly observed in processing of these steels. One of the contributing factors leading to balling was the use of coarser powder size (approximately 75 μm). Continuous efforts towards varying the powder size of these austenitic stainless steels coupled with optimizing the process parameters have resulted in overcoming the Balling phenomena and manufacturing dense solid parts through the L-PBF process [21].

The following figure presents an overview of the AM process dependency of different types of steels for the variation in their respective mechanical properties.

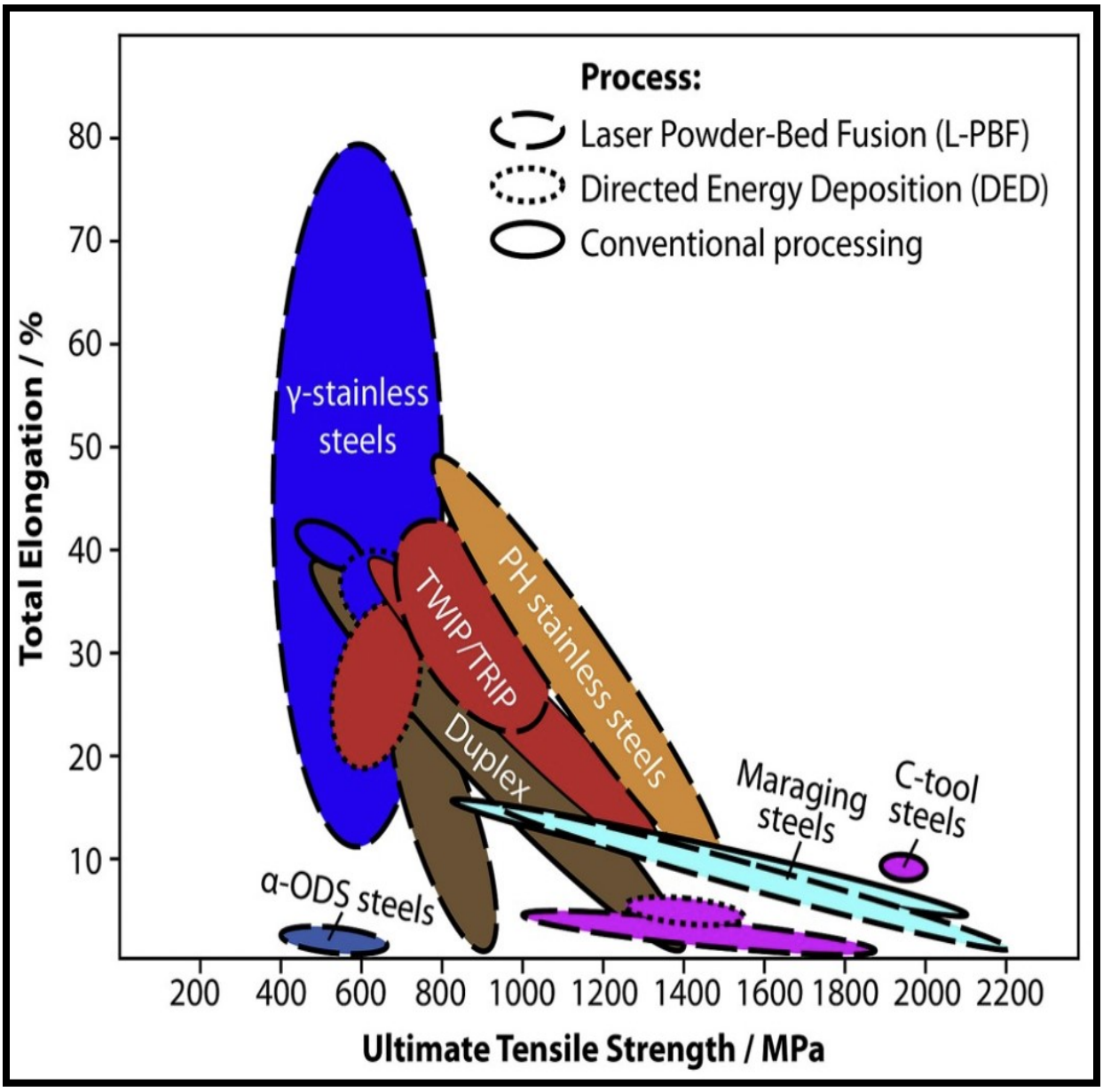

Figure 4.1: Mechanical property dependency of steels on different AM processes [21]

4.3 Microstructure of Austenitic Stainless Steels

Austenitic stainless steels in L-PBF are seen to grow columnar grain structures with fine solidification cells. Given their similar crystallographic orientations, hundreds of these cells come together to form one austenitic grain with high angle grain boundaries. Despite the simple microstructure, austenitic stainless steels processed through L-PBF portray excellent mechanical properties as compared to their conventional counterparts. The possibility of controlling the cooling rates or the thermal gradients during and after solidification by optimizing or varying process parameters opens a great potential to command local and digital control over the resulting microstructure which isn't possible through conventional manufacturing techniques [21].

Figure 4.2 gives an overview of different types of microstructures observed in the L-PBF and DED (Directed Energy Deposition) AM processes as compared to that from conventional processes.

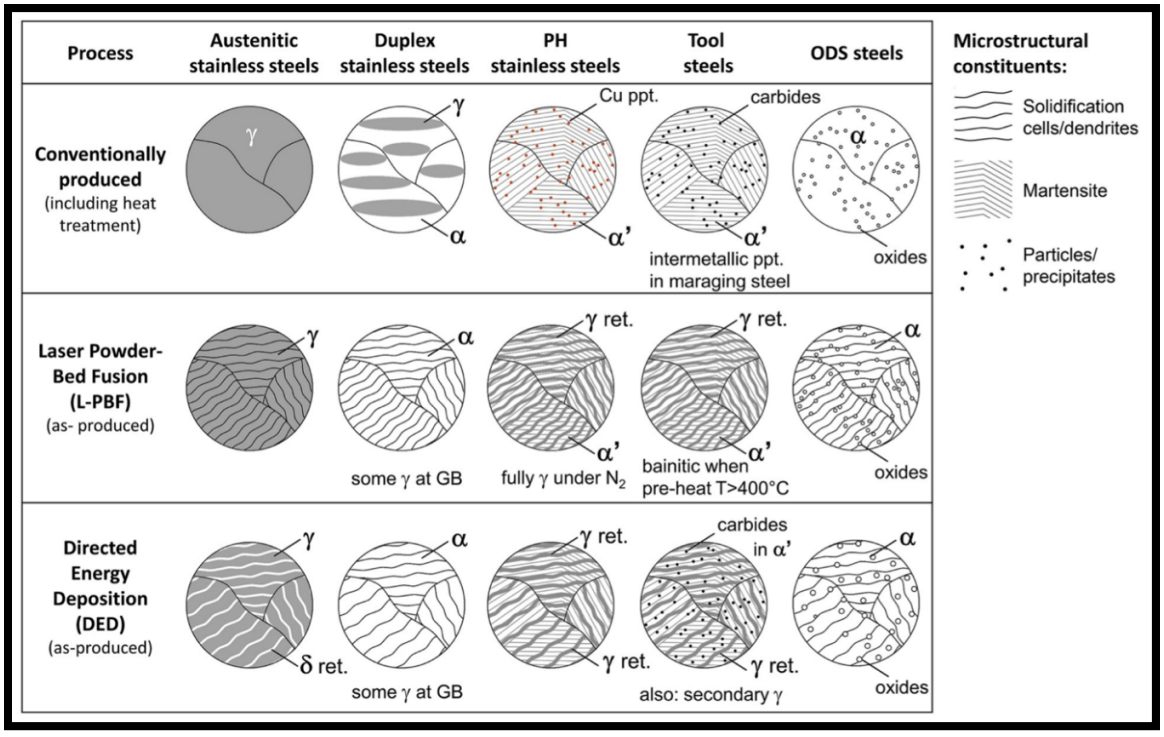

Figure 4.2: Microstructures observed for different grades of steel by conventional processes and their AM counterparts [21]

4.4 Material Selection for the ISLM

The wider applications of SS316 and the extensive research in the field of AM for the material system makes it favorable material of choice. Moreover, the study proposes the use of electromagnetic systems to address concerns discussed in the previous chapters. The austenitic phase of SS316 makes it a challenge to design an electromagnetic system around it given its non-magnetic properties. In addition to this, the easy availability of the raw material in all shapes and form (powder in the case of this study) favors well for its application in the proposal of the concept in the coming chapters. However, the initial phase of the study still takes into consideration other alloys of steel to explore any opportunities of application as a part of the future work of the study.

Chapter 5. Concept Generation and Coil Design

5.1 Concept Realization

Studies on the use of external fields in the solidification have been largely confined to conventional casting processes [22] [23] [24]. In contrast, an entirely additively manufactured component can be effectively influenced with the presence of an external field given that the entire volume of the melt pool is comparatively quite smaller as to that of a casting process (0.1 – 1.0mm in width), use of external fields for metal AM becomes a valuable research opportunity for microstructure control in AM without essentially changing the alloy composition of the material under consideration [25]. Efforts have been made to address the grain growth or refinement as a result of uncontrolled thermal distribution in metal AM, by means of adding secondary heating sources to the AM process. Studies show that the use of secondary laser heat sources as grain structure controllers decreases the thermal gradients inside the molten pool and also changes the shape and size of the molten pool. This helps in uniform grain growth inside the molten pool and the grain orientation is also strongly affected. A schematic of the top view of the use of a secondary laser heat source used along with laser melting is shown in Fig.5.1. The temperature profile thus obtained can be seen in Fig5.2a and the resulting change in orientation of the grain growth to being almost perpendicular to the laser scanning direction can be observed in Fig.5.2b [16].

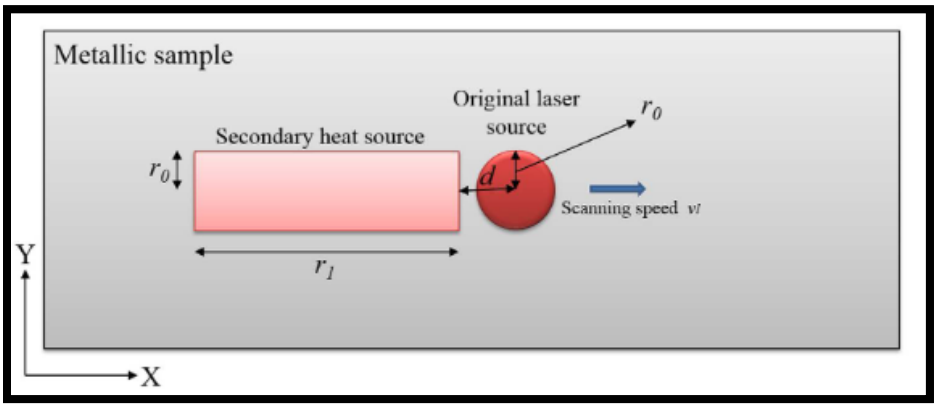

Figure 5.1: Schematic of a secondary laser heat source (top view) [16]

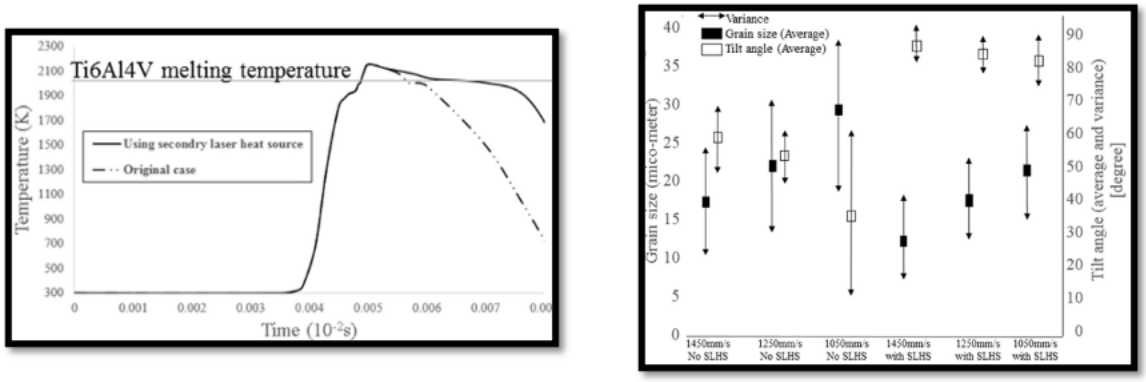

Figure 5.2: (a) Temperature profile (left) (b) Comparison between grain size and grain orientation for difference condition (right) [16]

Induction heaters to preheat powder bed prior to laser melting process, resistive preheating systems, post-process heat treatments, etc. are also some of the recent developments in terms of addressing tailored manufacturing. A recent study shows making use of micro-induction sintering to selectively sinter powder particles at radio frequency with an attempt to address minimal post processing, without making the use of a laser. When this system is triggered, it sends a RF-signal to the amplifier which amplifies the signal equivalent to a power wattage of more than 200W. The amplified signal is then transmitted to the powder and a fraction of it reflects back. This signal is

then analyzed to calculate the coupling efficiency of the emitter and the powder particles through the Voltage Standing Wave Ratio (VSWR) [26]. A schematic of the signal flow is shown in Fg.5.3

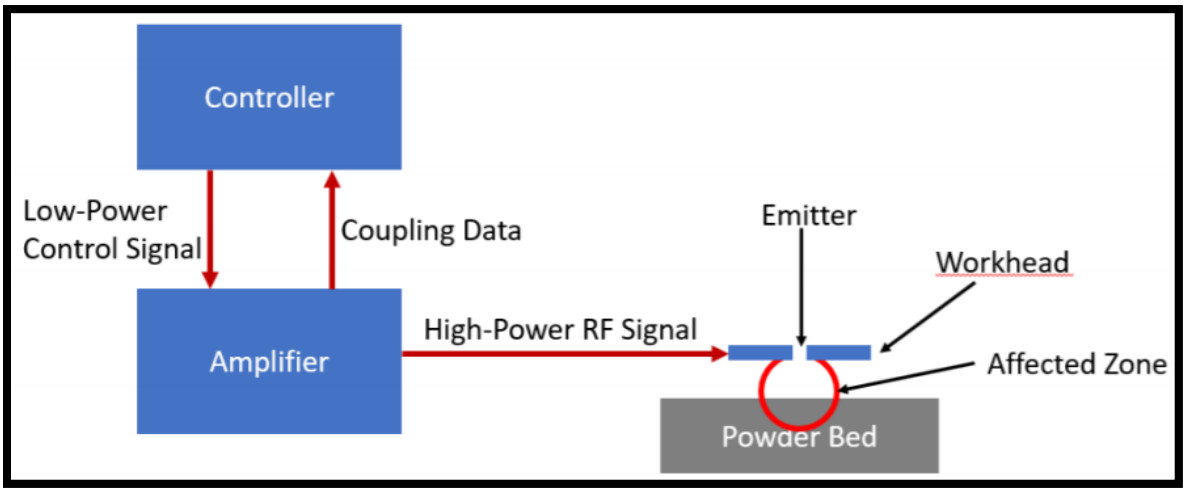

Figure 5.3: Flow of signals in the MIS system [26]

While steady advances in the field of Additive Manufacturing to address all the issues discussed above inch closer to bridge the gap, they usually come with a trade-off for cost, efficiency, or limitations with respect to application. The primary issue of controlling the thermal distribution in the powder bed fusion processes thus remains as a field of research. Taking into consideration the various research efforts this field has achieved so far, this study proposes a different approach with a familiar technique. There is enough literature and experimental analysis to support the requirement of a secondary heating source to lower the cooling rate in the powder bed depositions thus enabling extended gain growth. Induction coils have been used in multiple combinations and different end applications. This study proposes use of an induction coil in a co-axial setup along with a disk laser. While literature states a familiar approach in SLM with induction coils, this proposal defers in the working principle from the one already published and discussed ahead.

A study by Wei-Chin Huang et.al (2014) for Microstructure controllable laser additive manufacturing process for metal products makes use of a vibrating electromagnetic force to change the solidification process for a given set of SLM parameters allowing microstructure to be varied. However, the study reports the full mechanism to still be under works. Also, the study mainly focuses on metallic glass production with Additive Manufacturing alongside other non-magnetic alloys for bio-implants [27]. The schematic of the process is as shown in Fig.5.4

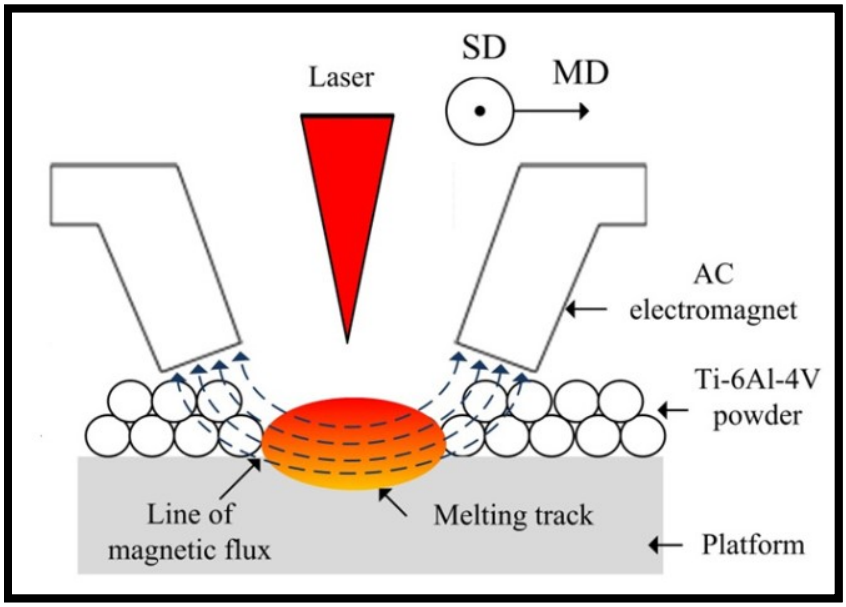

Figure 5.4: Diagram of basic SLM experimental platform with dual-magnetic-pole AC electromagnet (SD: scanning direction of laser; MD: movement direction of electromagnet) [27]

5.2 Proposed Work

The proposed work for this study can be split into four parts. Each part essentially becomes different stages in the timeline of the entire study. These four parts are as follows:

Part 1: Concept generation and numerical modelling of an auxiliary heat source.

Part 2: System design for Induction Assisted Selective Laser Melting and Coil Testing.

Part 3: Standard process parameter optimization and sample deposition for baseline data.

Part 4: Characterization of deposits and integration of ML models for the Digital Twin

5.2.1 Concept Generation and Numerical Modelling

The very basis of this study is to be able to develop a primary and secondary heating source that is cost-effective, efficient and one that can be a relatively simpler addition to the traditional SLM process. Process outputs of induction heating such as skin effect, reference depths, selective heating, etc. can be put to maximum use. All of this with minimal or no limitation to the process flow of a standard SLM process gives a unique advantage to the proposed work. Modifying the basic principle of Additive Manufacturing from rapid melting and rapid solidification to rapid melting and comparatively slower solidification due to the addition of induction can potentially help in controlling the microstructure and grain growth in the deposited samples by regulating the thermal distribution in the layer being built.

Electromagnetic induction (or sometimes just induction) is a process where a conductor placed in a changing magnetic field (or a conductor moving through a stationary magnetic field) causes the production of a voltage across the conductor. This process of electromagnetic induction, in turn, causes an electrical current [28]. The process of electromagnetic induction is unique in its own way as it actually generates heat inside a component and/or a material that needs to be heated with no effect of inertia, high-power densities and adjustable penetration depths. The working principle for Induction is a combination of two laws in physics namely: Lenz's Law and Joule's Law. When any conductive substance is immersed in a varying magnetic field generated by an induction coil, the substance carries the induced electrical current, also known as Foucault Currents. According to the Joule effect, the movement of the electrons carrying these currents dissipates the heat in the substance where they are generated [29]. The quality of the energy inducted into the workpiece

heavily depends on the placement of the inductor w.r.t. the part and vice versa, the frequency, magnetic, thermal and electric properties of the part to be heated, etc. The following factors have a pronounced effect on the way the induction system works: -

5.2.1.1 Electromagnetic Properties of the Material

Electromagnetic properties of a material is a broader expression of numerous properties that define the electromagnetic characteristics of the material. A couple of the properties which have a significant effect on induction are discussed below:

5.2.1.1.1 Electrical Resistivity - The ability of a material to conduct electricity is known as the electrical conductivity of the material, σ. The reciprocal of this conductivity is known as electrical resistivity, ρ. The resistivity of a particular metal varies with temperature, chemical composition, metal microstructure and grain size. Metals having low electrical resistivities are known as good electrical conductors. However, metals are further classified based on their resistivities as low-resistive metals (silver, copper, gold, aluminum etc.) and high resistive metals (stainless steel, titanium, carbon steel, etc.). The resistivity for pure metals is often expressed as a linear function of temperature given by the equation:

$$\rho\,(T) = 0\,[1 + \alpha(T - T0\,)]. \qquad (1)$$

Where $\rho 0$ is the resistivity at ambient temperature T0; ρ (T) is the resistivity at temperature T; α is the temperature co-efficient of electrical resistivity. The following graphs show electrical resistivities of some commercially used metals and their variation with temperature [30].

5.2.1.1.2 Magnetic Permeability and Relative Permittivity (Dielectric Constant) – Relative magnetic permeability, μr, of a material is defined as the ability of the material to conduct

magnetic flux better than a vacuum or air. Relative permittivity, ε, indicates the ability of a material to conduct electric field better than a vacuum or air. Both these properties are non-dimensional parameters, however, understanding the physics of these properties is very important while designing induction heating systems. Relative magnetic permeability has a significant effect on all basic induction phenomena including the skin effect, electromagnetic edge and end effect, proximity and ring effects, coil calculations and computation of the electromagnetic field distributions. The constant $\mu_0 = 4\pi$ x 10-7 H/m [or Wb/ (A.m)] is known as the permeability of free space. The product of relative permeability and permeability of the free space is called permeability and is the ratio of magnetic flux density (B) to magnetic field intensity (H)

$$B / H = \mu r \mu 0 \text{ or } B = \mu_r \mu_0 H. \qquad (2)$$

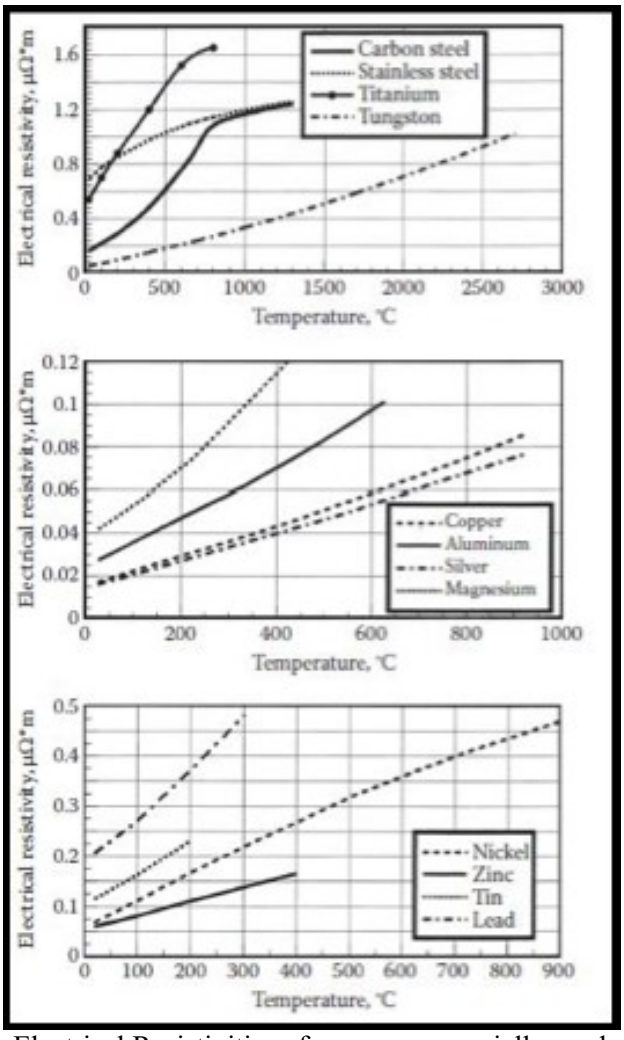

Figure 5.5: Electrical Resistivities of some commercially used metals [30]

Based on the magnetization abilities, all materials are classified as paramagnetic, diamagnetic and ferromagnetic materials. Relative magnetic permeability of paramagnetic materials is slightly greater than unity. For diamagnetic materials, it is slightly less than 1. However, ferromagnetic materials exhibit very high values of relative permeability ($\mu r >> 1$). Ferromagnetic properties of a material heavily depend and are a complex function of structure, chemical composition, prior treatment, grain size, frequency, magnetic field and temperature. For example, a same kind of

carbon steel at same temperature and frequency will have different values of relative magnetic permeability due to differences in the magnetic field intensity [30].

5.2.1.2 Skin Effect

The current distribution in a conductor carrying direct current is always uniform throughout its cross-section. However, when an alternating current is passed through the same conductor, there is uneven distribution of electric current. The maximum value of current density will always be found at the surface of the conductor. This density goes on decreasing from the surface towards the core of the conductor. This phenomenon of non- uniform distribution of current within the conductor's cross-section is known as skin- effect. As a result of this, skin effect is also found in the workpiece meant to be heated / treated through induction, due to the presence of an alternating current. This is one of the major reasons behind the concentration of eddy currents on the surface (skin) layer of the workpiece. In electrical applications, approximately 86% of the power is found to be concentrated in the surface layer of the conductor. This layer is known as the reference (or penetration) depth, δ. The extent of skin effect depends on the frequency of the system and also the material properties of the conductor.

$$\delta = 503\sqrt{\frac{\rho}{\mu_r.F}} \qquad (3)$$

Where δ is the penetration depth in meters, ρ is the electrical resistivity of the metal (Ω*m), μ_r is the relative magnetic permeability and F is the frequency in Hz [30].

5.2.1.3 Electromagnetic Proximity Effect

In most applications and systems, a current carrying conductor never stands alone. It is usually surrounded by other current carrying conductors or conductive materials. In such cases, the current and power density distribution gets distorted and is never uniform. This effect of the proximity of two current carrying conductors on their respective electromagnetic fields is known as the electromagnetic proximity effect. Figure 5.6.a shows a representation of the skin effect in a conductor standing isolated. However, when another current carrying conductor is placed close to this conductor, the currents in both these conductors redistribute. If the currents flowing in both these conductors have opposite directions, then due to the skin effect, both currents will be concentrated in areas facing each other, as shown in Figure 5.6.b. This results in a strong magnetic field in the area between the two conductors. This results because of both the conductors having their respective magnetic field lines in the same direction. Due to a strong internal magnetic field, both these conductors will have a weak external magnetic field. On the other hand, if the currents flowing in the conductors have the same direction, the both the currents will be concentrated in areas opposite to each other, as shown in Figure 5.6.c. This would result in a weak magnetic field in the area between the two conductors. However, due to a weak internal field, both these conductors will have a very strong external magnetic field.

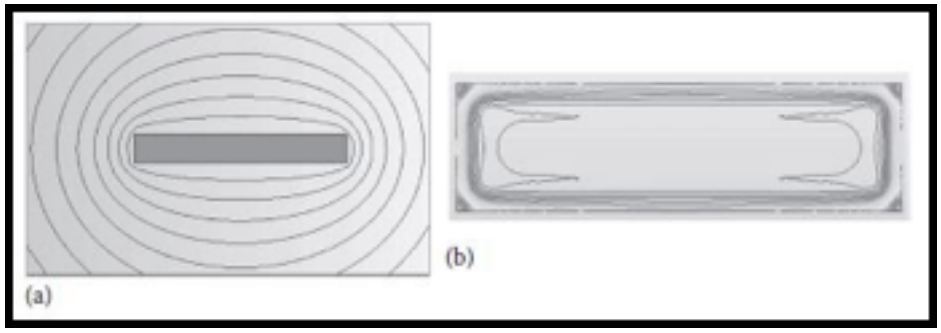

Figure 5.6.a: - (a) Magnetic field & (b) Current density distribution in a stand-alone conductor [30]

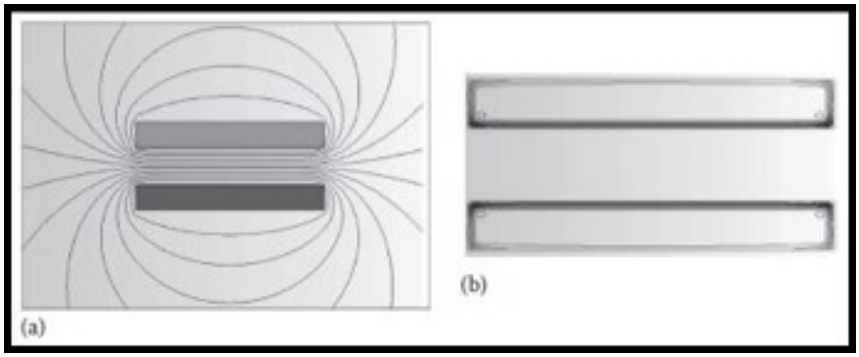

Figure 5.6.b: - (a) Magnetic field and (b) Current density distribution in conductors with current in same directions [30]

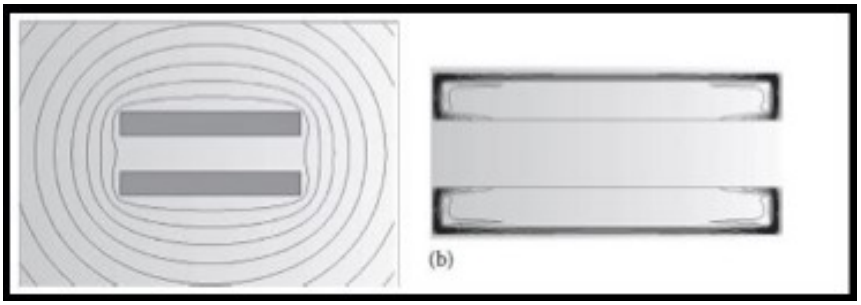

Figure 5.6 c: - (a) Magnetic field and (b) Current density distribution in conductors with current in opposite directions [30]

The phenomenon of proximity effect finds a direct application in Induction Heating. Here, the first conductor is the inductor carrying the current and the second conductor is the workpiece. According to Faraday's law, the direction of the eddy currents induced in the workpiece would be

in the opposite direction as that of the inductor. This, as per the proximity effect, would lead to a strong magnetic field between the inductor and the workpiece due to the eddy currents concentrating in the areas of the conductors that face each other [30].

5.2.1.4 Basic Thermal Phenomena in Induction Heating

The thermal properties of the materials play an important role in deciding the system requirements and parameters for induction heating. The Thermal Conductivity k defines the rate at which heat travels across a thermally conductive workpiece. In order to obtain a uniform thermal distribution, a metal with a higher thermal conductivity is preferred. However, in cases of selective heating, metals with higher k values may become a disadvantage. Metals with higher thermal conductivities have a tendency to promote soaking action and equalize thermal distribution within the workpiece. As a result of this, temperature rise not only takes place in the region of interest but also in areas surrounding it. Due to this, higher power is required to attain the desired temperature rise in the region of interest. Moreover, higher temperatures always bring in the possibility of geometric distortions in the workpiece.

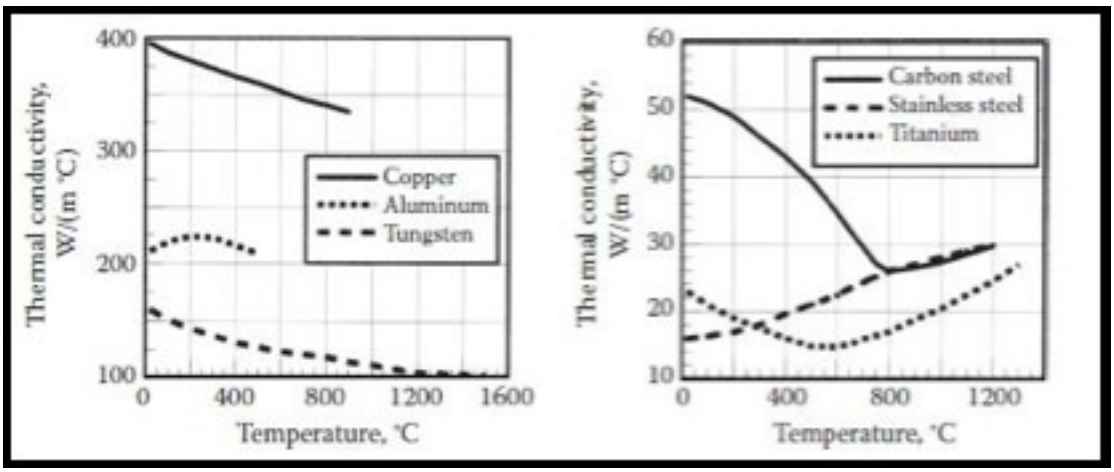

Figure 5.7: Thermal conductivities of metals Vs Temperature [30]

Similarly, the value of heat capacity C indicates the amount of energy that the workpiece would absorb in order to achieve a unit rise on temperature. Mathematically, C = dQ/dT Where dQ is the required energy and dT is the required temperature change. Heat capacity is closely related to a parameter called specific heat c which represents the heat capacity per unit mass i.e., the amount of energy absorbed by a unit mass of the workpiece to achieve a unit temperature increase [30].

5.2.1.4.1 Modes of Heat Transfer

Induction heating is characterized by three modes of heat transfer namely conduction, convection and radiation. Each mode of heat transfer plays a significant role depending on the nature of their application. They are discussed briefly as follows:-

5.2.1.4.1.1 Thermal Conduction

Heat Transfer through this mode takes place by conduction of heat from higher-temperature regions to lower-temperature regions as per Fourier's law,

$$q_{cond} = -k \, \mathrm{grad}(T). \qquad (4)$$

Where qcond is the heat flux by conduction and k is the thermal conductivity. As seen from the above equation, the rate of heat transfer through conduction is directly proportional to the temperature gradient and thermal conductivity of the material or the workpiece [30].

5.2.1.4.1.2 Thermal Convection

Heat transfer through convection is governed by Newton's law which states that the heat transfer rate through convection is directly proportional to the temperature difference between the workpiece surface and the ambient area. It is expressed as follows:

$$q_{conv} = \alpha (T_s - T_a). \qquad (5)$$

where qconv is the heat flux density by convection, α is the convection surface heat transfer co-efficient, Ts is the surface temperature and Ta is the ambient temperature. The convection surface heat transfer co-efficient is a function of the thermal properties of the workpiece and the surrounding fluids (gas or air). This mode of heat transfer becomes important when designing low-temperature induction systems (500 deg.C or less) as the convective losses in these applications are equal to or exceed the heat losses due to radiation [30].

5.2.1.4.1.3. Thermal Radiation

Thermal Radiation may occur due to heat transfer from the workpiece to the surrounding that include a non-material region (vacuum). The phenomenon of thermal radiation is often described as the propagation of electromagnetic energy due to a temperature difference. It is governed by the Stefan-Boltzmann law which states that the heat transfer rate by radiation is proportional to a radiation loss co-efficient Cs and the value of $T_s^4 – T_a^4$. As can be seen, since the radiation losses are directly proportional to the fourth power of temperature, these losses form a significant part of the total losses in high-temperature applications [30].

5.2.1.5 Magnetic Flux Control Techniques

Flux is defined as the rate of transfer of fluid, particles or energy across a given surface interface. Magnetic flux is a measure of the total number of magnetic field lines crossing a chosen surface. Even if magnetic flux lines cannot be seen, they can be represented in the form of mathematical calculations and graphs. Since an isolated magnetic source has never been observed to exist, the net flux of the magnetic flux density vector (B) is always zero. Therefore, the lines of a magnetic field are closed loops and for a given volume, the number of lines entering the volume will always

be equal to the number of lines leaving the volume. There are several ways through which the position of these lines can be altered. The density can be changed by changing the cross-section through which these lines pass or through which the flux flows. The positions of these lines can also be changed by making use of some special materials that give a different path for the flux to flow or restrict the path of the magnetic flux. The third way is to introduce another current-carrying conductor in the vicinity and then due to the proximity effect, the magnetic flux lines are altered [30].

5.2.1.5.1 Electromagnetic Shunts

Magnetic fields in induction heating are generated with the purpose to heat a metal workpiece. However, the field often ends up heating not only the workpiece but also the metal surrounding the coil and workpiece. In order to avoid this, it becomes necessary to make use of magnetic shields to reduce the effect of magnetic field and to protect other structures, components or equipment coupling to the coil [30].

5.2.1.5.2 Magnetic Shunts

Magnetic shunts usually consist of large stack of thin steel laminations placed along the axis of the inductor. These provide a parallel and low reluctance path for the magnetic flux. Shunts reduce the external magnetic field and prevent heating of the surrounding metal components when used along with heating coils. They can also be a good source of significant power dissipation in the system and can be cooled by water [30].

5.2.1.5.3 Magnetic Flux Concentrators

The main intent of the flux concentrators in induction is to improve the magnetic coupling efficiency and to achieve effective selective heating in workpiece areas that are either complex in

geometry or difficult to heat. In the absence of a flux concentrator, the magnetic flux may spread around the coil or current-carrying conductor and may couple with it. The concentrator forms a magnetic channel for the magnetic flux of the coil in a desired area outside the coil. This happens mainly due to the conductor's current getting concentrated on the surface facing the workpiece. This current concentration leads to good coil workpiece coupling and therefore improves the coil efficiency by reducing any losses that might occur otherwise. The actual current distribution heavily depends on frequency, magnetic field intensity, geometry and material properties of the conductor, workpiece and also the concentrator. Flux concentrators help in improving the efficiency of the process partly by reducing the coupling distance between the conductive part of the coil and the workpiece. They also reduce the stray losses by reducing the reluctance of the air path. However, the conduction of high-density magnetic flux in the concentrators also generates heat inside the concentrator due to the Joule effect. This leads to a drop in the electrical efficiency. The overall change in the efficiency is a result of the above mentioned three factors. As a result of this, appropriate use of the magnetic flux concentrator becomes necessary to achieve a higher process efficiency. This also results from the concentrator's potential to concentrate magnetic field in a certain area due to which the field does not propagate behind the concentrator. The collective effect of which, the heated mass or area of the metal is smaller, and the desired heating pattern is achieved [30].

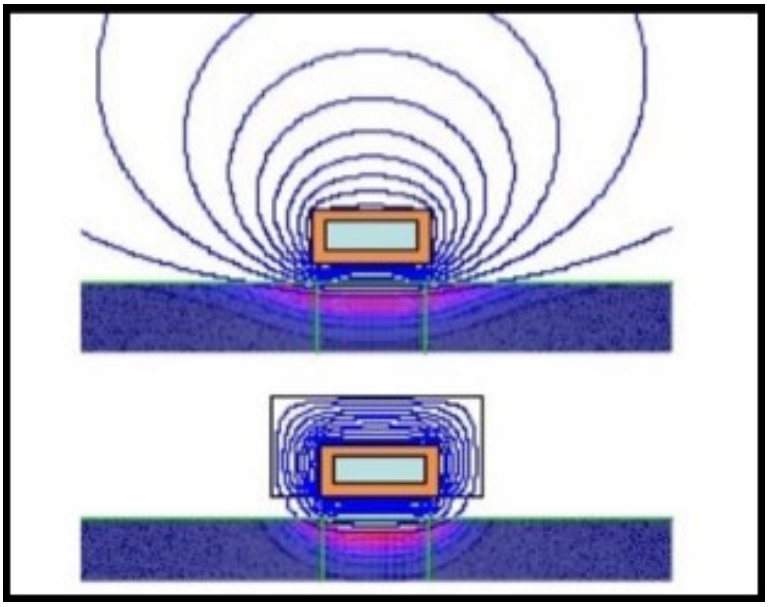

Figure 5.8: Magnetic field without concentrator and with concentrator [31]

5.2.1.5.3.1 Selection of Flux Concentrator Materials

Selection of a material for the flux concentrator is influenced by many factors including electrical resistivity, thermal conductivity, relative magnetic permeability, curie point, saturation flux density and ductility. Additional factors include machinability, formability, resistance to any chemical reactions, ability to withstand high temperatures, etc. The materials under consideration should have a high slope of magnetic permeability and a high saturation flux density. Magnetic materials with high electrical resistivities reduce eddy current losses of the concentrator thereby reducing its temperature increase. Having a higher thermal conductivity helps in overcoming local over-heating that is caused, at times, due to radiation from the heated workpiece or high-density flux in some areas of the concentrator. The most commonly used type of materials as flux concentrators are as follows:

1. Laminations

2. Electrolytic iron-based materials

3. Carbonyl iron-based materials

4. Pure ferrites and ferrite-based materials

5. Soft formable materials

The use of soft formable materials helps in ease of molding of flux concentrators as per desired shape and size and later machining, if needed, to exact tolerances. One such material is Alphaform which is an advanced composite made of insulated iron microparticles, space-age polymers and a thermally sensitive catalyst.

Some of the advantages of using flux concentrators are listed as follows:

1. Reduce the operating power levels required to obtain the desired heating of the workpiece.
2. Improve the electrical efficiency of the process and decrease the amount of energy used.
3. Make selectively heating of specific areas of the workpiece possible.
4. Obtain a superior heat pattern and improve the physical and metallurgical properties.
5. Minimize geometric distortion of the workpiece.
6. Prevent undesirable heating of the adjacent parts or areas of the workpiece.
7. Improve equipment life.
8. Reduce cycle time [30].

5.3 Application of Induction to Control Thermal Distribution in AM

As discussed in the previous chapters, controlling the thermal distribution in the powder bed becomes extremely crucial in terms of porosity control, formation of residual stresses, crack initiation, curling, balling and the overall build quality of the parts. Also, significant enhancements

in the material properties of the powder metal can be achieved by maintaining constant thermal cycles and temperature profiles throughout the process. Techniques have been developed in order to address the thermal distribution and the issues that follow with it. Research has been made where induction coils are introduced along the walls of the powder bed to control the variation of temperature at different depths of the powder bed in order to achieve a gradual thermal gradient during the process [32]. Induction to heat the powder instead of heating the entire bed is proposed through this study after taking into consideration the benefits of Induction heating that can be suitably applied to the Additive Manufacturing process. The introduction of induction coils to selectively heat the powder substrate will not only help in minimizing the power usage due to lower requirements of laser power, no arrangement required to maintain the powder-bed temperature but also as a result of this, will increase the process efficiency. In a typical SLS setup, as the powder bed is heated, the powder that acts as a support structure to the part being built cannot be re-used directly. This is because the powder undergoes thermal variation throughout the build-time of the process reducing its material properties. Due to this, post-processing of the unused powder becomes necessary if the same powder needs to be re-used. This also calls for time-delays in production. The unique advantages of induction such as the skin effect, reference depths thus become operational parameters and, therefore, they can be tuned to optimize the process as per the requirement. Also, the quick response time of metals while heating through induction helps in reducing the cycle time of the process.

However, the use of induction heaters and coils in AM processes isn't new. Various studies have demonstrated the use of induction coils to either pre-heat or post-heat the powder bed or the base metal. Base metal pre-heating is one of the most commonly used methods to address the defect formation in the deposition of metal parts through different AM techniques. Baseplate pre-heating

helps in maintaining the uniformity in the material temperature during the deposition process and reducing thermal and residual stresses through lowered cooling rates [33]. In addition to this, preheating the baseplate or the powder can also lead to changed microstructures and resulting material properties. Studies have also been carried out employing a high temperature L-PBF process employing constant preheating throughout the build process as the build platform gets lowered during the deposition process. This is achieved with the use of a helical coil surrounding the build chamber and controlling the thermal gradient as the part is being built [34].

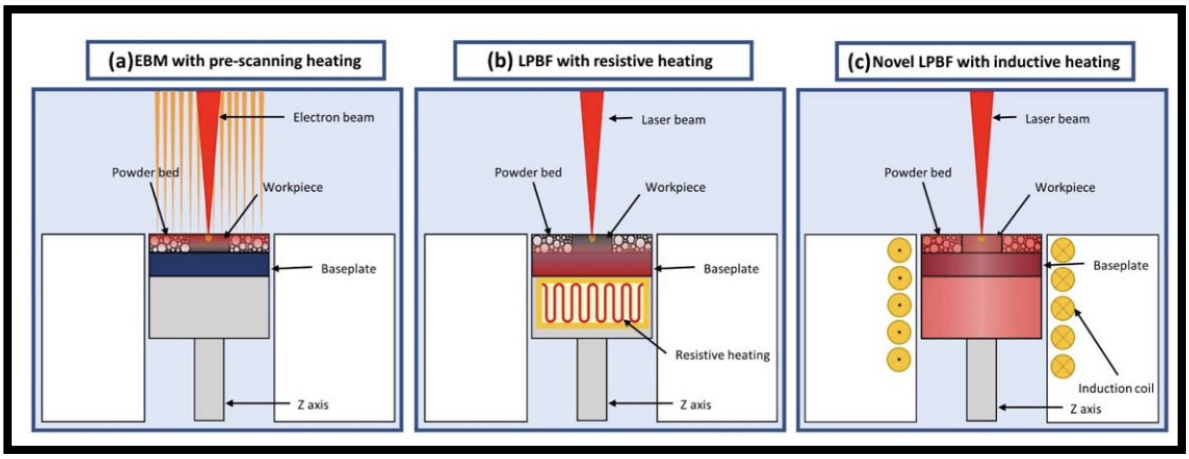

Figure 5.9: Conceptual layout design of (a) EBM with pre-scanning heating (b) LPBF with standard resistive preheating system and (c) novel LPBF with inductive heating system [34].

One of the most important factors of this proposition lies in achieving a desired temperature rise within a minimal heat affected zone (HAZ) in shortest time possible. To achieve this, flux concentrators are also used to increase the flux density and channel it through the path requirement for a given geometry. Based on the literature and concept generation in the previous chapters, the next step in this study was to run simulations of induction with a process specific induction coil, determination of process parameters for induction and also study its effects on different substrates.

The coil design had to be small and lightweight in order to be able to accommodate the coil in any complex working environment. The first step in this stage was to model simulations for a simple cylindrical coil. COMSOL Multiphysics 5.3a was used to simulate the induction process with the Heat Transfer in Solids and the AC/DC modules.

5.3.1 Coil Geometry Design

Specifically designed and configured coils with single or multi-turns are usually preferred for medium to high range of induction frequencies. These design modifications are obtained by making changes to the simple geometrical contours. Given the higher conductivity, lower resistivity and its cold and hot working abilities, most of the coils fabricated for induction heating are made from copper. These copper tubing's are available in different types of cross-sections and sizes based on their availability and application. In addition to this, apart from its own I^2R losses, the radiation and convective heat transferred from the workpiece also needs to be considered while choosing the tubing size and cross-section. This is specifically important to maintain effective cooling of the coil while in operation [35].

5.3.2 Coil Shape

Solenoid and conical coil geometries are taken into consideration to study their effective magnetic fields thus determining the coupling efficiency based on the time required for the work piece to heat up. Studies suggest that while both the coil geometries generate a distributive magnetic field pattern around their respective geometries, the high intensity of the field at the center follows a gradual decrease as the point of consideration moves away from the center towards the boundaries

of a solenoid coil. The conical coil, on the other hand, produces a better magnetic field in a single direction. This is achieved based on the nature of the coil geometry that generates a stronger magnetic field towards the tapering end of the coil converging the maximum flux lines [36]. The use of an induction coil in a Laser Powder Bed Fusion (L-PBF) process limits the coil geometry to smaller dimensions. This helps towards making minimal changes in the L-PBF nozzle and optics system. This stands true for the baseline simulation comparisons for the solenoid and conical coil geometries.

The simulation parameters and constants are mentioned in Table No.5.10. Preliminary in-built geometry module from COMSOL is used to model the coil geometries and the current input is assumed to be on the surfaces of the coils. Furthermore, appropriate Multiphysics models are chosen to ensure correct physical coupling of the geometries is obtained for determining accurate conclusions.

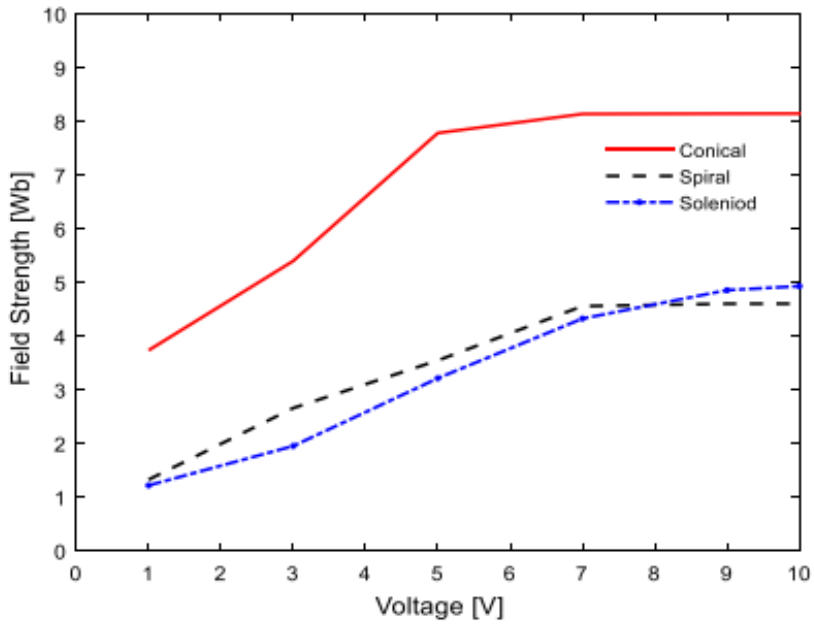

Figure 5.10: Fundamental parameter analysis of conical, spiral, and solenoid coils as a function of excited dc voltage. Measurement of the magnetic field in the center axis of three different shaped coils [36]

Parameters	Values / Descriptions
Induction Frequency	340kHz
Induction Current	60A (20A, 40A, 80A and 100A) (v)
Coil movement	Stationary
Coil standoff	0.125in
Baseplate dimensions	4.5* 4.5* 0.125in
Simulation environment envelope	Air / Argon (6* 6* 6in)
Induction duration	20 secs
Coil Tubing size	-0.125in -0.25in (v)
COMSOL Modules	-Magnetic Fields - Heat Transfer in Solids

Table 5.1: Induction simulation parameters and details
(v): Variation studied as a parameter influencing design decision

Taking into consideration the application requirement and conclusions from the literature survey, an in-depth simulation study is carried out for the conical coil geometry and its comparison to an equivalent solenoid coil. A SS316 plate is considered for the simulation of all the coils and its variations. However, material variation is taken into consideration towards the later stages of numerically modelling the design optimization process of the coil.

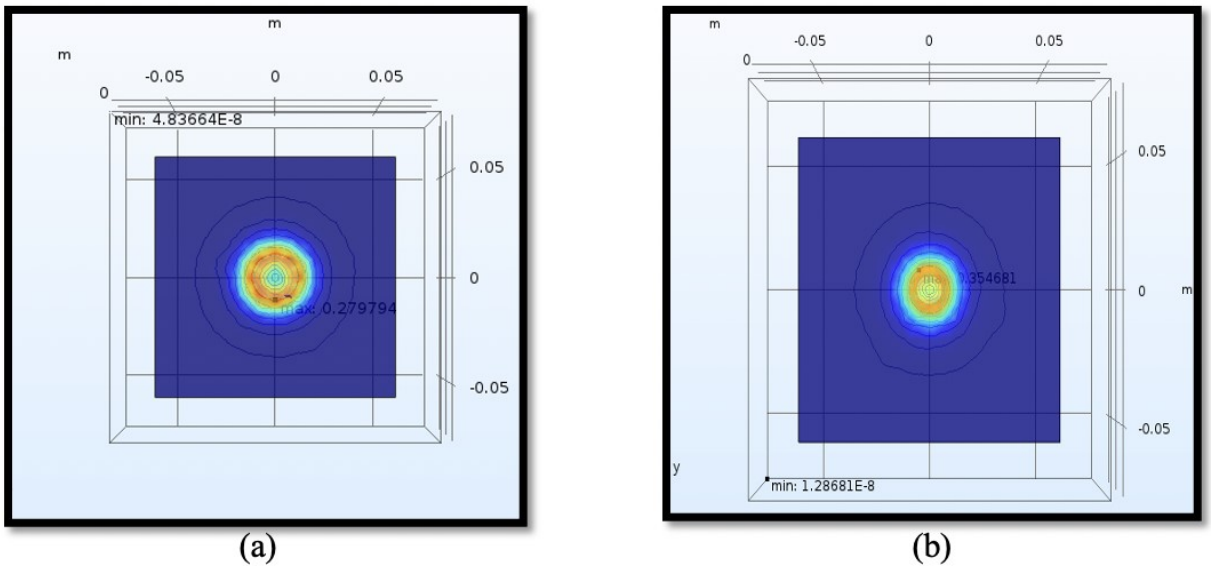

Figure 5.11: (a) Top view of a solenoid coil showing the spatial spread of the magnetic field and (b) Top view of a conical coil showing the spatial spread of the magnetic field

The baseplate (work piece) modelled for the simulations is designed in accordance with the maximum build area available in the in-house built powder bed for the L-PBF process. Therefore, for a fixed baseplate dimension, coil height and coil-work piece stand-off, it can be clearly seen from Fig.5.11, the spatial distribution of the magnetic flux density on the baseplate for a solenoid coil to be much greater as compared to that of the conical coil. It thus concludes that the distribution or "spread" of coupling of the solenoid coil is far greater than of the conical coil. This is well supported by the significant difference in their radiosity values which stand at 8.7922×10^5 W/m^2 and 2.0362×10^6 W/m^2 for the solenoid and conical coils respectively. The higher concentration of the flux lines towards the center of the solenoid coil makes it the most suitable for internal heating applications. As a result of this, a conical coil geometry is considered best suitable for the proposed work. The next step, then becomes, to vary the different aspects of the conical geometry of the coil.

5.3.3 Coil Angle

The approach in modelling the conical coils in COMSOL for simulating the various geometric features is set within the design regulations for the proposed system. The base radius of the coil (larger end of the cone fulcrum) is fixed with a corresponding maximum height for the coil. This maximum height is then justified with respect to the number of turns of the coil winding and the tubing size used to fabricate the coil. The coil angle is then varied w.r.t to this fixed base radius and coil height. The lowest coil angle (0°) corresponds to the standard solenoid coil and a higher coil angle adds more taper to the conical feature of the coil. The bottom (smaller) radius of the coil is thus a function of the coil angle. This, in turn, limits the higher end of the coil angle to allow for

a considerable bottom radius of the coil so that fabricating the coil and its integrated functioning with the laser becomes possible. For the simplicity and better understanding of the simulations, the coil angle is varied in steps of 2° and for each increment, the magnetic flux density and the maximum temperature value are noted at the end of the 20 seconds of the simulated induction time. Both, the baseplate, and the coil are kept stationary to study the coupling time and the final temperature rise. An input current of 60A is pre-determined based on the actual system specification to be used to test these conical coils after the completion of the simulation study.

Coil Type	Coil Angle (°)	Magnetic Flux Density (T)	Temperature (°C)
Intermediate	10	0.3152	2028.77
	12	0.3177	2020.51
	14	0.3843	1963.58
	16	0.3546	2596.03

Table 5.2: Variation of Magnetic Flux Density and final temperature with increase in coil tilt angle.

The study is concluded at a maximum of 16° coil angle given the design restraints discussed above that regulate the bottom diameter of the fulcrum of the cone. A higher coil angle leads to a relatively smaller diameter at the smaller end of the conical coil. Also, a steady decrease in the magnetic flux density is observed as higher coil angles are simulated. Owing to two these two considerations, a 16° conical coil angle generates the maximum surface temperature rise on the baseplate of 2576°C (starting temperature is assumed to be 20°C) and a comparable magnetic flux density, as can be seen from Table No.5.2. Figure 5.12 shows a comparative illustration of the HAZ and the maximum temperature rise of the baseplate at the end of 2 mins.

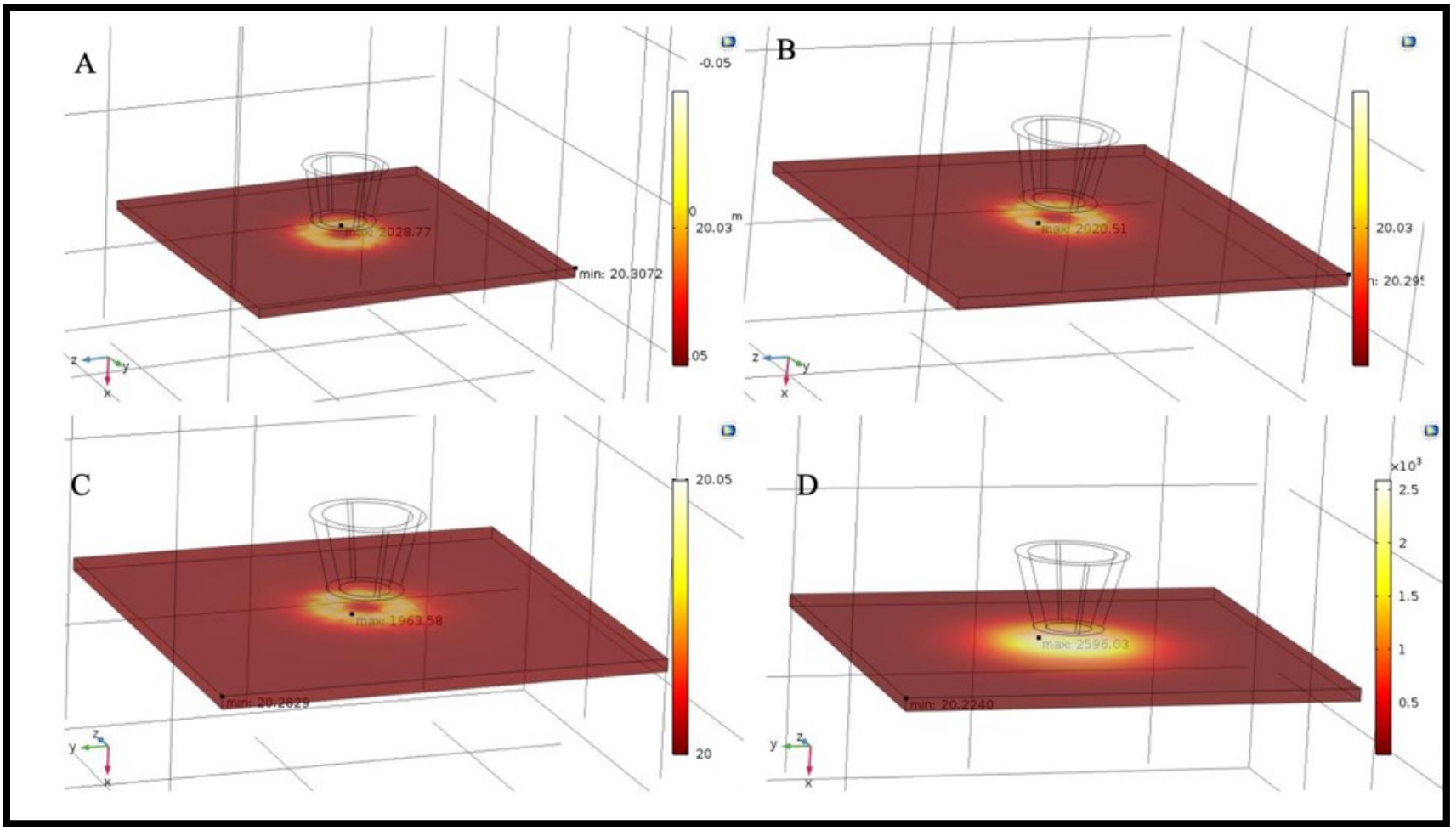

Figure 5.12: Temperature rise and distribution of a conical coil with a coil angle of (A)10°, (B) 12°, (C) 14° and (D) 16°

5.3.4 Input Coil Current

The coil input current has a direct relation on the magnetic field density induced in the workpiece. The conical coil with a 16° coil angle is studied for the effect of increment of the input current for the coil on the magnetic flux density variation and resulting temperature rise. This is carried out in stages of current increments of 20A. The maximum current value simulated is restricted to 60A owing to the restrictions of the actual system specification as mentioned in the previous section. The resulting data is summarized in Table No.5.3.

The plot of the coil power vs induction current in Fig.5.14 is a clear indication of the non-linear trend of the coil power with increasing current. This can be related to the electrical resistivity of the material which is a temperature-dependent property. A higher current reduces the resistivity of the material as the temperature in the baseplate (workpiece) goes up.

Coil Type	Input Current (A)	Coil Power (W)	Magnetic Flux Density (T)	Temperature (°C)
Intermediate	20	5.05	0.1182	483.55
	40	20.2	0.2364	1631.03
	60	45.4	0.3546	2596.03
	80	**80.8**	0.5279	3265.52
	100	**126**	0.6599	3813.58

Table 5.3: Variation of Magnetic Flux Density, Coil Power and final temperature as a function of increasing current.

While induction current values higher than 60A are not available on the physical system, the simulated values, on the overall (80 & 100A), highlight the trend in the rise of the coil power as resistivity goes on decreasing.

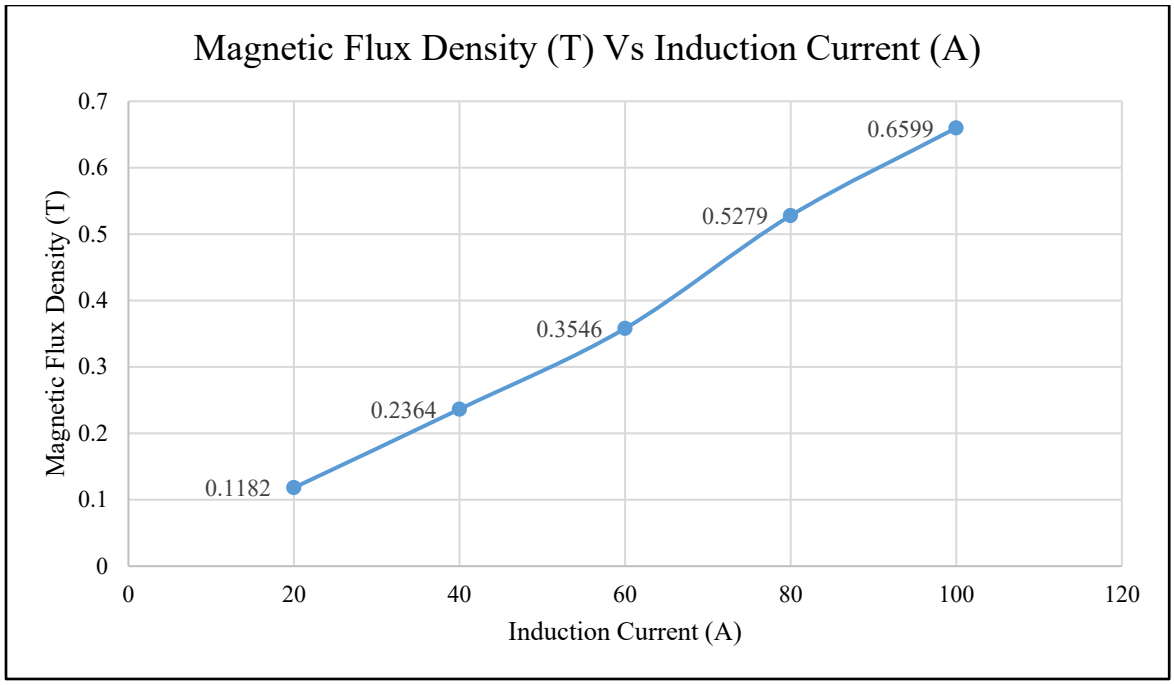

Figure 5.13: Magnetic flux density Vs Input Induction Current of a conical coil with a coil angle of 16°

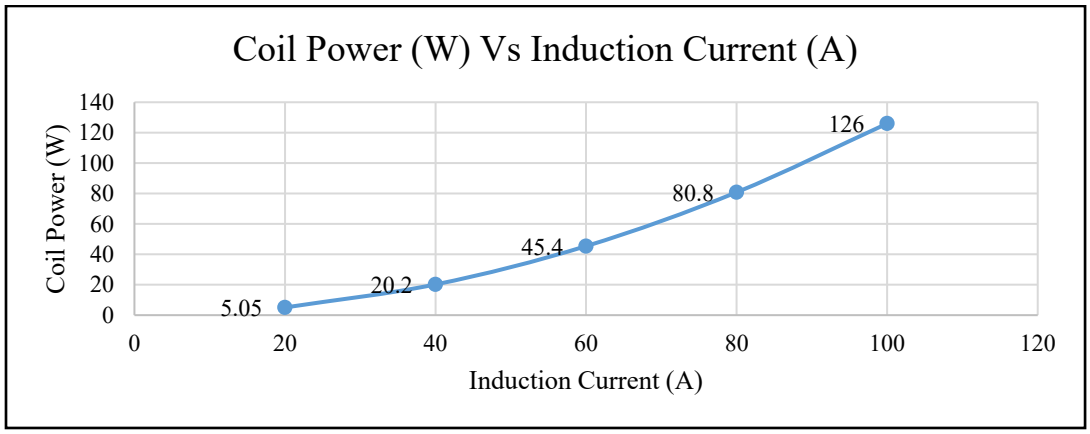

Figure 5.14: Coil Power Vs Input Induction Current of a conical coil with a coil angle of 16°

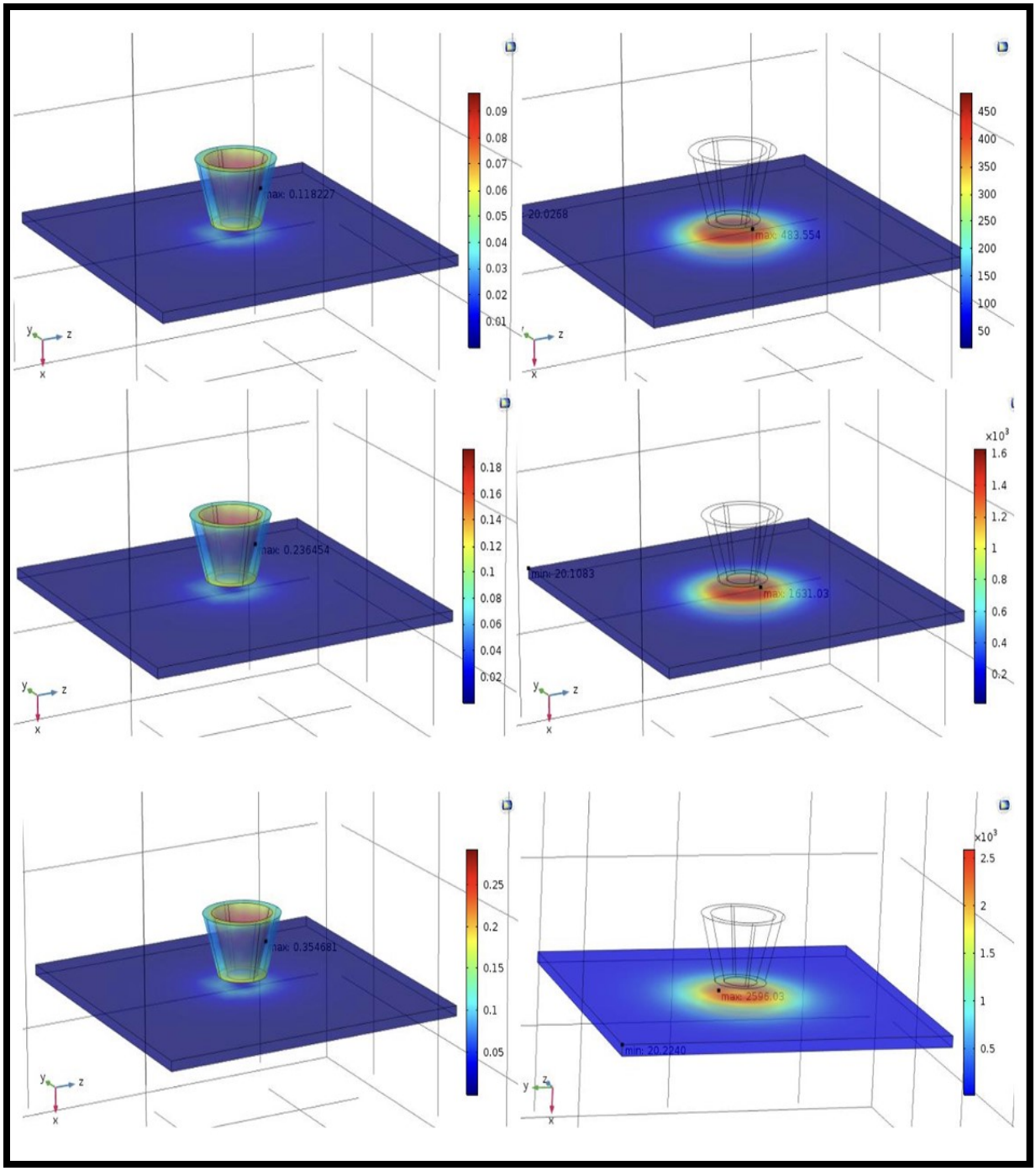

Figure 5.15: Magnetic Flux Density (T) (left column) and Temperature variation (°C) (right column) Vs Input Induction Current (20 to 60A) of a conical coil with a coil angle of 16°

5.3.5 Coil Height and Tubing Size

The coil height and tubing size plays an important role not only in determining the efficiency of the coil but also in deciding the design boundaries for the induction system. In the case of this proposed work, the overall height was varied for a fixed current input of 60A and a fixed coil angle of 16°. Given the compactness of the coil in terms of its height and width, the tubing size of the copper coil used to simulate its various geometric features so far have been kept constant at 0.125in. in diameter. Modelling this coil tubing size to a 0.25in diameter to study the effect of the change on the resulting temperature rise was carried out alongside lowering the overall height of the conical coil. The results for the same are tabulated in Table No.5.4 and Table No.5.5.

Coil Type	No. of turns	Magnetic Flux Density (T)	Temperature (°C)
Intermediate	4	0.2847	2449.22
	6	0.3546	2596.03

Table 5.4: Lowering of coil height and its resulting final temperature (°C) and the corresponding Magnetic Flux Density (T)

Coil Type	Tubing size (in)	Magnetic Flux Density (T)	Temperature (°C)
Intermediate	0.125	0.3546	2596.03
	0.25	0.0269	30.2

Table 5.5: Change of coil tubing size and its resulting final temperature (°C) and the corresponding Magnetic Flux Density (T)

A sharp fall in the coupling efficiency is observed as the tubing size of the modelled coil is changed from 0.125in to 0.25in. This is observed in terms of both, the magnetic flux density and the final temperature achieved. This is also due to the increased surface losses of heating due to a larger diameter tubing. On the other hand, the selection of a bigger tubing size also leads to fabrication issues. The minimum bending diameter is significantly reduced as the size of the tubing is doubled

(0.125in to 0.25in). As a result of this, special forming operations need to be incorporated. One of this is done through filling the coil tubing with sand or salt to avoid crimping of the coil turns. Once the final geometry of the coil is achieved, the sand or salt can be cleared through the tubing by passing water.

As a result, the minimum tubing diameter of 0.125in is fixed for the coil design with 6 turns of coiling at an angle of 16°. The next steps consist of determining the stand-off between the coil and the baseplate.

5.3.6 Coil and Baseplate Stand-off and Material Variation

With a fixed coil geometry for the proposed concept, the stand-off between the coil and the baseplate are now varied. The stand-off for all the simulations so far is at a constant 0.125in. This stand-off is now varied in two increments of 0.125in and the resulting temperature values are tabulated in Table No. 5.6.

Coil Type	Baseplate Material	Coil Stand-off (in)	Magnetic Flux Density (T)	Temperature (°C)
Intermediate	SS 316	0.125	0.3546	2596.03
		0.25	0.3605	1372.51
		0.375	0.3634	572.14

Table 5.6: Change of coil stand-off and its resulting final temperature (°C) and the corresponding Magnetic Flux Density (T)

While the geometry of the coil has been optimized throughout the course of this simulation study, the baseplate (workpiece) material has been kept the same. SS 316 has been chosen as the material of choice for the simulation study so far given its austenitic nature that makes is magnetic properties on the weaker side of the spectrum. As a result, this leads to true optimization of the

coil design for the proposed system in terms of coupling a material that is non-magnetic in behavior. A basic simulation is also carried out on SS410 and yields similar results as compared to that of SS 316. This signifies the design optimization of the coil for its martensitic and austenitic applications. The result is as follows:

Coil Type	Baseplate Material	Magnetic Flux Density (T)	Temperature (°C)
Intermediate	SS 316	0.3546	2596.03
	SS 410	0.3545	2218.68

Table 5.7: Change of baseplate material and its resulting final temperature (°C) and the corresponding Magnetic Flux Density (T)

This concludes the basic coil design optimization simulation study for its use with a SS 316 baseplate. A conical coil geometry is now fixed with a 16° coil angle, at a total coil height of 0.75 in (6 turns of a 0.125in coil tubing) operating at a maximum induction current of 60A. The material of choice for the coil tubing is copper owing to the various material advantages copper possesses. Given its very low resistivity, fully annealed and high conductivity copper becomes the most common choice in most of the induction heating applications. The easy availability in different cross-sections also gives an added advantage.

Chapter 6. Induction Assisted SLM System Development

6.1 Coil Design and Testing

The geometric feature results of the conical coil simulation study form the basis of the Part 2 of the proposed study for the design and fabrication of the Induction assisted Selective Laser Melting (ISLM) system. Based on the conical coil angle and height of the coil, a cone fixture with threads to turn the copper coil was designed. The coil fixture was designed to accommodate 10 turns throughout its end-to-end height. This coil fixture could then be divided into different sections as per the design revisions of the coil based on the coil height. For an in-depth study of the coil design variation, the fixture can turn “small, intermediate and big” coils on the same fixture. These coils were distinguished based on the smaller cone-fulcrum diameter requirement for designing the system while still maintaining the simulated geometric results for the coil design. The coil fixture was fabricated through Rapid Prototyping techniques (Fused Deposition Modelling). A simple two-dimensional illustration of the coil fixture is as shown in Fig 6.1.

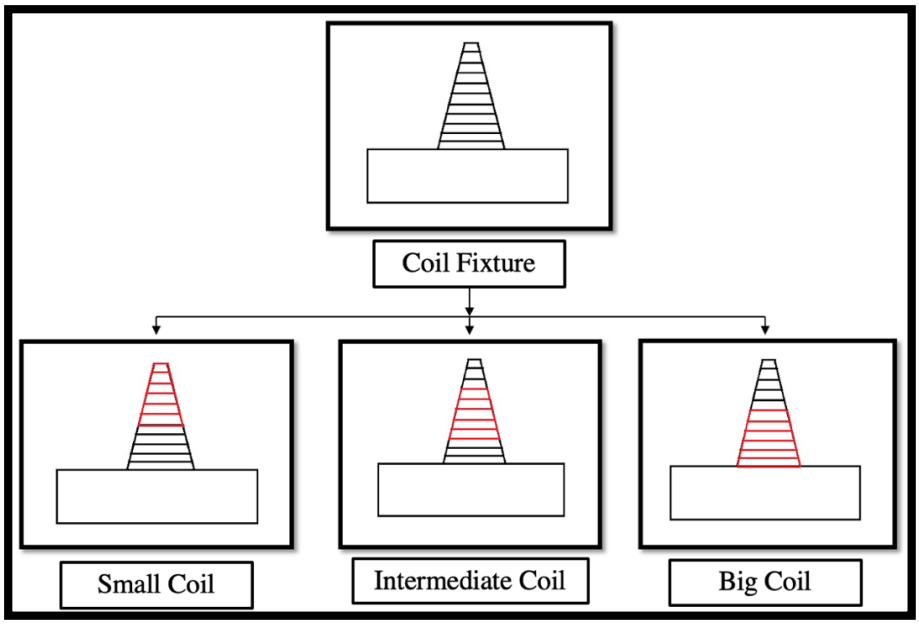

Figure 6.1: Coil fixture 2D illustration with three coil design divisions

The red features in Fig 6.1. shows how the same coil fixture can be used to turn coils of different sizes but still have the same coil angle. However, the small and the big diameters of the conical coil change. This means that the overall Heat Affected Zone (HAZ) due to the coil increases or decreases. The results of the simulations are based on the intermediate coil design specifications. The turning of the coil is carried out with a 1/8" in. copper coil procured from McMaster Carr. The coil fixture is clamped onto a table and the coil tubing is turned around the fixture with the help of the threads on the fixture. As copper work hardens with increasing deformation, the threads make the entire turning process quick and easy as the tubing easily grips around the coil fixture assuming the required conical shape. An example of the coil turned on the coil fixture can be seen in Fig 6.2.

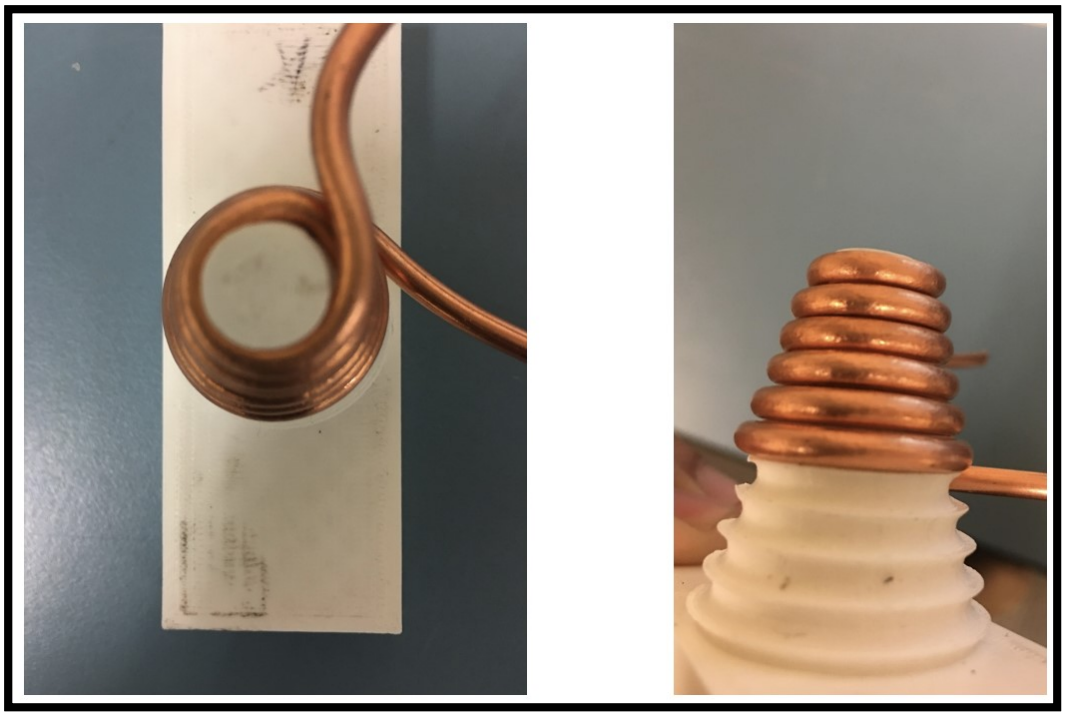

Figure 6.2: Coil fixture with a “small coil” turned for demonstration purposes

Once the turning process is complete, the coil can be removed from the fixture by simple unscrewing. The leads of the coil are crimped to cut and then the ends are re-formed close to their starting internal diameter. This ensures a minimal internal opening is maintained for the cooling water to flow throughout the coil. The coil ends are connected to the induction system by the means of nuts compressing the ferrules and back sleeves ensuring proofing against water leaks.

One of the most important factors of this proposition lies in achieving quick coupling of the coil with the baseplate and the metal powder with a minimal heat affected zone (HAZ). To achieve this, flux concentrators are used to not only increase the flux density but to also channel it through the path requirement for a given geometry. Alphaform MF from Fluxtrol Inc. is used as the flux concentrator due to its material properties aligning with the process requirements. The following table gives an overview of the properties of Alphaform MF:

Properties	Units	Alphaform MF
Density	g/cm3	4
Maximum Permeability	none	10
Saturation Flux Density	T	0.9
Operating Frequency Range	kHz	10-1000
Thermal Conductivity	W/ (cm.° C)	0.02

Table 6.1: Alphaform MF properties [37]

Depending on whether a flux concentrator (fluxtrol Alphaform MF) was to be applied to the coil, the application process was carried out in three different ways. They are as follows:

1. Hand baked coils
2. Mold baked coils
3. Slip-on Molds

Hand baked coils referred to the coils onto which fluxtrol was applied directly on the internal walls of the coils. Fluxtrol was maintained at temperatures below 55° C while applying. This heat treatment is what would give fluxtrol it the clay-like structure helping it to adhere easily onto the coils. Heating them at and above 60° C can potentially start the curing and hardening process of the AlphaForm even before applying it to the coil.

Once the required amount of fluxtrol was applied onto the coil, it was then taped with an aluminum foil paper and PTFE thread seal tape. While the Al foil helped in providing a flat surface for easily forming the fluxtrol, the PTFE tape helped in containing the flow of fluxtrol while it was being cured through a standard process. The curing process involved heating the fluxtrol adhered coil system at 120° C for one hour. After the first stage was complete, the holding temperature was

then increased to 190° C for one hour. This completed the curing process of the fluxtrol, and the coil was then ready to use [37].

Likewise, mold baked coils referred to the coils for which fluxtrol was molded onto Aluminum stems with plastic molds. Once the fluxtrol adhered to the Al stem, the stem was inserted into the coil for the curing process as mentioned above. During the curing process, the fluxtrol would flow evenly onto the internal walls of the coil. After the curing process, the stem would be removed from the coil with the fluxtrol completely hardened onto the coil. Mold baked coils gave more process control over the application and uniformity of fluxtrol applied to the coil thus ensuring uniform heating and repeated results.

On the other hand, the third way of using fluxtrol with the induction coils was to cure the fluxtrol separately on plastic molds and then slip the cured fluxtrol inside the induction coil for use. While the third way of using fluxtrol seemed rather convenient and quick, the flow of current throughout the fluxtrol cone was uneven due to the flux concentrator having multiple discontinuous points with the current conducting coil damaging the fluxtrol insert cone. A schematic showing the three ways adopted for the use of fluxtrol are shown in Fig No.6.3a, b and c respectively.

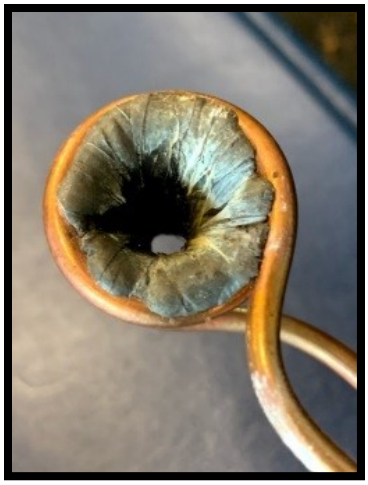

Figure 6.3a: Hand baked coil

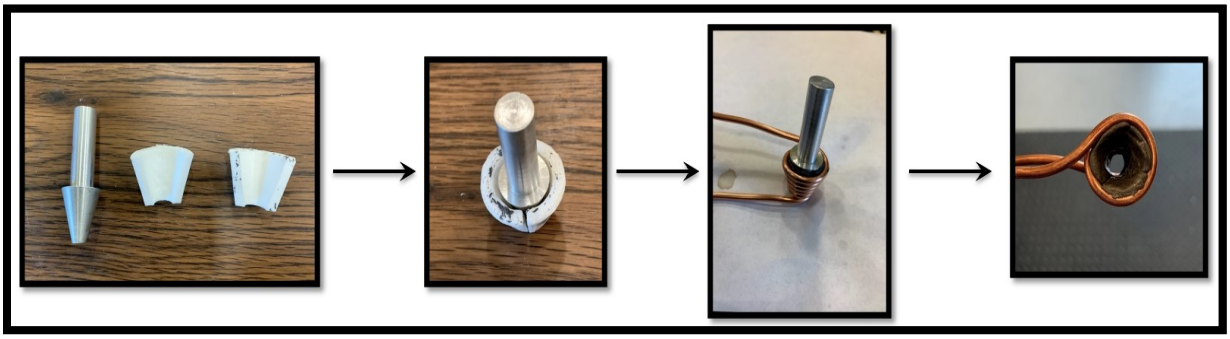

Figure 6.3b: Mold baked coil

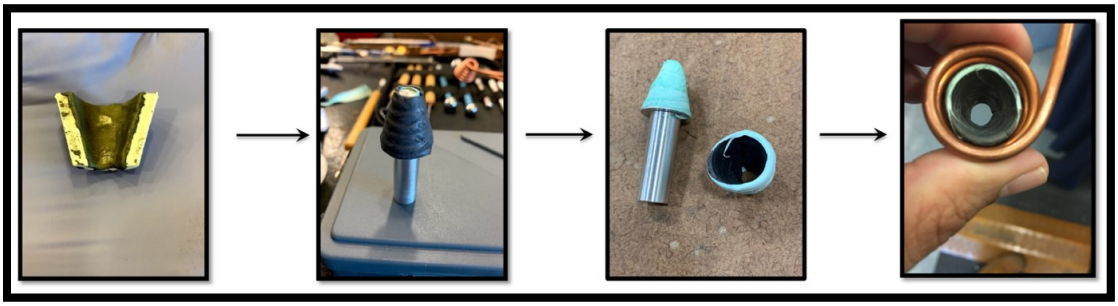

Figure 6.3c: Slip-on mold coil

While the use of flux concentrators with the induction coil really proved as an added advantage in increasing the density of the magnetic flux induced in the baseplate as can be clearly seen in Fig 6.4a., it did have its own set of drawbacks and limitations. The fluxtrol coils generated high intensities of magnetic pull such that the initial induction trials with metal powders would end up with the metal powder being pulled up on the coil due to the magnetic pull even for austenitic powders. It would also lead the current-charged coil to spark with all the metal powder being pulled up in the magnetic field as can be seen during a Laser Power Test from Fig 6.4b. Moreover, since the coil was proposed to be integrated with the laser system, it came with greater risks of damaging the lenses and the optical setup with all the metal powder being pulled up the laser beam path. A small lateral movement of the coil with respect to the nozzle would end up getting the fluxtrol clipped by the laser thus damaging the fluxtrol and its use in the ISLM. Owing to these factors, the use of fluxtrol was limited and more emphasis was given on optimizing the plain conical coil design. This eliminated the extra steps of molding the fluxtrol onto the coil and curing it. Also, it facilitated in the hassle-free assembly of the proposed system design.

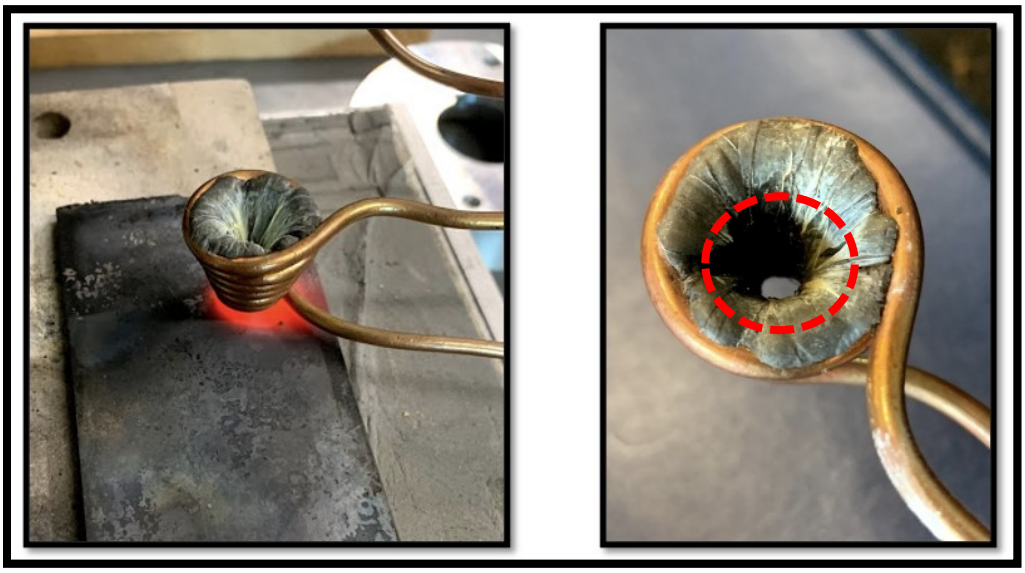

Figure 6.4a: (left) Hand baked coil at 60A of induction current and (right) highlighted area in red damaged due to laser beam clipping on the fluxtrol due to a lateral shift movement of the coil w.r.t the laser

Figure 6.4b: (left) Hand baked coil at 60A of induction current clipping with the laser beam during the power test and (right) plain conical coil with a relatively larger opening bottom diameter allowing uninterrupted passage of the laser beam.

A plain (fluxtrol free) conical intermediate coil was turned using the coil fixture shown in Fig.6.1. The resulting coil was then put to test with Mild Steel and SS 316. Heating times for each of the 5 variants of the coil were recorded to achieve a HAZ as shown in Fig.6.4a (left). The 5 variants of

the same coil were fabricated in accordance with the design revisions of the proposed system and to also validate that the repeatability of the induction heating was consistent. The variants were classified as follows. The first three variants named A, B and C were essentially the same coils turned on the same fixture with the operator error being the only uncertainty. The fourth and the fifth variant named D and E were changed w.r.t the lead of the coils i.e., the length of the coil leads varied and were turned differently to suit the system design discussed in detail later. The variation of these five coils can be seen through a CAD representation in Fig 6.5.

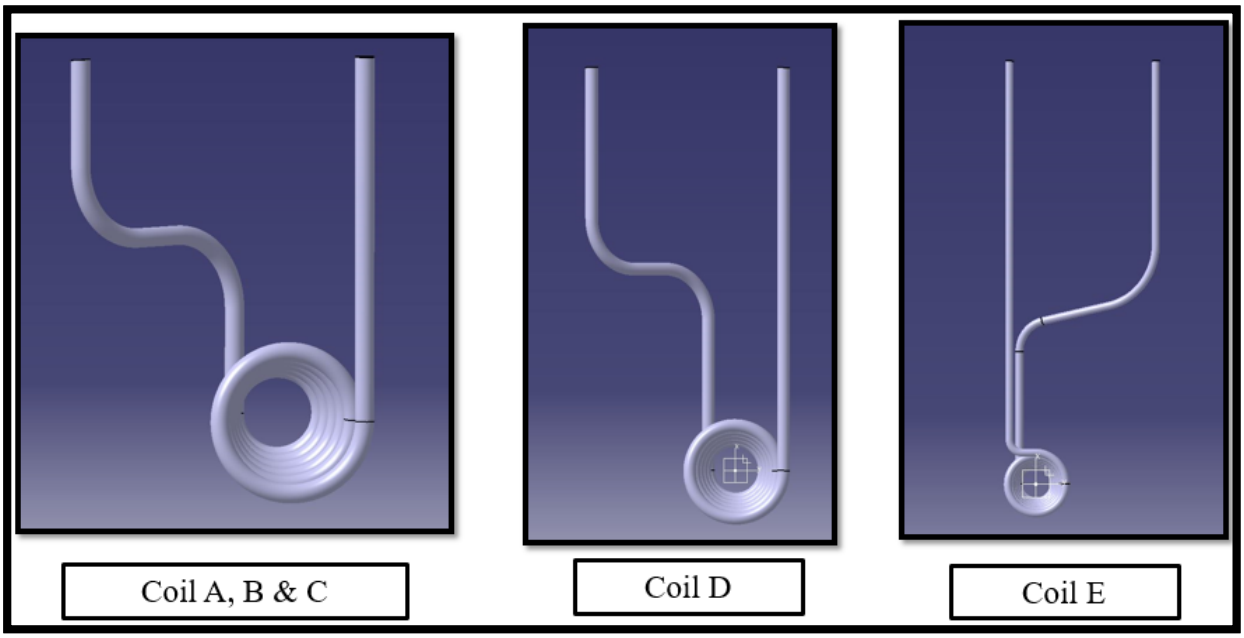

Figure 6.5: CAD representation of the five varians of the intermediate induction coil

Once the coils were turned as per the specifications, they were tested for their heating trials with Mild Steel and SS316. The starting temperatures for both these baseplates were recorded prior to starting each of these heating tests and a constant stand-off height was maintained throughout the set of experiments. A fixed current of 60A was given as an input to the induction coil resulting in

a working frequency of 350kHz. The times were recorded for each of the five variants for the two sets of trials run. Table 6.2 summarizes the results for the heating trials.

Coil Name	Current (A)	Voltage (V)	Frequency (kHz)	Initial Temperature (° C)	Time (s) Mild Steel	Time (s) SS 316
A	60	60	350	23.6	5	35
B		65		27.2	5	19
C		60		28.8	4	37
D		60		26.2	7	32
E		60		24.1	7	29

Table 6.2: Heating Trials of Coils A, B, C, D and E

As can be clearly seen from the test results, Coil B reached the desired coupling temperature (through visual cues as can be seen Fig.6.6) in the shortest time, Coil B was now studied for its design variation as compared to Coils A and C which were turned for same or similar specifications as that of coil B. It was also evident, as expected, that coils D and E take longer coupling times given the increased load distribution due to their varied lengths of the leads (as can be seen in Fig.6.5).

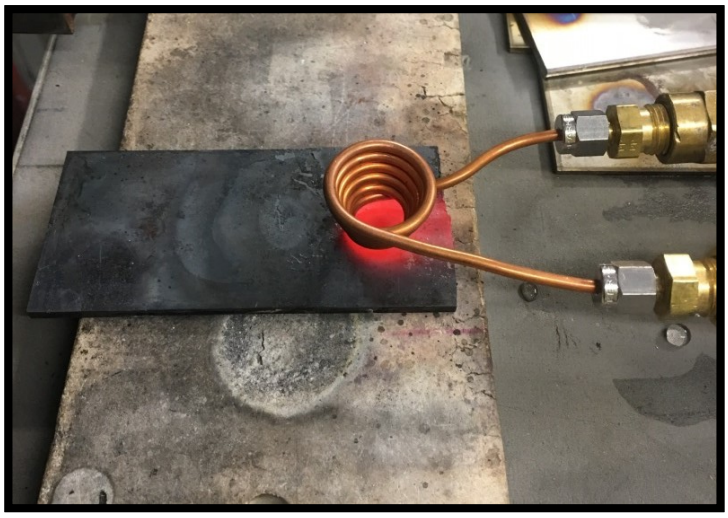

Figure 6.6: Coil B during the preliminary heating heating trial

Further design optimization for coil B included reverse engineering the coil fixture design as per the measured specifications of coil B. Once the design revision was finalized, the coil fixture was printed through FDM (Fused Deposition Modelling), and multiple iterations of the coils were turned and kept ready for their use in the system.

6.2 System Design

The system design for the ISLM process was carried out at various sub-component levels. These sub-components were designed, drafted, machined, and assembled based on the calculations for the optical path of the laser so that its resulting focal length would lie exactly on the powder bed. The first set of sub-components can be listed as follows:

1. Nozzle design and external coil tester
2. Gas inlet manifold design and nozzle holder
3. Nozzle midshaft connector
4. Optic assembly base flange

These sub-components comprised the main ISLM system design w.r.t the induction coil and the laser assembly integration. The second set of components comprised of the Nachi robot system used to make deposits with the ISLM system. The third and the fourth set of components were the Trumpf Laser and the powder bed system integration with the ISLM system. With the incorporation of induction in the system, special attention was paid to the use of metal components around the induction coil and losses due to the coil coupling with the components of the system were assumed to be the reflection in the drop of the coupling of the baseplate to the coil. The nozzle for the induction coil was designed from machinable ceramic. The obvious choice of ceramic was

due to its non-magnetic nature and ability to withstand higher temperatures. The angle of the internal wall of the nozzle was maintained in accordance with the induction coil angle itself. This meant adjusting the angle of flow of the shielding gas outlets designed as a part of the nozzle. For all the components designed for the ISLM system, their respective prototypes were fabricated through 3D printing and mockups were assembled to realize the system assembly and make any revisions, if necessary. As can be clearly seen from Fig 6.4b., lateral movement of the coil w.r.t. the ISLM system could lead to coil failure and other significant component damage, the nozzle design for the induction coil required seamless assembly with tight tolerances to restrict the lateral movement of the coil resulting from the scanning strategy and the robot arm movements followed for the depositions. The progression of the design changes leading to the finished nozzle can be seen in Fig. 6.7.

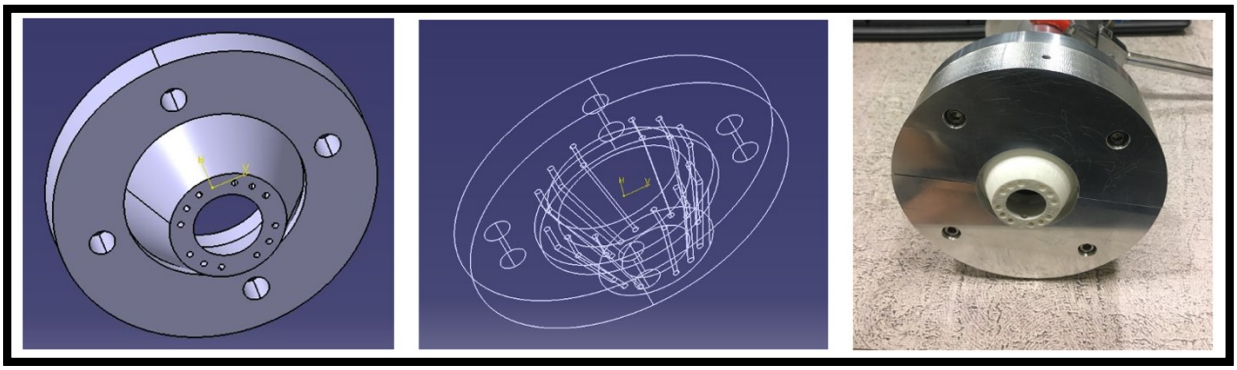

Figure 6.7: Coil B nozzle design progression from CAD to first prototype (from left to right)

Based on the testing of the prototype fabricated for the nozzle, changes as design for manufacturing were adopted and the final design of the nozzle was fabricated. Alongside the nozzle, an external tester was also fabricated to test the induction as a stand-alone addition to the nozzle before assembling the coil into the system. The finished coil and the external coil tester are as shown in Fig 6.8.

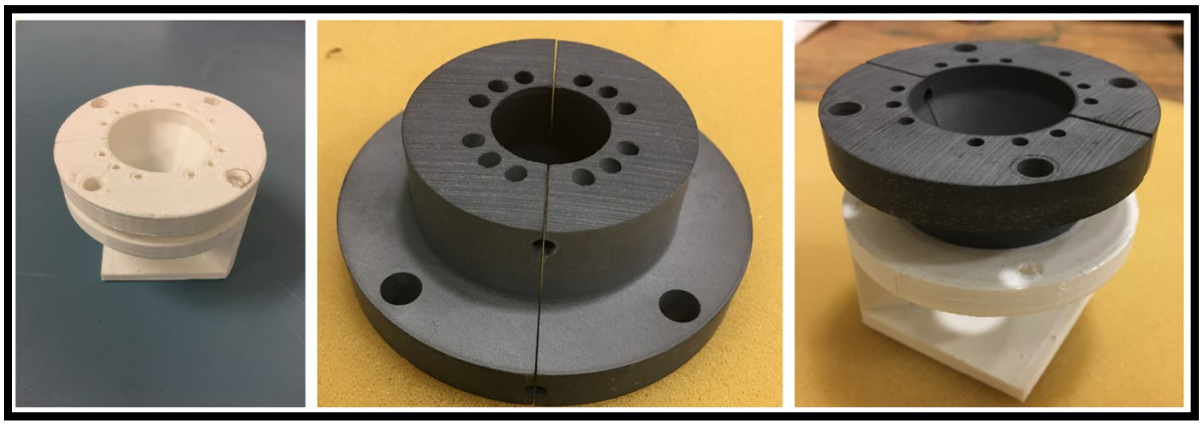

Figure 6.8: Coil B external tester fabricated through FDM on the left. Ceramic coil nozzle at the centre and nozzle and external coil tester and nozzle assembly at the right

The gas inlet manifold design, nozzle holder, nozzle midshaft connector and the optic assembly base flange were designed as a sub-assembly. Multiple iterations to accommodate provisions for various mounting and positioning features were designed onto this sub-assembly. The progression of the iterations of this sub-assembly can be seen in Fig 6.9. The Zemax calculations for a laser beam spot size of 2.77mm resulted in a 6.661in length for convergence of the beam from the end of the optics on the robot arm. Taking into consideration the stand-off height between the coil and the powder layer, coil integration into the setup design, the design height of 6.661 in was then split into 6.411 + 0.125 + 0.125in. The final designed height of the setup being 6.411 in, 0.125in for the copper coil tubing (last turn of the coil) protruding outside the nozzle and the second 0.125 in would be the maximum stand-off available between the coil and the powder layer. The total overall height for this sub-assembly was then always maintained at 6.41 inches.

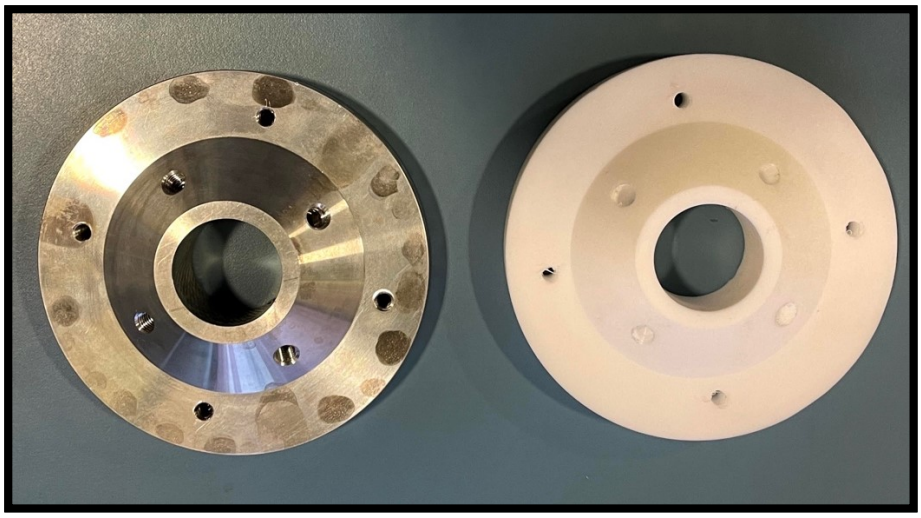

Figure 6.9a: The gas inlet manifold actual machined part (left) and Prototype (right)

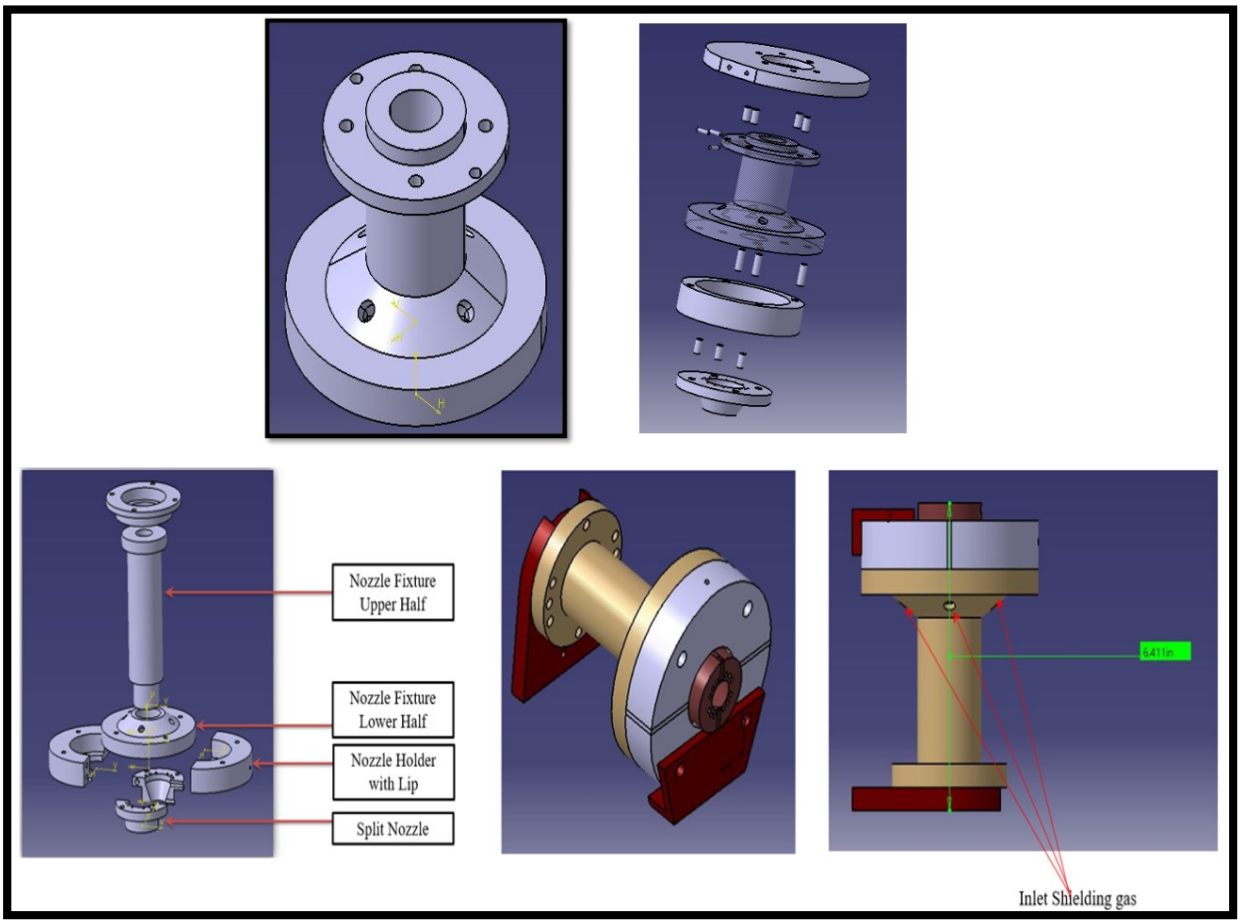

Figure 6.9b: The gas inlet manifold, nozzle holder, nozzle midshaft connector and the optic assembly base flange sub-asembly progression from top to bottom.

The resulting ISLM setup was then integrated with the optics setup and assembled on the robot arm. The optics setup was adapted from the LACS (Laser assisted Cold Spray) system and Fig 6.10 shows a schematic of the optic setup.

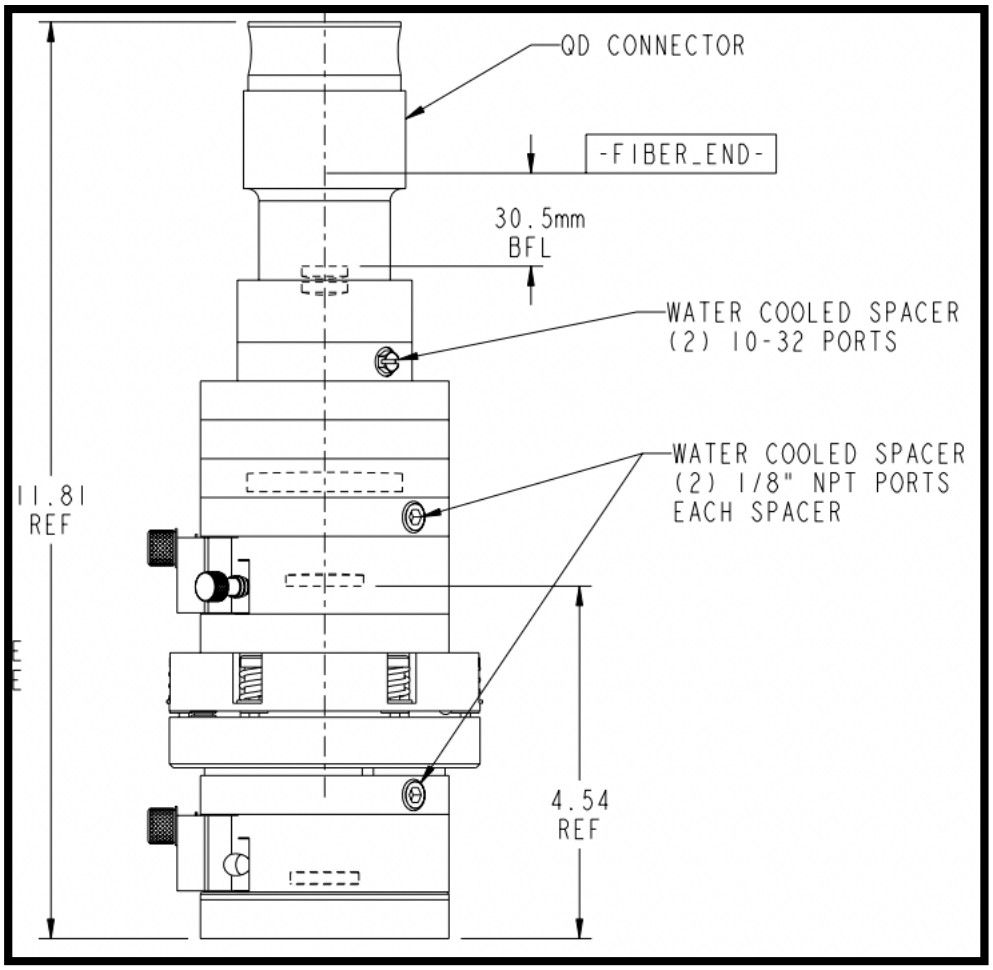

Figure 6.10: ISLM Optic setup

The entire ISLM system assembly mounted on the robot arm for the Nachi SH 200 AX-10. The Nachi robot was used to generate the scanning patterns for the deposits made through the ISLM system. It's simple program coding language made making changes to the program a simpler task and gave the flexibility of controlling the minute details of the scanning patterns such as modifying the overlap percentage in the different raster scans that were programmed for the deposits. This

helped in eliminating any uncertainties arising through the fixed process parameters and provided more emphasis on the system optimization for material deposition.

The entire assembly mounted on the robot arm was modelled on CAD followed by a successful physical assembly.

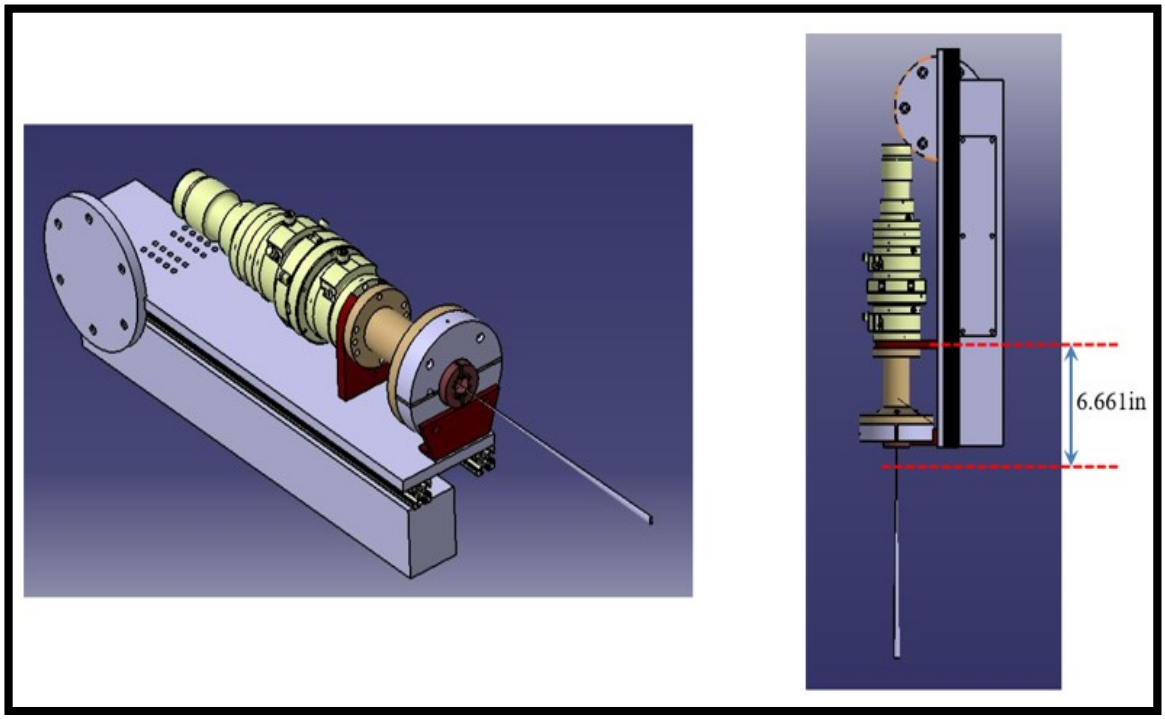

Figure 6.11: CAD assembly of the ISLM System setup on robot arm with simulated laser beam travel

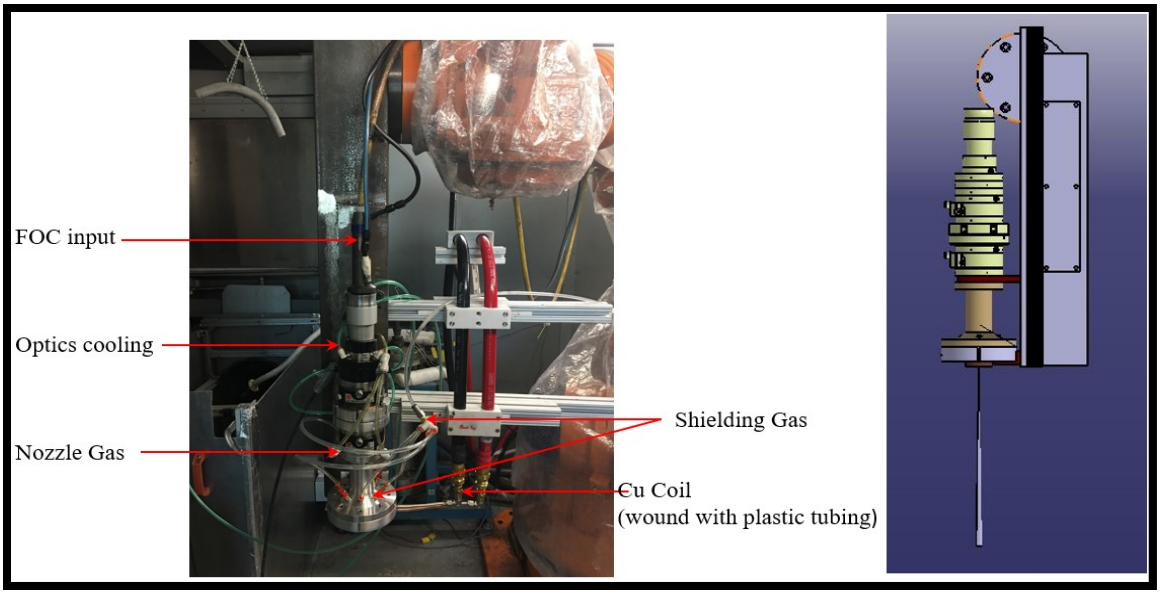

Figure 6.12: ISLM System setup on robot arm with mounted induction power supply

The next sub-component assembly was the powder bed that would be used for the depositions. Benchmarked with a typical powder bed design, the ISLM powder bed consisted of three sections of equal dimensions. These were namely: (1) Powder Reservoir, (2) Building Chamber and (3) Powder dump.

The powder reservoir, as the name suggests, is used to store the powder which would be spread onto the building chamber in a layer-by-layer manner with the help of a powder blade. The building chamber is the section where the deposits are fabricated with the ISLM system, and the powder dump is the section where the extra powder from the powder spread gets collected when the blade spreads the powder on the building chamber. The powder blade is controlled by a dual stepper motor setup on either side of the blade mount. This dual motor setup helps in accurately spreading the powder by eliminating jerks in the movement of the blade. The blade mount houses a bevel gear and a rotary gear setup on each ends respectively. The bevel gear drives the roller mounted

on the rear end of the powder blade as a means to flatten the newly spread powder layer in the building chamber. On the other hand, the rotary gear is coupled to a gear rack mounted on the powder bed which provides the necessary linear motion for the powder blade and the blade mount. The powder reservoir and the build chamber comprise of pistons that have opposite motion w.r.t each other and are responsible for making new powder layer available for spreading and creating an equivalent powder layer depth for the new layer to be spread on their respective sections. The pistons are operated through stepper motors allowing for precise motion defining the overall height of every layer.

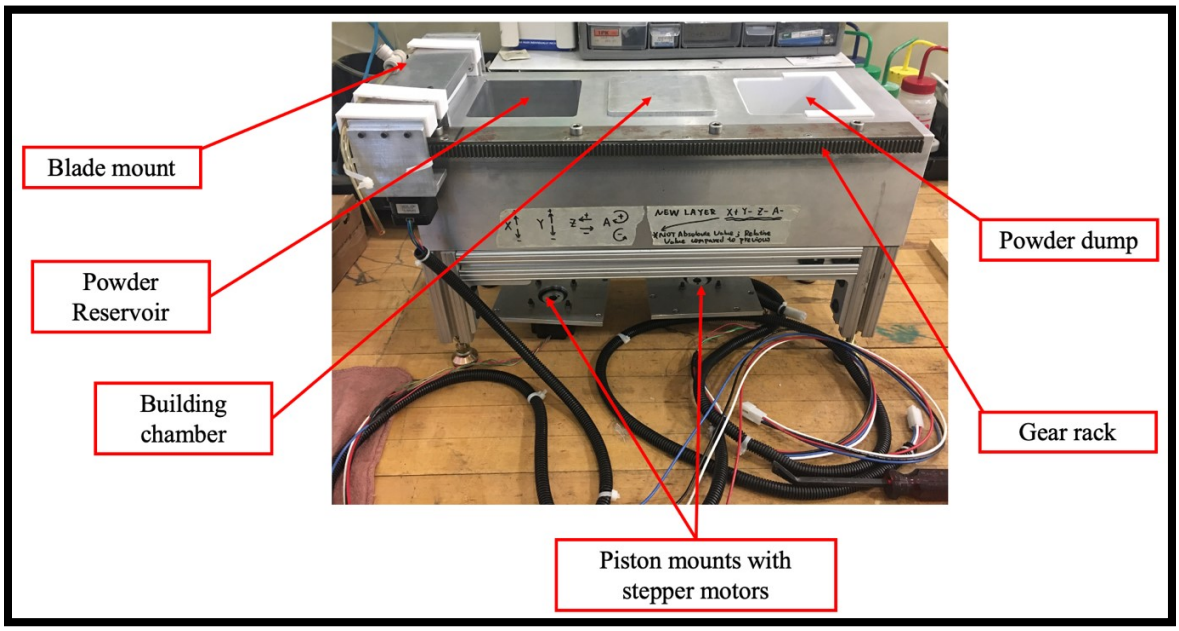

Figure 6.13: ISLM System powder bed

A Trumpf TruDisk 3302 laser was used for the ISLM system. The output wavelength of the laser light from the TruDisk 3302 is 1030nm with a minimum power output of 80W and a maximum power output of 3000W. The Fiber Optic Cable (FOC) travels all the way from the main unit of the TruDisk to the ISLM optic system to finally generate a laser beam with a diameter of 2.77mm.

The TruControl panel assists in operating the various functions of the laser from conducting preventive to corrective maintenance to regulating the type and power of the laser program in use. For the purpose of the ISLM depositions, the continuous wave mode of the laser was used. The working laser power range for the ISLM deposits was from 80W to 150W.

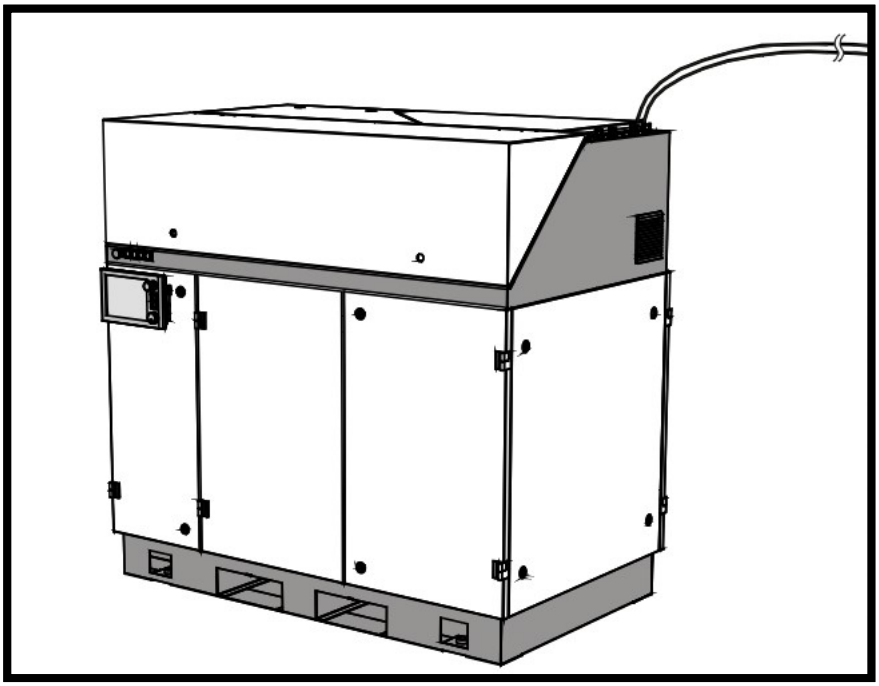

Figure 6.14: Trumpf TruDisk 3302 main unit schematic with a FOC [38]

All the sub-component assembles were integrated together in CAD to realize the system layout and the physical ISLM was assembled. While major components of the final system were standard industrial equipment either designated for different research applications or for other product development processes at the Additive Manufacturing Processes Labs (AMPL), components specifically designed for ISLM were designed to machine through conventional manufacturing processes.

The stepper motors for the powder bed (total of 4) were controlled through an in-house built PLC circuit operated through MACH3 programming software. The MACH3 program codes mainly varied with the powder feed rate through the powder blade (dual stepper motor setup), layer thickness (Y- axis motion for the pistons in the powder reservoir and the building chamber) and the no. of layers the program and the experiment was designed for.

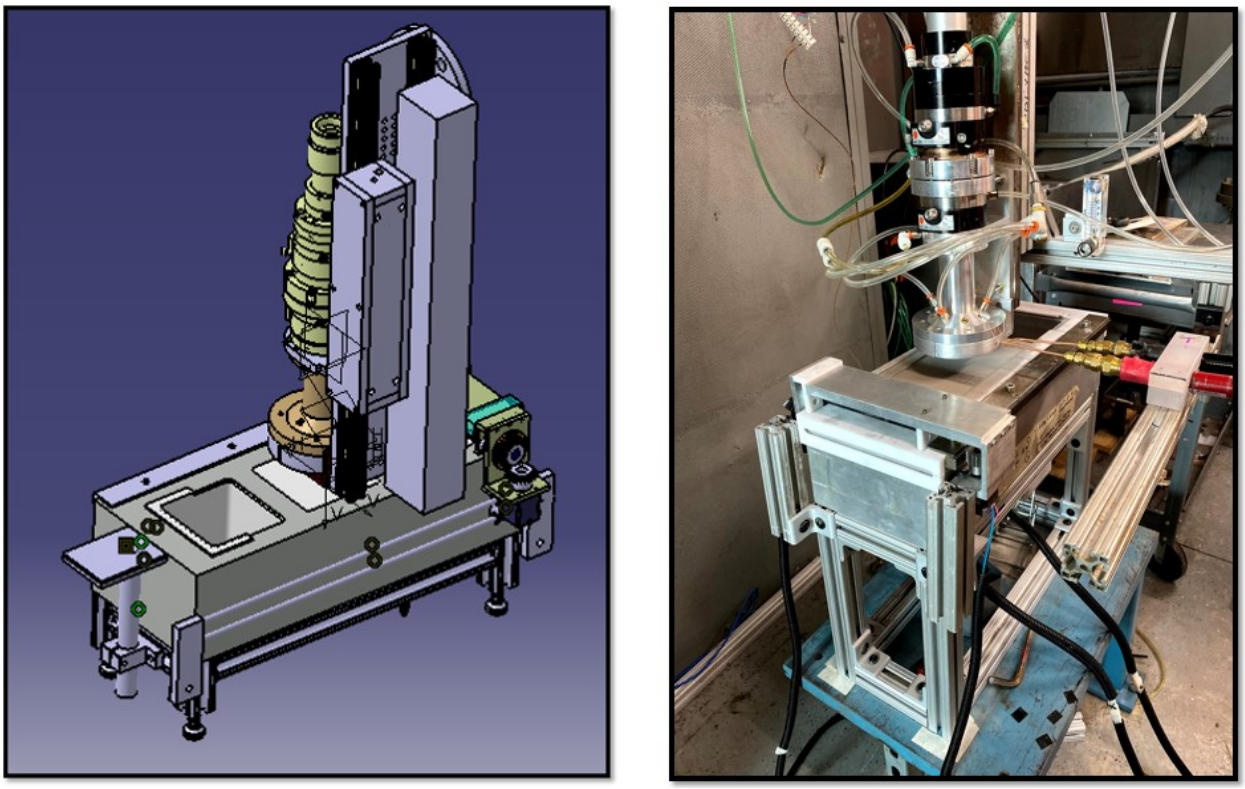

Figure 6.15: CAD ISLM assembly (left) and physical ISLM assembly (right)

Pillar MK-20 Induction system was used as the power supply source for the designed induction coil. It is a water-cooled solid state frequency convertor which makes use of a 3-phase voltage source to produce a single-phase output at one of the four nominal frequencies at 50, 100, 200, 300 or 400kHz. The MK-20 comes with a resonant frequency generator designed to operate at the resonant frequency of the tank circuit. A function of tank capacitance and inductance (ISLM coil),

the easiest approach to change the resonant frequency is by adjusting the tank capacitance as the inductance is fixed for the given application. The capacitance adjustment process is as shown in Fig No.6.16. The output leads from the MK-20 are connected to the ISLM coil and current is input parameter on the system. The resulting load adjusts the output voltage and the frequency. Owing to this working principle, the data generated for the design simulation of the ISLM coil has been under the assumption of a fixed frequency and voltage with current only being the deciding variable for the coil [39].

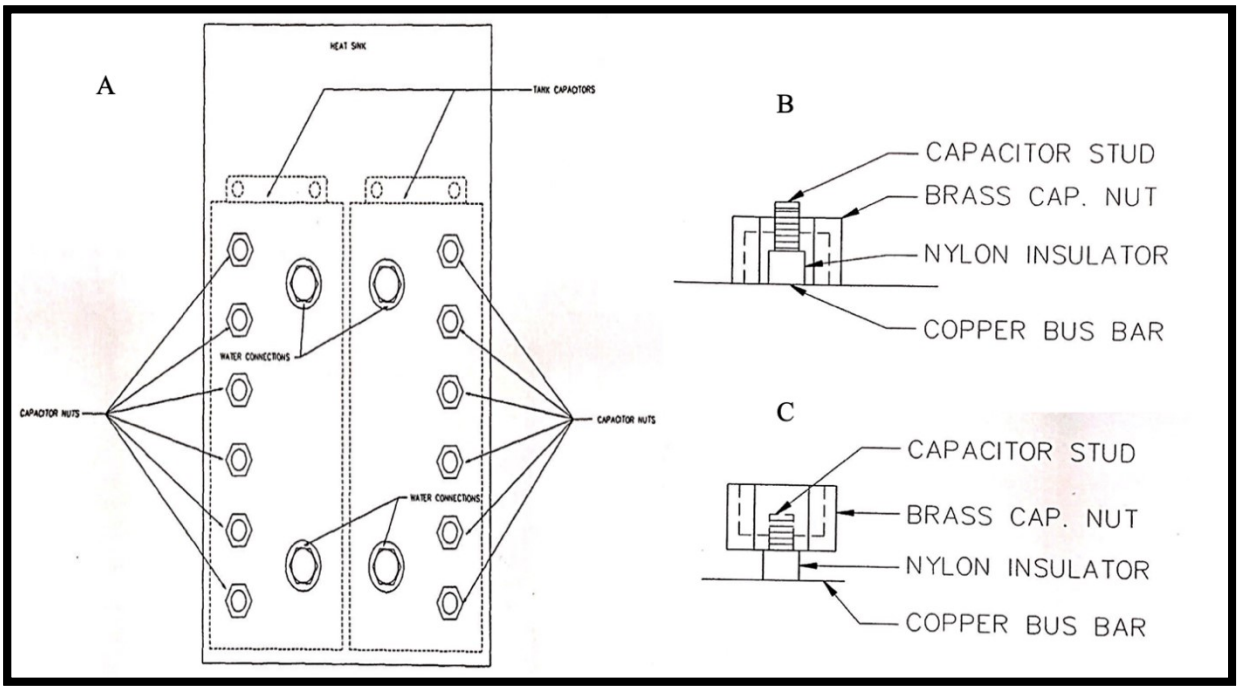

Figure 6.16: (A) Front view of the tank section, (B) Capacitor in tank circuit and (C) Capacitor removed from tank circuit

As both the units (Trumpf TruDisk and MK-20) are water-cooled, Riedel chillers are used for their respective operations. With a maximum current output of 72A of DC current, the MK-20 comes fitted with a teach pendant that helps controlling the basic system parameters from an isolated location (in this case, outside of an enclosed booth structure) [39].

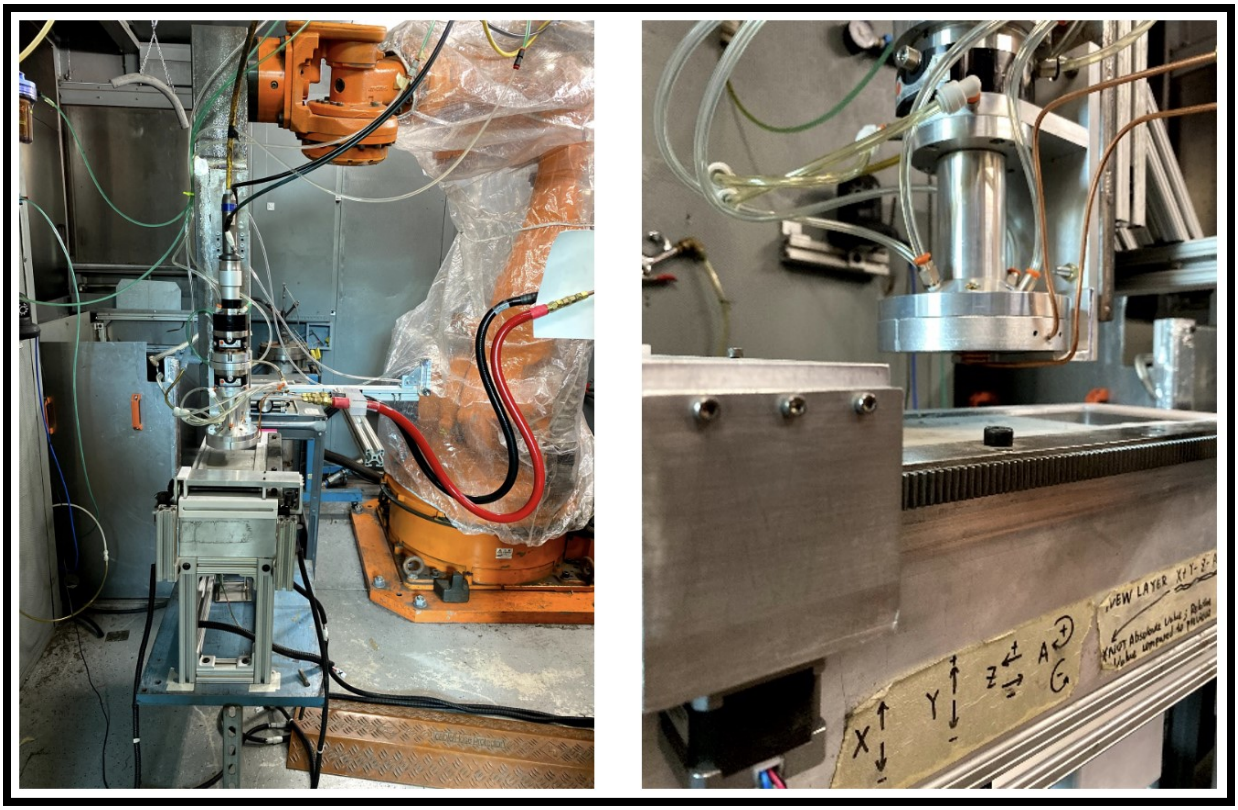

Figure 6.17: ISLM system (left) and ISLM system closeup with the powder bed

Chapter 7. ISLM Depositions and Experiments

7.1 System Testing

Once the ISLM system was assembled, a detailed Job Safety Analysis (JSA) was conducted to set working protocols and formulate a Standard Operating Procedure (SOP) for the ISLM system. Part of the SOP included the laser power tests, compatibility checks by conducting alignment tests, coil tests, Nachi Robot tests and the powder bed program tests.

7.1.1 Beam Alignment Test

The correct optical alignment of the assembly directly regulates the quality of the output. Due to this, the beam alignment test was the first test in the standard operating procedure for the ISLM and was necessary prior to conducting any experimental deposits. A beam alignment test necessarily needs to be carried out (1) after making modifications in the optical setup, (b) modifying the laser program and its mode of operation, (c) changing the ISLM coil from the setup, (d) making any design revisions directly affecting the laser beam path and (e) after powering up the system after maintenance downtime. This made sure that the laser would not clip on the coil while the process is running leading to potential hazards. The TruDisk 3302 has a provision for the Pilot Light path HeNe (Helium-Neon) beam to check for any alignment issue the system may have. This was done by turning on the HeNe and measuring the beam size to measure the

differences of the beam profile geometry by conducting burn tests, if any. Another technique to check the alignment of the optics is through visual inspection and mapping the pilot light on a crosshair to understand the deviation of the light path from its actual expected profile and measurements. A good representation of this can be seen in Fig no.7.1. The HeNe was also proved helpful while recording program points on the NACHI robot to make sure that the robot travels on the desired toolpath and does not deviate onto other areas of the building chamber. More on this process has been discussed in later sections of this chapter.

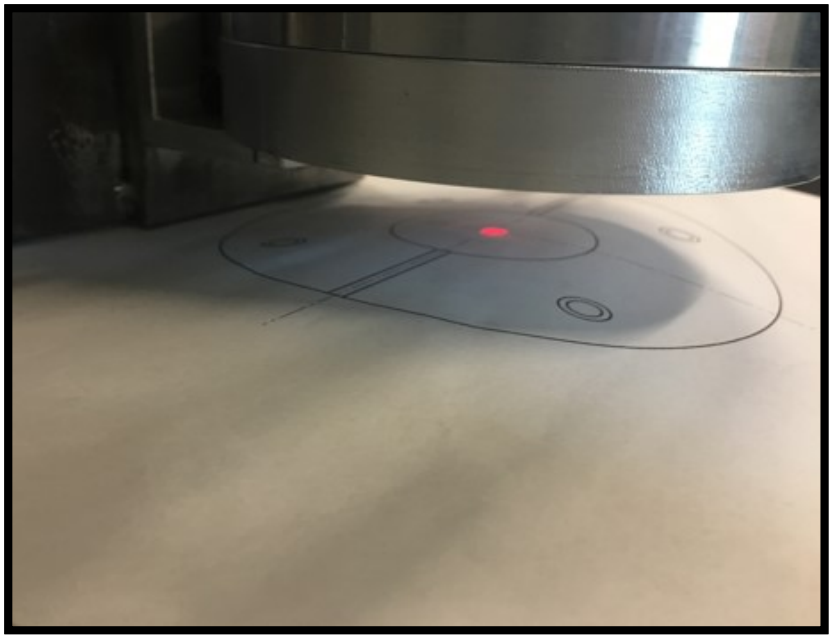

Figure 7.1: ISLM system beam alignment test

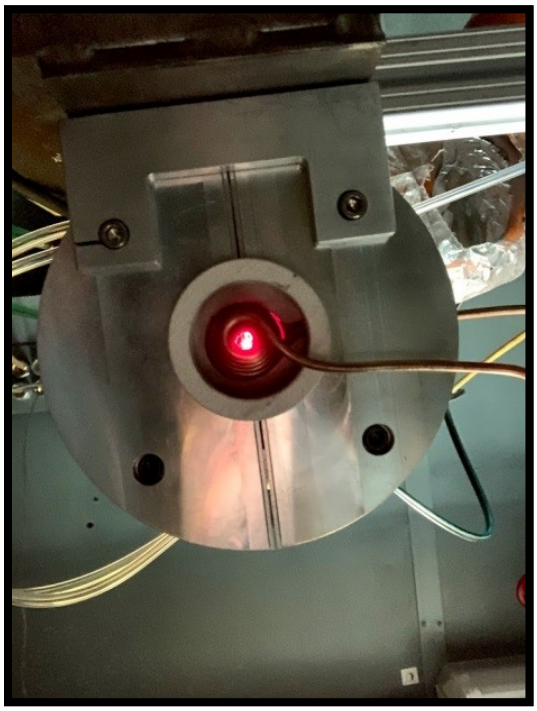

Figure 7.2: HeNe beam path bottom view from the ISLM system

7.1.2 Laser Power Test

One of the defining parameters of the L-PBF process is the Laser. A measured output of the laser helps in building a well-informed approach towards the design of experiments. It also helps in determining the significant effects the parameter can have on the final output of the process. Typically, a laser power test is also carried out for the very same reasons as that for the Alignment Test. It gives the accounted losses of laser power and also helps in determining if any changes are required towards addressing this concern. A laser power test is conducted by defocusing the laser beam. This can be achieved by moving the setup positive Z axis so that the focal point of the beam path is pushed further away from the tip of the lens. The primary reason to defocus is to protect the pyrometer used in measuring the output laser power from the intensity of the laser beam for an

extended period of time while the test is being conducted. This pyrometer is water-cooled and is connected to a digital output which reads the measured values over the time of the test.

The ISLM laser power test is carried out for a duration of 1.5mins for each input value of laser power. Any losses below 10% of the input value is acceptable taking into consideration that there are transmission losses, setup losses, etc. The power test was carried out over a laser power range of 100W to 400W in incremental steps of 50W.

Laser Power Input (W)	**Measured Laser Power (W)**	**Difference (W)**	**Percentage Loss (%)**
100	93	7	7.00
150	143	7	4.67
200	193	7	3.50
250	241	9	3.60
300	290	10	3.33
350	342	8	2.29
400	390	10	2.50

Table 7.1: Laser Power Test results for the ISLM system

As can be observed from the results in Table 7.1, the highest power loss measured was 7%. The setup for the power test can be seen in Fig 7.3.

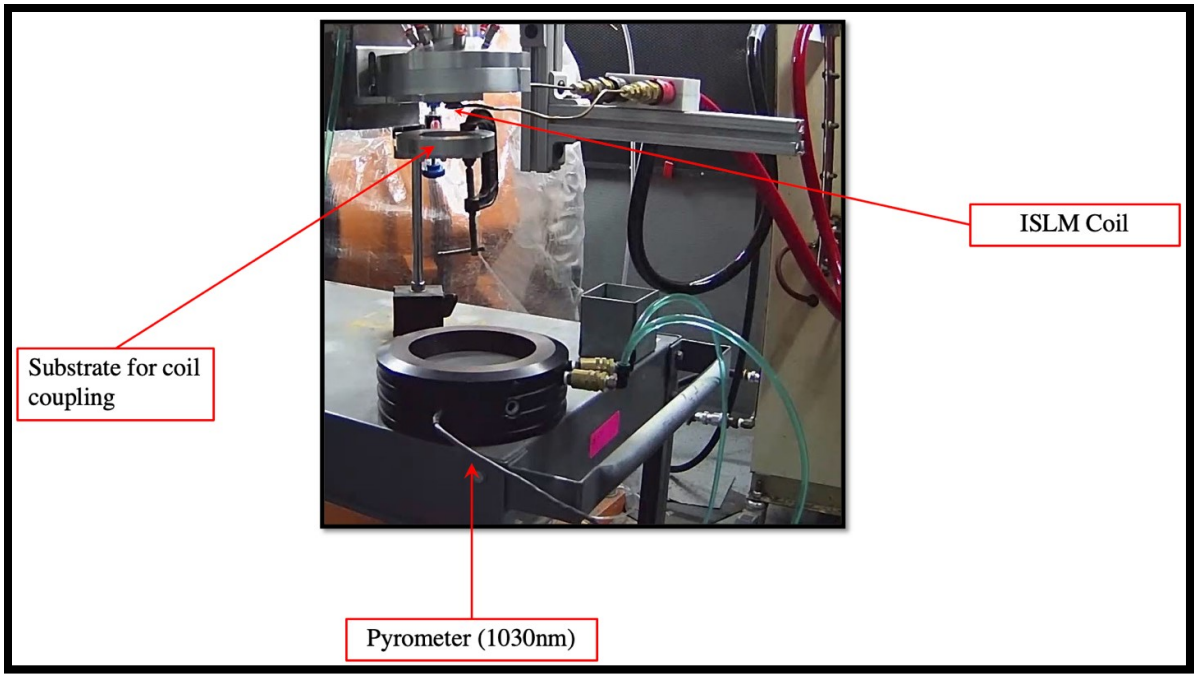

Figure 7.3: Laser Power Test setup

7.1.3 ISLM Coil Test

The working principle of induction is such that the inductor under the presence of a current flow generates a magnetic field and induces eddy currents in the workpiece or any good conductor of electricity in the vicinity of the inductor. This can lead to significant losses in the coupling efficiency through drop in desired temperature rise required in the workpiece (baseplate) as the metals surrounding the coil and/or the workpiece is also under the magnetic field influence. As a result of this, conducting coil tests like the one described in Table 6.2 becomes necessary. The only difference between the two tests is the environment in which the test is conducted. The presence of the ISLM system metal components around the ISLM coil mandates measuring temperatures on the components as well as the baseplate.

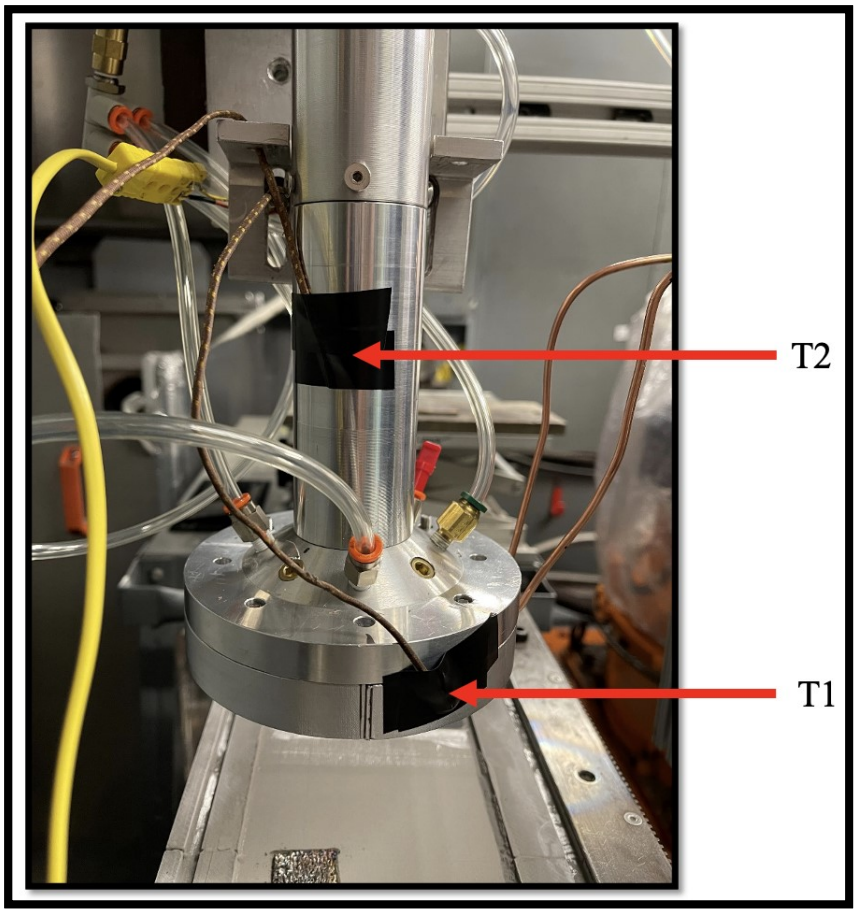

Figure 7.4: ISLM Coil Test setup- first stage

The coupling test measurements were divided in two stages. In the first stage, temperature rise was measured with the ISLM system depositing one complete one-layer build (one complete raster pass) at two points. The first point T1 was the nozzle holder which lies in the immediate vicinity of the coil and T2 which was on the nozzle midshaft connector. A temperature rise of 85 ºC was measured at T1 and 37 ºC at T2 when the ISLM system was used to deposit. On the other hand, when the induction system was turned off and just the laser was used to deposit a one-layer build, a temperature rise of 27 ºC was measured at points T1 and T2. It was clear from the tests when the ISLM system was put to use, there was a loss of coupling to the system components which resulted

in the rise of temperature neglecting the radiation effect from the melt pool and the process as a whole.

The second stage of the coupling test measurement was to check the coupling time to match the visual cue as observed in Table 6.2. For an induction current of 60A, stand-off of 0.125in, the time required by the coil to reach a desired temperature to match the visual template used as used and shown in Fig 6.6. Unlike the first stage testing, the coil was kept stationary, and the baseplate was now located on the powder bed's building chamber.

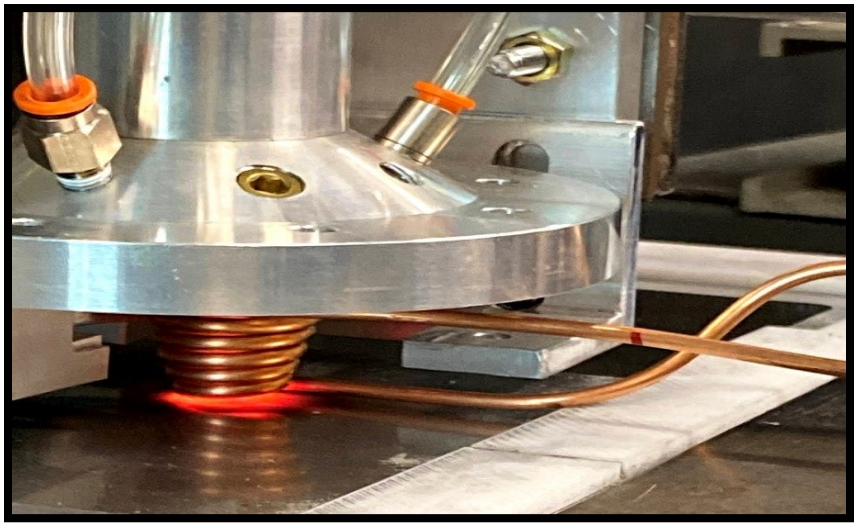

Figure 7.5: ISLM Coil Test setup- second stage

The desired temperature rise was now obtained at a measured time duration of 20 seconds. This also validated the observations made in the first stage of the coupling test with losses incurred from undesirable coupling of the ISLM coil with the surrounding system components.

7.1.4 Nachi and MACH3 Controls

The Nachi SH-200 AX 10 robot was used to program the scanning strategy for the depositions. The programming syntax for the robot follows the positioning methodology in which each position on the desired toolpath defining the motion needs to be recorded. For example, for a simple line program, the Nachi robot would take in an input of two points. The mode of travel between these two points will then need to be defined as either Linear, Angular or Circular. Likewise, for a raster scanning strategy, an overlap distance (also known as hatching distance) typically acceptable in the range of 50% of the single-track width and above, a program was coded for two different scan patterns. These programs were called the “perpendicular” and “parallel” orientation programs. The names for the programs were based on the orientation of the coil leads w.r.t the longest length of the raster pass. This can be well understood through a visual representation as shown in Fig 7.6. The scan speed was defined as the travel speed for the raster program and was varied from 2mm/s to 8mm/s in incremental steps of 2mm/s. The HeNe pilot light from the Trumpf laser was used to correctly trace the toolpath of the deposit while the Nachi programs were written. Throughout the program, the vertical motion of the robot arm is fixed. This vertical position of the robot arm is calculated based on the required stand-off distance between the last turn of the coil and the topmost layer of the powder bed. The overall program is then divided into two-time steps: deposit time and dwell time. For an overall deposit dimension of 1” x 1” and a fixed time steps required for spread the powder layer (dwell time), the deposit time varied from 6.9 mins/layer at a scan speed of 2mm/s to 2.88 mins/layer at 6mm/s.

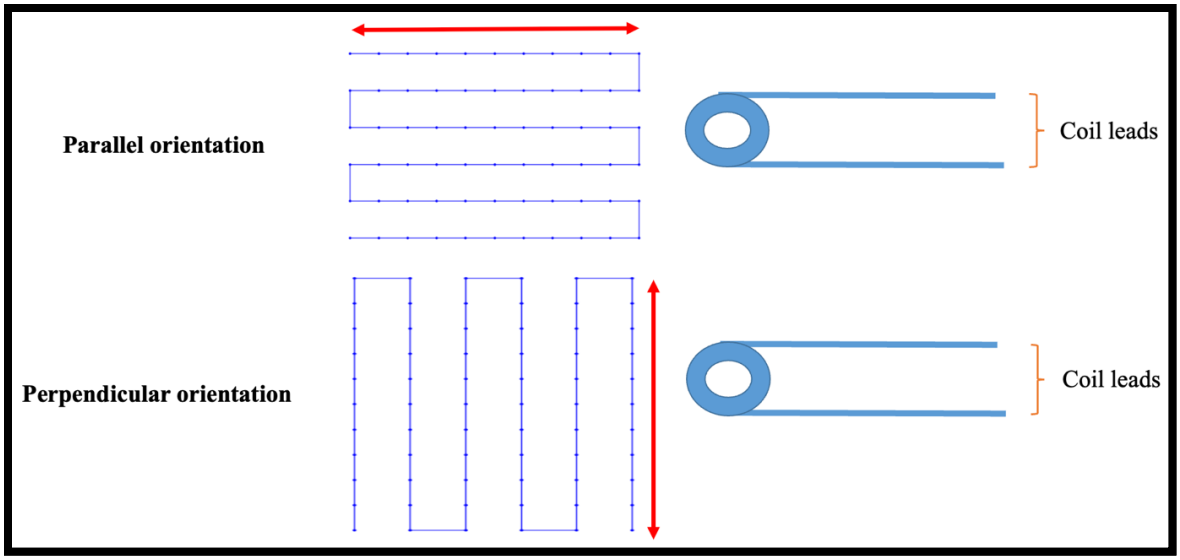

Figure 7.6: Top view of scanning patterns w.r.t coil leads

The MACH3 controls program would help in operating the stepper motor co-ordination on the powder bed. The MACH3 programming syntax is based on the G and M code inputs. The Y axis motion, upwards for the powder reservoir and downwards for the building chamber, needed same increments that would define the layer thickness of the deposit. The bevel gear feed rate and the rotary gear feed rate were adjusted according to the step size of the motors and the program requirement of the deposit to achieve shorter "dwell times" for each deposit. Similar to the programming on the Nachi robot, the MACH3 program was also coded for multi-layer deposits. Various iterations of the MACH3 program code were tested to achieve the ideal parameters for the powder bed and the powder layer spreading. This was majorly regulated by the machining tolerances achieved on the powder bed components namely the pistons, the baseplate, and the roller blade.

The integrated co-ordination of these mentioned sub-systems (Induction, Laser, Robot and the MACH3) would ensure a good deposit experiment for the ISLM system. Multiple iterations of

these coordinated runs were carried out to finally formulate a Standard Operating Procedure for the ISLM. Based on the SOP and the individual specifications of these systems along with the designed ISLM coil, two sets of experiments were designed to be carried out with the system. The first set was conducting single layer deposits and the second set consisted of running multi-layer deposits. Approaches for both the experimental sets are discussed in the sections hereon.

7.2 ISLM Experiments

With a maximum induction current set at 60A and the ISLM system checks done, a simple design of experiments was carried out. The entire experimental procedure was divided into two stages. The first stage consisted of depositing single layer deposits and the second stage consisted of multi-layer depositions. The single layer depositions formed the basis of the parameter optimization for the multi-layer deposits. The characterization of these single layer deposits held two important significances. The first, as discussed, was the parameter optimization for the second stage of experiments while the second significance was the data generation for the Digital Twin. The Digital Twin and its approach are discussed in the next chapter. However, the very basis of the Digital Twin is data driven. As a result of this, a comprehensive dataset was required to build an algorithm that would help in formulating a Digital Twin. In addition to this, the single layer experiment characterization also helped in highlighting the differences and key improvements the proposed concept has over a standard Selective Laser Melting (SLM) process. As a result of this, depositions laser counterparts for every ISLM deposit became important to complete the study. The multi-layer deposits and their characterization would give an in-depth analysis of the ISLM system and the advantages it possesses over the standard SLM.

Sample No	Coil Type	Induction Current (A)	Laser Power (W)	Scan speed (mm/s)	Scan Strategy
M1		60	80	2	Perpendicular
M1.1		0	80	2	Perpendicular
M2		60	80	4	Perpendicular
M2.1		0	80	4	Perpendicular
M3		60	80	6	Perpendicular
M3.1		0	80	6	Perpendicular
M4		60	100	2	Perpendicular
M4.1		0	100	2	Perpendicular
M5		60	100	4	Perpendicular
M5.1		0	100	4	Perpendicular
M6		60	100	6	Perpendicular
M6.1		0	100	6	Perpendicular
M7.1		0	100	8	Perpendicular
M8		60	80	2	Parallel
M8.1		0	80	2	Parallel
M9		60	100	2	Parallel
M9.1	B	0	100	2	Parallel
M10		60	80	4	Parallel
M10.1		0	80	4	Parallel
M11		60	100	4	Parallel
M11.1		0	100	4	Parallel
M12		60	80	6	Parallel
M12.1		0	80	6	Parallel
M13		60	100	6	Parallel
M13.1		0	100	6	Parallel
M14		60	80	8	Parallel
M14.1		0	80	8	Parallel
M15		60	100	8	Parallel
M15.1		0	100	8	Parallel
M16		60	120	6	Parallel
M16.1		0	120	6	Parallel
M17		60	150	6	Parallel
M17.1		0	150	6	Parallel

Table 7.2: ISLM single layer deposit list of experiments

The nomenclature developed for all the samples mentioned in Table 7.2 is as follows. All the deposits start with **M**. The ISLM deposit would follow the nomenclature **M** (sample number). On the other hand, the laser counterpart deposit would follow the nomenclature as **M** (sample number)**.1**. For example, M1 would be an ISLM deposit and M1.1 would be the same set of parameters except that it would be deposited using just the laser without any induction influence. 33 single layer deposits were made through ISLM, and Laser-only samples combined and were

characterized for different evaluations as follows. Both, the single layer and multi-layer deposits followed standard metallographic preparations by grinding up from a 240 to 1200 grit size SiC papers. Colloidal alumina and silica slurry polish were used for the multi-layer deposits after the grinding process.

7.2.1 Phase Identification

To study the phase alterations or modifications of the samples deposited with ISLM, an X-ray Diffraction (XRD) analysis was conducted on the samples using the Rigaku Miniflex, Cu Kα radiation with ƛ = 1.5402 Å. Fig 7.7 shows compiled diffraction graphs, and the phases present in the ISLM samples, the laser counterparts and the as-is Truform SS 3163 powder received from Praxair. The Truform 3163 powder was a Fe-17Cr-12Ni-3Mo chemistry composition with a D50 of 31µm [40]. The peaks for all the compilations were indexed using the ICDD 2019 Database. The presence of a residual ferrite was observed in the as-received 3163 powder. The presence of the austenite-only peaks at 43.8º, 50.9º and 74.8º in both the ISLM and the laser only samples was confirmed through their indexing and also aligns well with the results reported for SS316 fabricated through the L-PBF process [41] [42] [43]. Peak broadening was observed and can be concluded as an outcome of the fabrication process (SLM) due to the introduction of the residual stresses due to the rapid solidification phenomena occurring the additively manufactured deposits and also indicated the possibility of formation of fine grain structures [44] [45] [46] [47]. However, the most important conclusion from the study was there was no phase change due to the introduction of an extra heating source (induction coil).

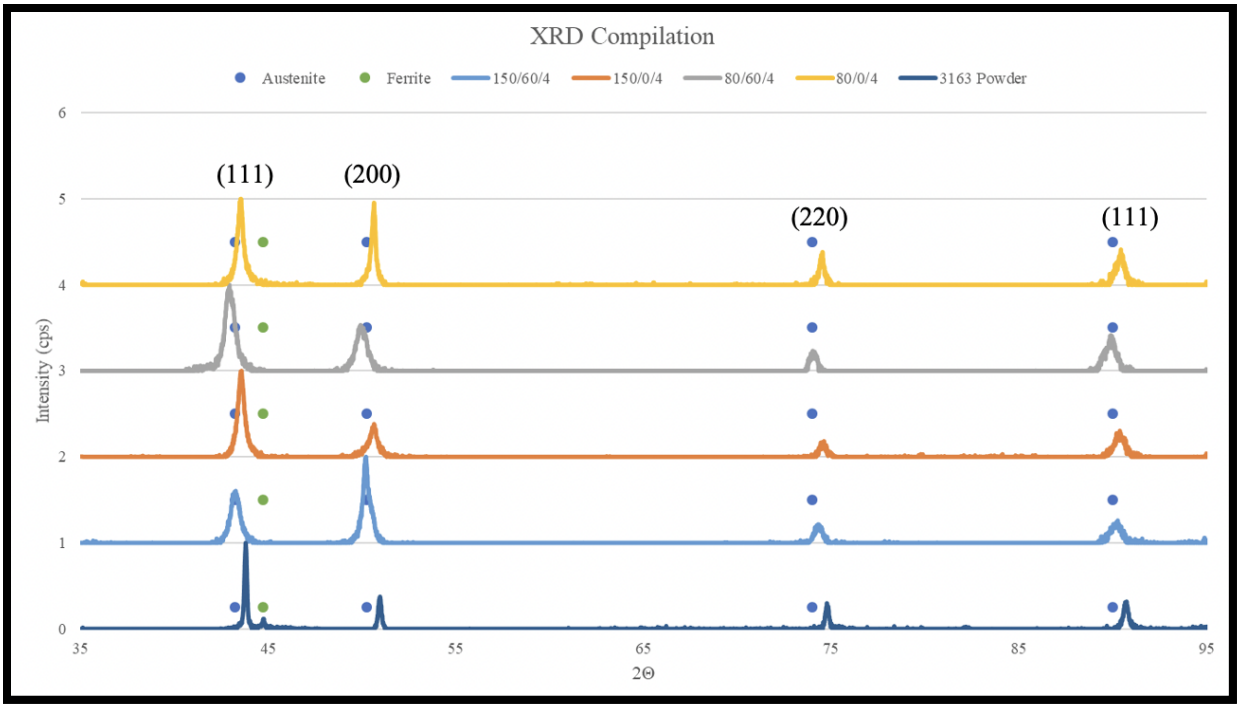

Figure 7.7: XRD Pattern compilation for ISLM samples, laser only samples and as-received powder

A minor phase shift of ~ 0.2º was observed for a few compositions across the compilation. This was possibly due to the non-equilibrium nature of the process or the errors in the instruments or both. XRD patterns allow for the selective spacing of the specific set of crystal lattice planes (h k l) oriented at precise angles to the surface of the deposit with the accuracy required to determine the strain the surface of the deposit. The angle ψ between the normal of the surface of the deposit and the incident and diffracted beam bisector also refers to the angle between the normal to the diffracting lattice planes and the sample surface. The presence of a tensile stress results in the contraction of the Poisson's ratio which reduces the lattice spacing and increases the diffraction angle of the crystal. Rotation of the deposit through some known angle ψ further causes the tensile stress present in the deposit to increase the lattice spacing. Measurements of the angular change of the diffraction peaks for a minimum of two orientations of the deposit surface enables stress

calculations present in the surface of the deposit. As only elastic strains change the mean lattice spacing, only elastic strains are measurable through XRD patterns, useful to determine the macro-stresses discussed in the previous chapters.

The residual stresses measured through XRD are the arithmetic average of the stresses related to a volume of the material defined by the irradiated area. The depth of penetration is governed by the linear absorption co-efficient for the deposit material and the radiation. Plane stresses exist in this thin layer of the diffracting surface with no normal or shear stresses acting on the surface. As a result of this, stresses can be measured without any reference to any unstressed lattice spacing standard [48].

7.2.2 Single Layer SEM Cross-section Analysis

Standard metallographic procedures were followed to prepare the samples for characterization and analysis. A Hitachi S-2600N SEM to determine and inspect the quality in terms of homogeneity, induced porosity, and cracks through SEM/ BSE micrographs across a defined magnification.

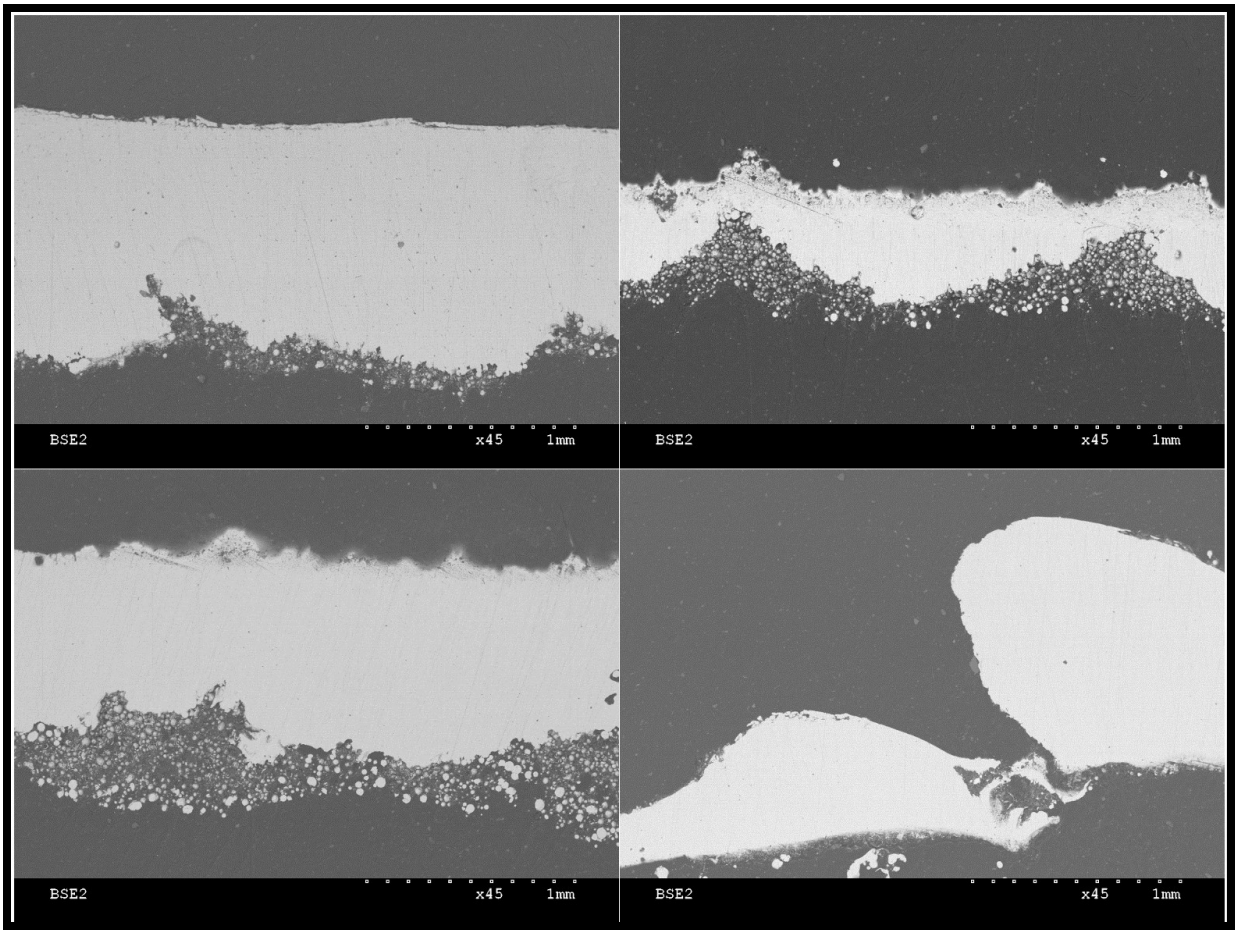

Figure 7.8: Single layer cross-section SEM images of ISLM deposits (left) and laser counterpart deposit cross-sections (right) with increasing laser power (top to bottom at 80W and 100W)

Single layer cross-section images were studied for M1 and M6 (perpendicular orientation), and the laser counterpart samples, M1.1 and M6.1. Primary observations through the SEM micrographs show a consistently dense cross-section for M1 and M6 deposited through the ISLM system (left column). On the other hand, poor homogeneity was observed in the laser samples M1.1 and M6.1. Partially fused raster tracks with non-uniform cross sections were observed throughout the length of the deposit (right column). The process parameters for M1 were 60A of induction current, 80W laser power at a scan speed of 2mm/s while it's laser counterpart, M1.1 at 80W of laser power at

a scan speed of 2mm/s. Both these samples are compared on the top row of Fig 7.8. The same features were studied when the laser power was now increased to 100W and the scan speed to 6mm/s. The M6.1 cross-section displaying an increased porosity in terms of lack of fusion and deposit inconsistency. This could be well accounted for the higher scan speeds not compensating enough for the lower energy input to the deposit. Meanwhile, the cross-section for M6 still was dense throughout with an increased unmelted sintered powder particles at the bottom of the deposit. This observation made a clear indication of the extra energy input from the ISLM coil not only leading to denser deposits but also causing powder sintering to the base of the deposit that would then have to be removed through manual cleaning. Fig 7.9 shows SEM/ BSE images of samples M9 and M9.1 & M12 and M12.1. The scanning strategy for these deposits was parallel orientation. M9 was deposited at 60A induction current, 100W of laser power at 2mm/s while M9.1 with just 100W of laser power at 2mm/s. M12 was deposited at 60A of induction current, 80W of laser power at 6mm/s and the laser counterpart M12.1 at 80W at 6mm/s. Similar features were observed for the ISLM M9 and M12 samples with denser cross-sections throughout the scan while M12.1 had the unfused raster tracks which can be seen as beads in the lower right corner image in Fig.7.9.

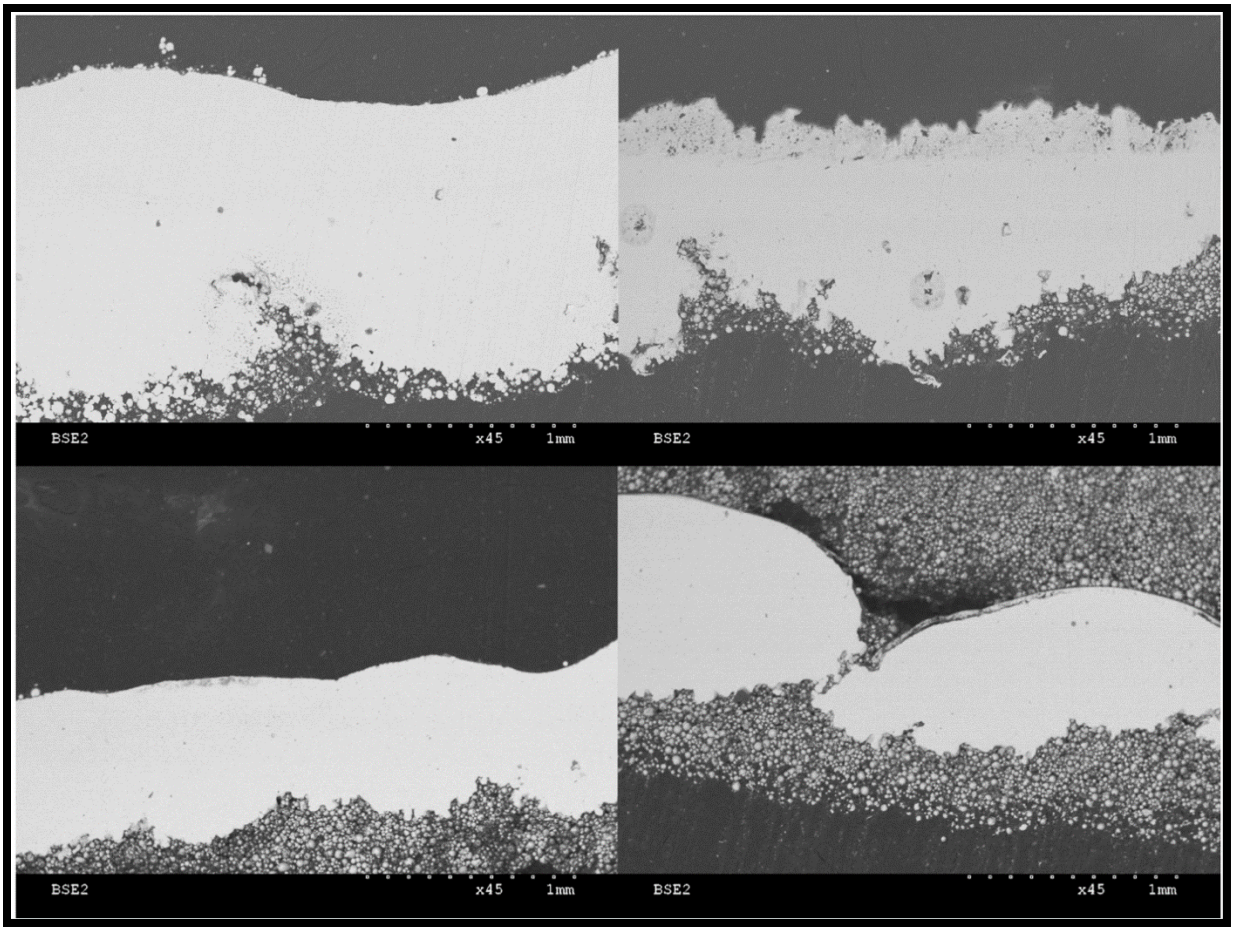

Figure 7.9: Single layer cross-section SEM images of ISLM deposits (left) and laser counterpart deposit cross-sections (right) with decreasing laser power (top to bottom at 100W and 80W)

The gas flow throughout the depositions was set at 50psi. Argon was used to reduce the oxidation levels in the deposits. Typically, a L-PBF process is carried out in an inert atmosphere to minimize or eliminate any defects arising due to increased oxygen levels during the build process. Increased oxygen levels also regulate the resulting properties of the builds. However, to eliminate the complexity of the system design by adding a gas chamber to the system, selective shielding was carried out through the nozzle of the ISLM coil. This can be observed in Fig 6.7 through the CAD design as well as the actual nozzle. The gas flow rate was achieved was reached after a trial of single layer experiments to minimize the oxidation on a macro-scale. The oxidation observed

across all the samples was mainly associated with the sintered powder particles at the bottom of the deposits. This was progressively minimized as shown in Fig 7.10.

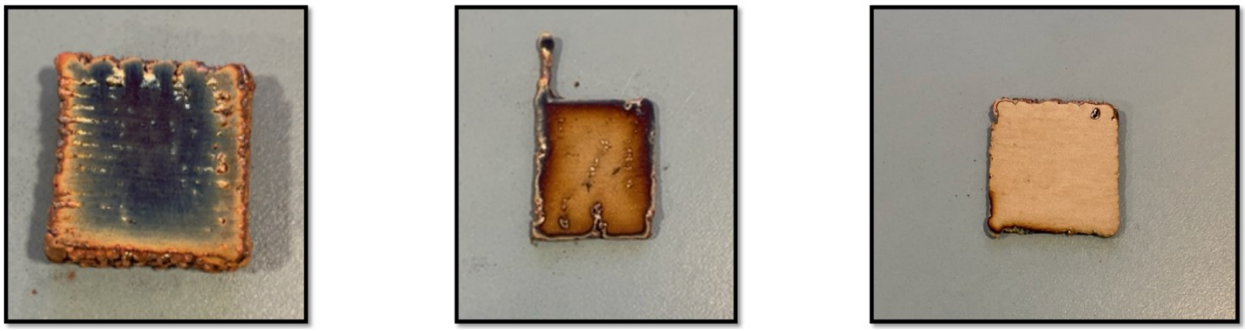

Figure 7.10: Oxidation control in the ISLM deposit (left to right) by variation in the Argon gas flow

7.2.3 Single Layer Deposit Vickers Hardness Measurements

The micro hardness measurements at 300gF for a duration of 20 secs for the single layer samples were divided into two stages depending on their scan orientations. As induction plays a significant role in regulating the density of these deposits, as can be seen from the discussion in Section 7.2.2, variation of hardness is also expected among the samples falling under the categories of "perpendicular" and "parallel" orientation. The results shown in Fig 7.11 and Fig 7.12 depict the variation of hardness of the ISLM samples with a direct comparison of their laser counterparts. It must be noted that for samples M1.1 and M7.1, hardness measurements were not conducted given their poor cross-sections. On the overall, a general trendline of harder ISLM cross-sections as compared to their laser counterparts was observed when the samples were deposited in the "perpendicular" orientation. While, for the "parallel" scanned samples, the ISLM sample cross-sections appeared to be softer compared to their laser counterparts. With the orientation of the scan being the only variable in these two sets of experiments, it could be concluded that the effect of induction was more pronounced in the for parallel scans as compared to the perpendicular scans.

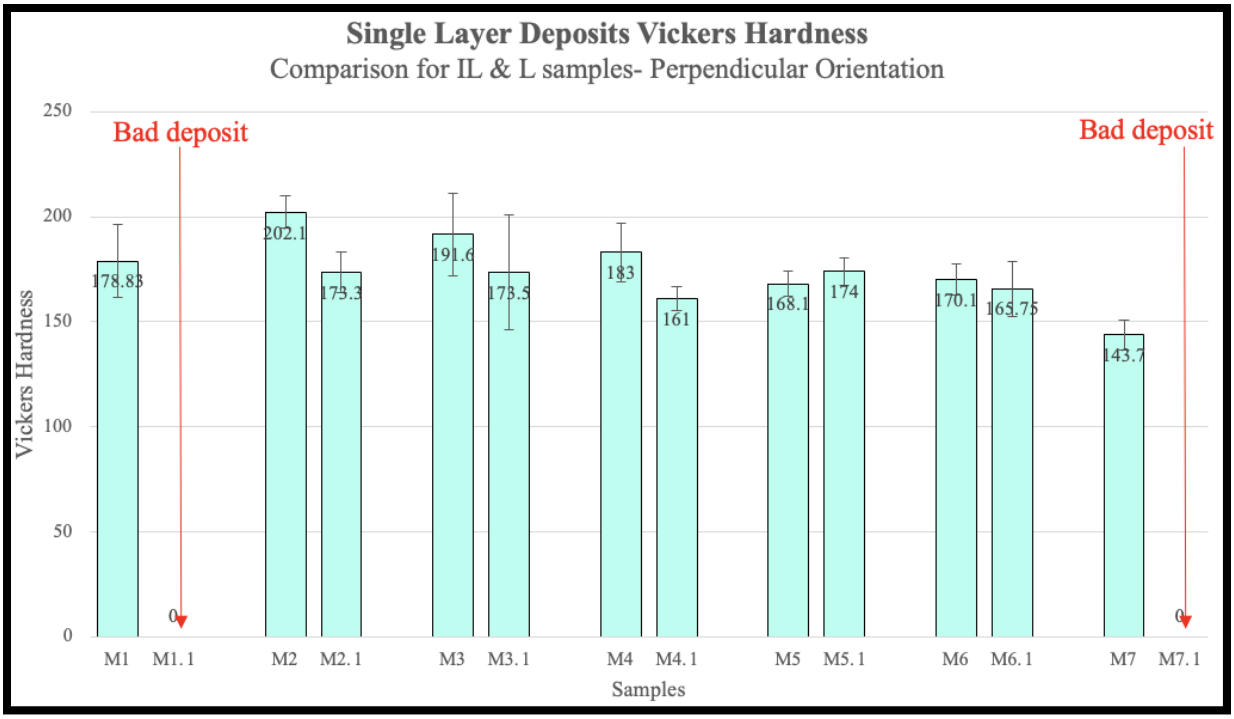

Figure 7.11: Vickers Hardness for ISLM deposits with perpendicular orientation

The overall results obtained for both the scan strategies are lower as compared to that reported in literature for austenitic steels [49] [50]. The effect of heat-treatment on deposits made through SLM have usually shown softer hardness values as compared to their as-is laser counterparts [51] [52]. The decrease in hardness comes even after a consistent density throughout the cross-section of the ISLM samples even with the scan speeds being varied with incremental variation in the laser power.

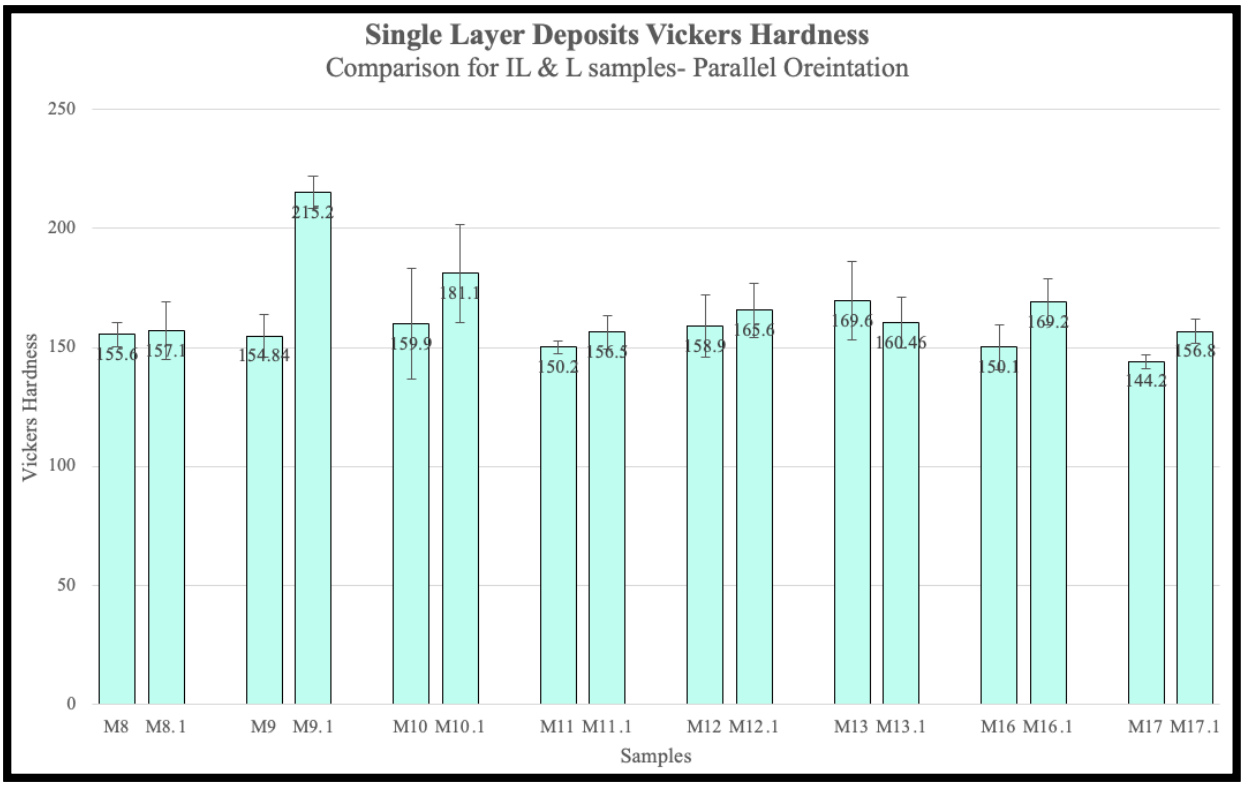

Figure 7.12: Vickers Hardness for ISLM deposits with parallel orientation

The variation of hardness across the cross-section of the ISLM samples, M4 and M9, with perpendicular and parallel scanning strategies respectively shows the effective coupling area of the coil to be approximately at the 50% mark of the in the width of the deposit. Both the cross-sections show considerable variation in this highlighted region which can be seen in Fig 7.13. The highlighted area signifies when the coil is completely on top of the deposit area as a result of which, the induction of magnetic flux in the deposit is the highest in this region leading to a variation in the hardness depending on the respective scanning orientation. However, the obtained Vickers Hardness values are comparable to the heat treated 316L deposited samples through the L-PBF process when processed through the parallel scanning and higher when deposited with perpendicular scanning [53].

Orientation	Average Hardness (HV)	Standard Deviation (HV)
Perpendicular	176.77	18.78
Parallel	155.41	7.7

Table 7.3: Vickers Hardness for ISLM single layer deposits

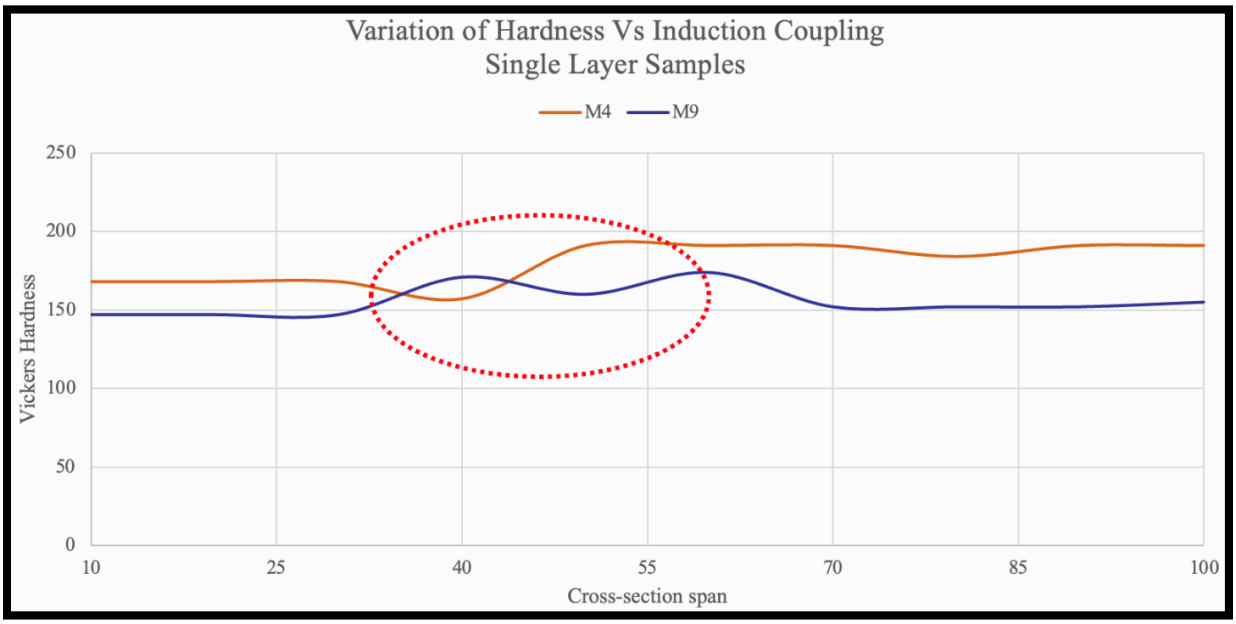

Figure 7.13: Vickers Hardness across cross-section of ISLM deposits for both orientations

7.2.4 Tribological Behavior Analysis

The tribological behavior of the ISLM and laser-only deposit surfaces were studied under defined loading conditions at room temperature using a CSM ball-on-disc Tribometer. Prior to testing, all deposit surfaces were polished upto and with a 1200 grit SiC polishing paper. This helped in minimizing excessive tangential loads on the deposit during testing.

The sliding tests were conducted under a load of 9N at a maximum linear speed of 3.25cm/s. The acquisition rate was set to 9Hz and a 6mm diameter SS316 ball was used procured from McMaster

Carr to be used as a static friction partner. The wear track developed after the test was further analyzed and the wear track and ball debris was collected for future study

The test utilized a few initial cycles to achieve a uniform wear track. The wear test results were benchmarked with a standard annealed SS316 coupon procured from McMaster Carr displayed by the black curve which also had the highest variance in the measurement compilation. Similar wear behavior was observed among the ISLM, laser only and the benchmark SS316 coupon.

The wear tracks generated from the wear tests were now measured for their profile to understand the behavior of the ISLM and laser-only sample. The width and the depth of the wear tracks represent the overall volume loss of the material from the deposits after the ball-on-disk measurements. The depth of the tracks is directly linked to the hardness of the material which was influenced by the processing parameters used to deposit the respective samples [54]. Fig 7.15 shows compiled results for the same

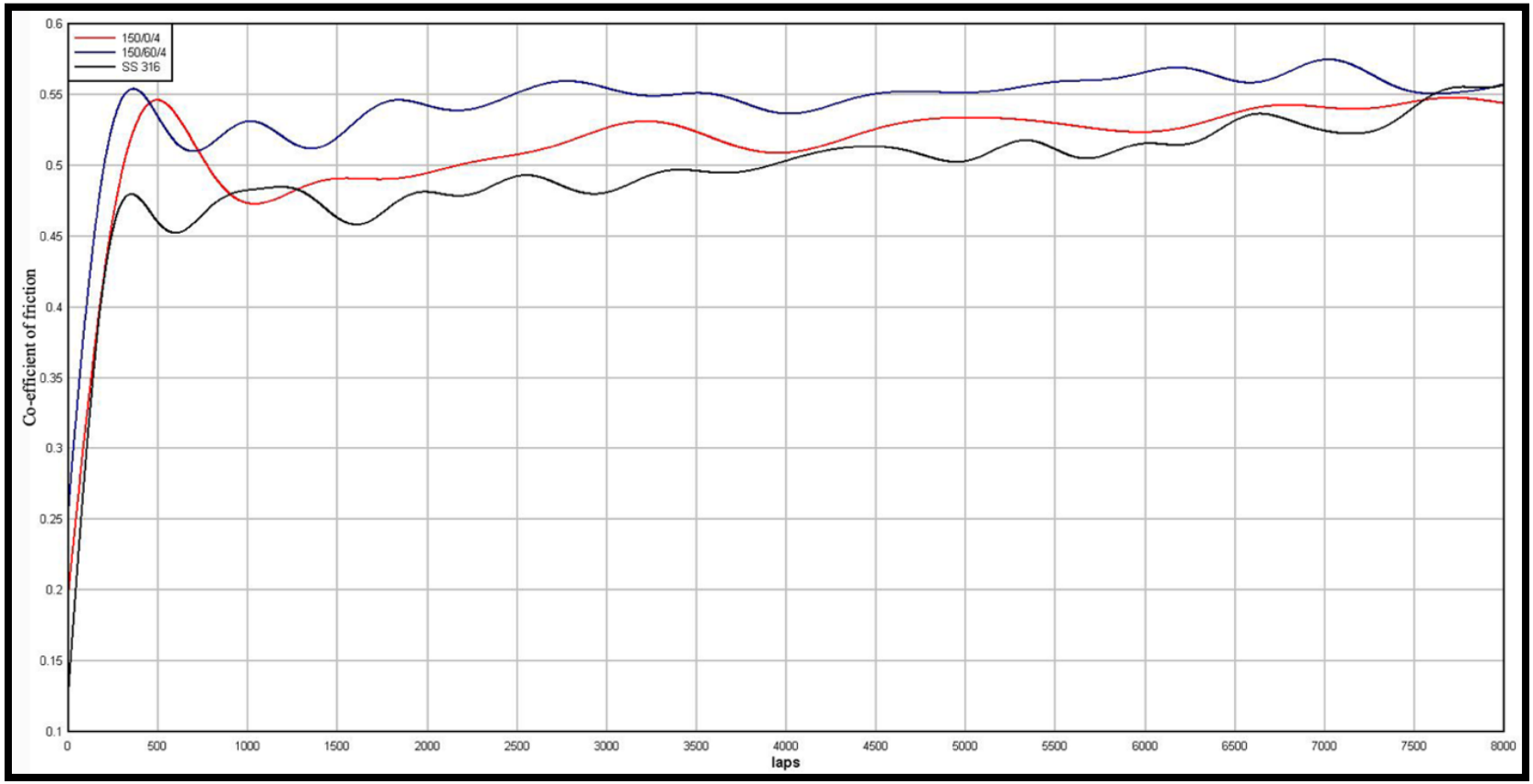

Figure 7.14: Tribometer profiles for ISLM and laser-only deposits

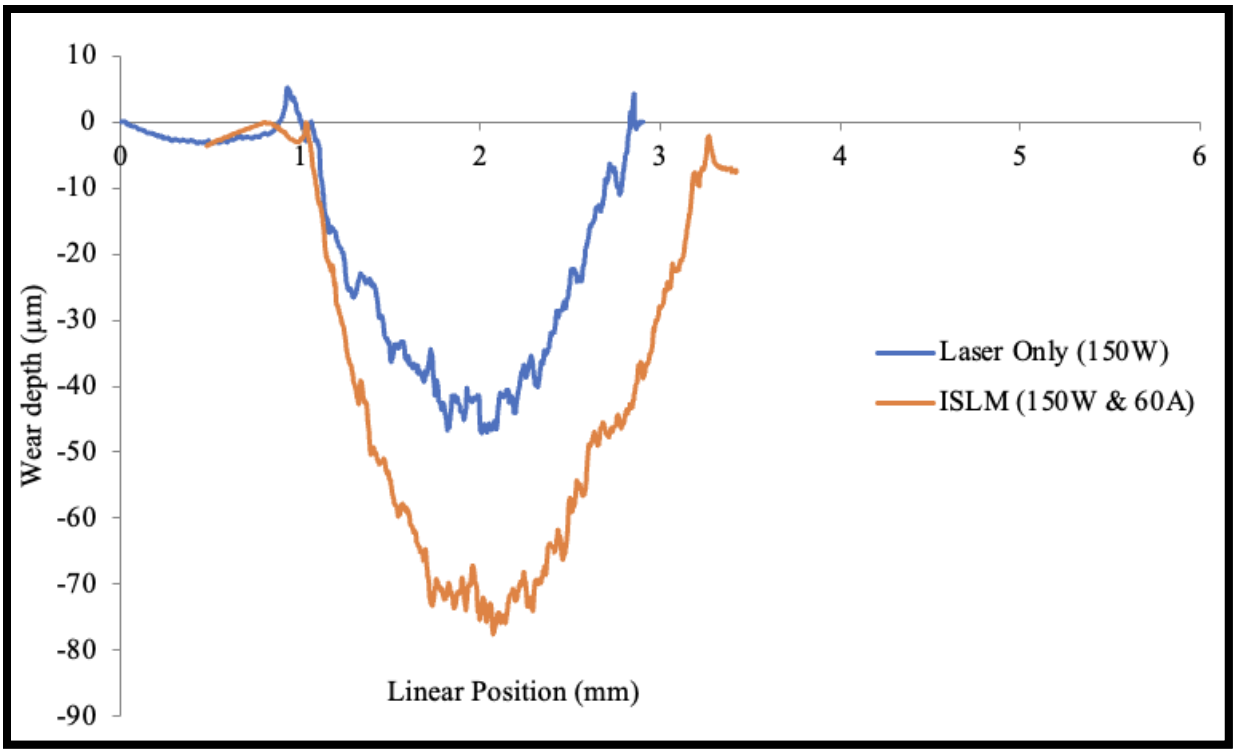

Figure 7.15: Wear depth for ISLM and laser only deposits in mm

The average roughness value for the ISLM deposit was 10.34µm (Ra) while that of the laser-only sample was 13.73µm. The wider and deeper wear track for the ISLM deposit concluded the softening of the surface due to the presence of induction leading to more wear as compared to its laser counterpart.

7.2.5 Corrosion Test

The electrochemical dissolution of stainless steels is regulated by the stability of its passive oxide film. The physical and chemical composition of this oxide film defines the mechanical integrity of the final deposit. The properties of the AM deposits, in general, are dependent on their resulting

microstructure which is directly related to the processing parameters used to deposits the samples. Higher cooling rates, usually observed in AM parts tend to reduce the MnS inclusion nucleation time in stainless steels. This ensures homogenous distribution of the alloying elements throughout the matrix and balances out the formation of any Chromium depleted regions. These favoring conditions hypothesize the enhanced corrosion resistance of AM SS316 in acidic environments [42] [55] [56] [57].

Fig 7.16 represents compiled potentiodynamic curves of the ISLM and its laser-only counterpart deposit.

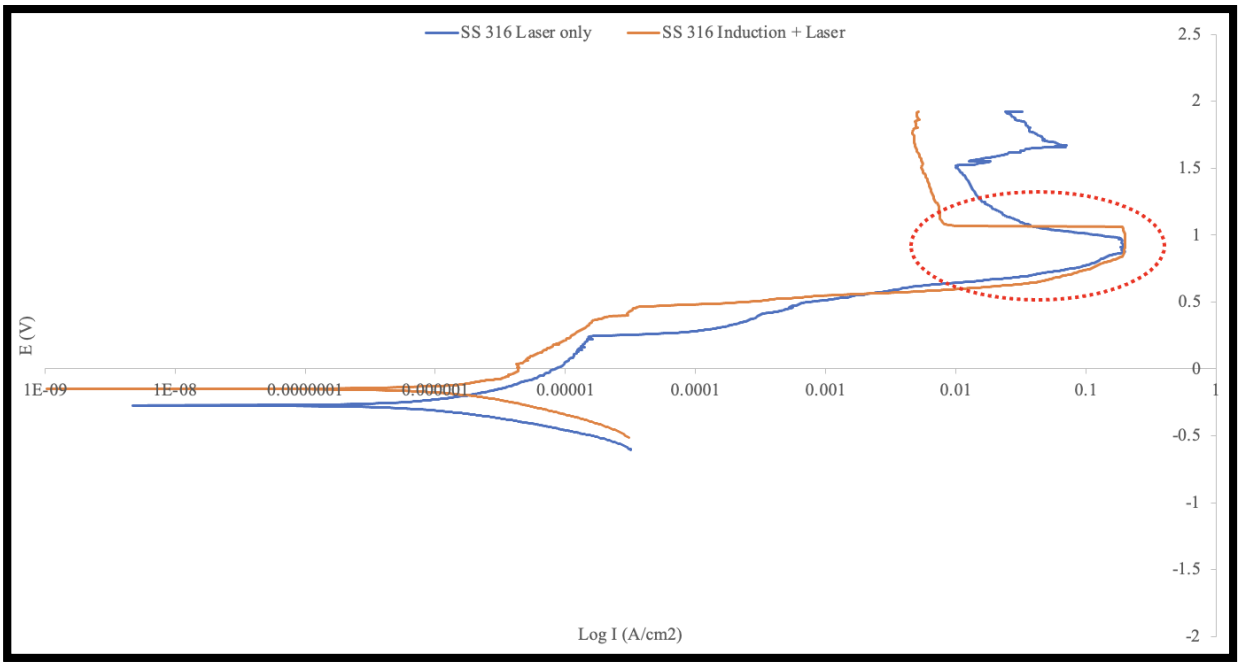

Figure 7.16: Potentiodynamic curves of ISLM and laser only samples

The corrosion behavior of the deposits were measured by the galvanic technique. An Ag/AgCl and Pt wire combination were used as reference and counter electrodes respectively. A 0.5% NaCl solution was prepared to be used as the electrolyte for the test. All the tests were conducted at room temperatures to measure the polarization behavior (potentio-dynamic curve) for a range of -

1V to 2V at a scan rate of 1.66mV/s. The collected data was analyzed for Tafel-fitting using a commercially available software (EC-lab). The results were tabulated in Table 7.4 and illustrated in Fig 7.16. From Table 7.4., it can be seen that both the samples have similar Ecorr values of -187mV and -198mV respectively. Sharp passivation points were observed for both the deposits as highlighted in Fig 7.16. Lower Icorr values were observed, from Table 7.4, for both the samples and are often related with lower corrosion rates [58]. The Ecorr and Icorr were obtained through Tafel fitting as seen in Fig 7.17.

Sample	Ecorr (mV)	Icorr (µA/cm2)	ßa	ßc
ISLM	-187.764	9.36E-04	159.7	149.8
Laser only	-198.186	6.61E-04	171.1	151.1

Table 7.4: Corrosion potential and Tafel slopes for ISLM and laser-only deposit

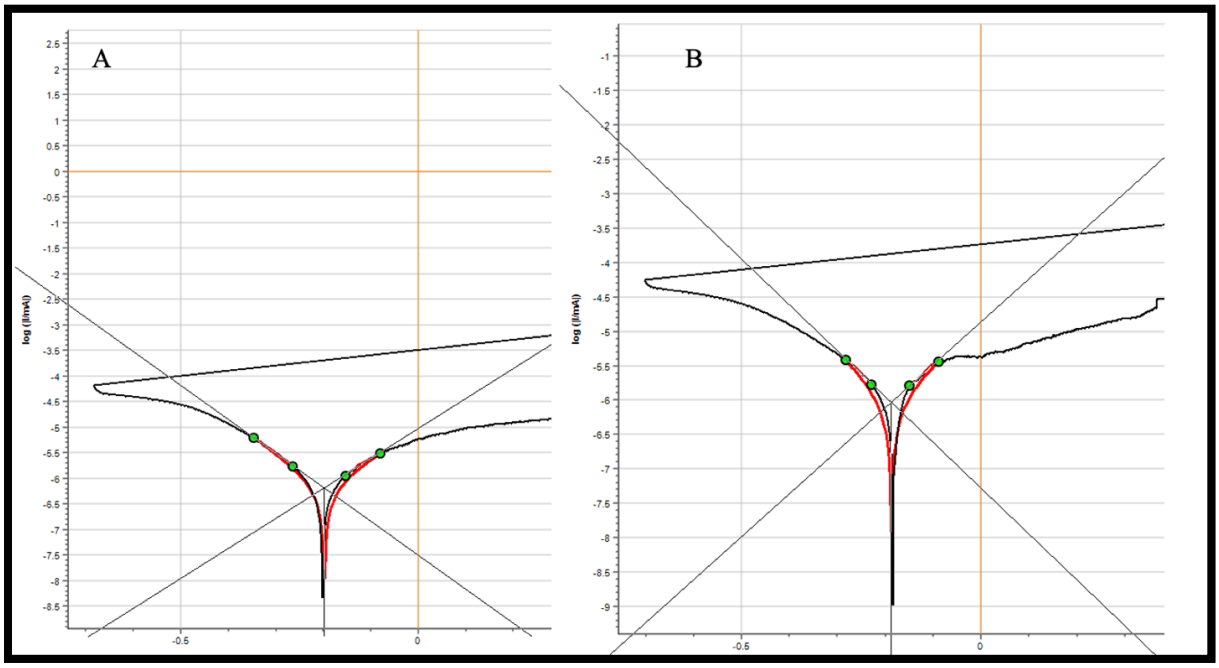

Figure 7.17: Tafel fitting for (A) Laser only deposit and (B) ISLM deposit

7.2.6 Multi-layer Deposit SEM Cross-section Analysis

The characterization study for the single layer deposits helped in optimizing, by elimination, process parameters required to run multi-layer deposits. The comprehensive analytical study also gave a fair understanding of the effects of the use of induction and its scan orientation on the resulting properties of the single layer deposits. Taking into consideration the conclusions of the study, three sets of two-layer deposit experiments were carried out. The approach towards conducting both, single and multi-layer, deposits was to not fuse the starting layer to the base as opposed to the conventional practice for a SLM process. This eliminated several post-process requirements such as wire EDM cutting of the deposit from the baseplate, grounding new baseplates and machining them as per design tolerances of the powder bed. On the other hand, the added input of an auxiliary heating source meant extra energy being fed to the deposits leading to significant warping at the edges of the deposits. This was mainly due to the starting layer of the deposit not being fused to the baseplate and the heat radiation and convection being higher and on the edges of the raster scan of the deposit. This limited the scope of the multi-layer deposits to two layers. However, as a proof-of-concept, significant results were observed and are explained in detail in the following discussion.

Continuing the approach of depositing a laser-only counterpart for every ISLM deposit was not achieved with the two-layer deposits. The primary reason being the lack of fusion between the two layers meant that both the layers would easily peel off after the deposition was complete. Comparatively, an addition of the ISLM coil facilitated easy deposition of the two-layer deposits. This proved to work in favor of the ISLM concept in addition to the single layers deposits, the properties of which were regulated by the choice of the scanning orientation. The three deposits

used a combination of the scanning strategies. The first deposit named D1 was deposited with both the layers scanned in the “perpendicular” orientation. Deposit D2 was deposited with both the layers scanned in the “parallel” orientation while D3 was deposited with the first layer scanned in the “perpendicular” orientation while the second layer in “parallel”. The reverse combination of D3 was not achieved with both layers peeling off. A detailed discussion of this limitation is discussed in the following sections.

Fig 7.18 shows cross-sectional SEM images of the tail end of D1 and an illustration of the cross-section in general. A dense deposit was observed throughout the length of the sample. Completely fused layers were observed with no distinct line of separation of layers. D1 was deposited with 100W for the first layer and 150W for the second layer with 60A of induction current at 2mm/s for both the layers.

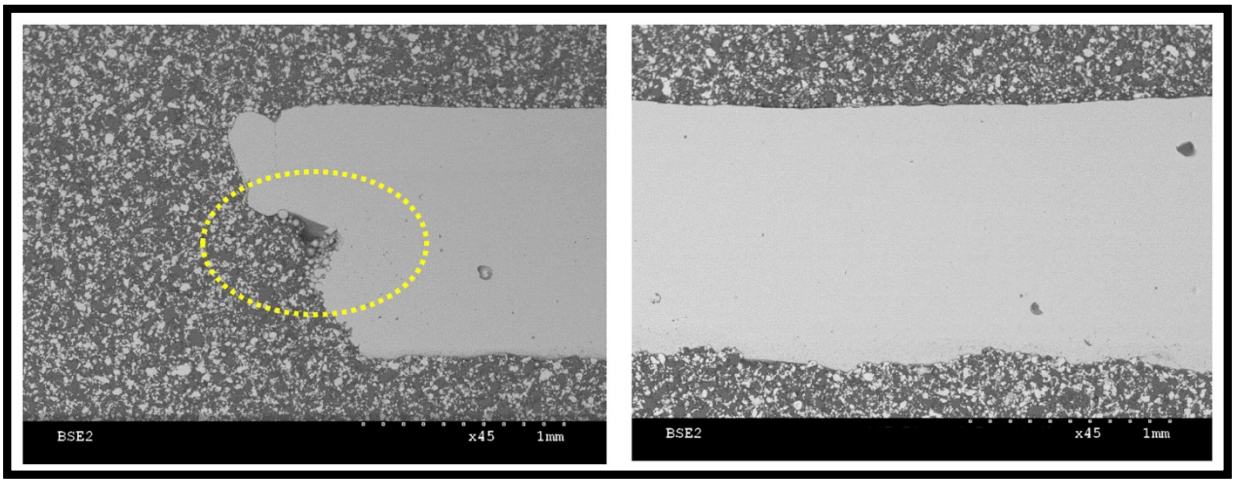

Figure 7.18: SEM images of D1 at (A) Tail end of cross-section and (B) general cross-section representation

It can be seen clearly from Fig.7.18 A, the tail end of D1 with two distinct layers seen at the line of fusion after which distinguishing the two layers becomes difficult. Fig 7.19 depicts the tail end of D2 and the cross-section across the width of the deposit. D2 was deposited with the same process

parameters as that of D1 with the only change being the parallel scan instead of the perpendicular orientation scan for D1. Similar features in terms of dense cross-section are observed throughout the width. The line of layer fusion can be predicted from Fig7.19A based on the nature of the warped layers ending at different inclinations. Following the conclusions made for single layer deposits with the parallel scan, slight warping is observed towards the tail end bottom of the first layer. The single layer deposit characterization study shows that the parallel orientation has softer hardness values which are an outcome of higher heat induced in the deposit due to higher flux generation through induction in the deposit. This explains the warping in the first layer of D2 that effectively translates to the second layer of D2.

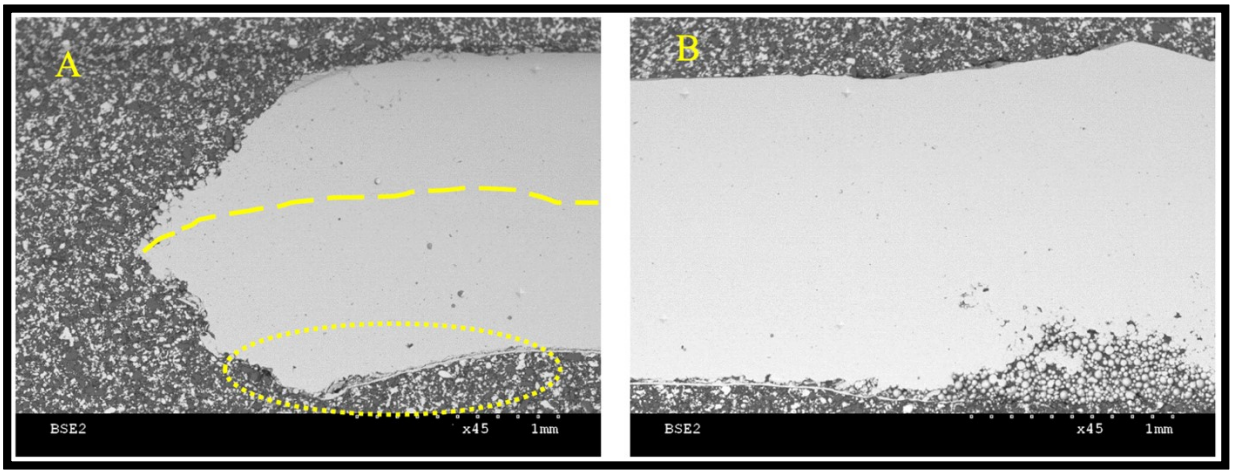

Figure 7.19: SEM images of D2 at (A) Tail end of cross-section and (B) general cross-section representation

Deposit D3 is, as discussed, a combination of a perpendicular and parallel orientation scans for the first and second layers respectively. The processing parameters remain the same as of D1 and D2 with 100W of laser power in the first layer and 150W for the second, 60A of induction current at 2mm/s of scan speed for both the layers. Consistent with the observations made for the cross-

sections D1 and D2, the cross-section of D3 was observed to be dense throughout the width of the cross-section. The SEM images for D3 can be seen in Fig 7.20.

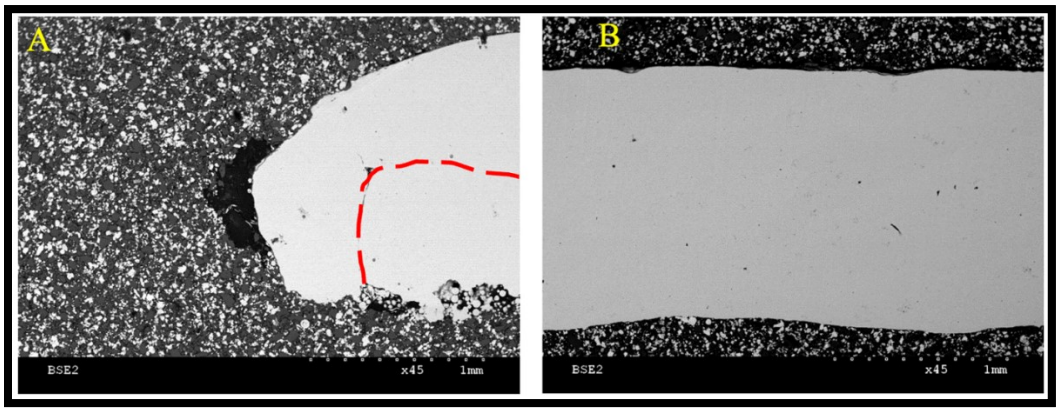

Figure 7.20: SEM images of D3 at (A) Tail end of cross-section and (B) general cross-section representation

Of the limitations discussed about the deposition approach at the beginning of the section, one more limitation can be clearly seen in Fig7.20A. Since the first layer is not fused to the baseplate, it makes it prone to any movement that may occur due to the lateral movement of the powder occurring during the spread of the powder layer by the blade. This can be seen in Fig7.20A where the first layer moved laterally as compared to its programmed position. The second layer can be seen wrapping up on top of this moved first layer with the interrupted line of layer fusion in the region of concern. While the added energy input compensates for good fusion throughout the sample cross-section, the region of discussion could be a potential delamination or a peeling zone giving rise to irreversible defects in the build.

7.2.7 Multi-layer Deposit Microstructural Analysis

The composition range for 316 and 304 stainless steels categorizes their solidification occurring either through the primary ferritic phase or the primary austenitic phase. These differences in their primary solidification phases have an impacting result on the microstructural properties [59] [60]. L-PBF fabricated stainless steels have reported to be completely austenitic with columnar grain structures [61] [62] [63] [64]. Finer stainless steel grains are observed for AM parts as compared to their conventional counterparts [63] [64] [65] [66]. A strong crystallographic fiber texture, aligned along the build direction, with a <001> direction that is against the direction of the fastest heat source removal is observed [45] [67]. Such a strong crystallographic structure may not be observed depending on the scanning strategy adopted. Dendritic growth is observed along this <001> crystallographic direction which is the fastest growing direction as it is aligned with the thermal gradient present throughout the deposition process. The energy source removal from the melt pool, in turn, regulates this thermal gradient which is globally defined by the conduction towards the baseplate along the build direction yet varying locally along the melt pool. Optimizing the process parameters in a way that regulates the shape and size of this melt pool can help modify the overall texture of the melt pool as fraction of each of the melt pool re-melts as the energy source scan the deposits newly spread powder layer [68] [21]. However, the metal AM community still continues its research in order to address the issue of obtaining larger volumes of fine equiaxed grains with a few demonstrations of AM solidification control solution for manufacturing metallic alloys with equiaxed structures resulting in improved mechanical properties [69].

Owing to the dependency of the microstructure of stainless steels on the process parameters set for the processes, conducting a study for the same becomes important. This was done by etching the

deposits D1, D2 and D3 with oxalic acid to reveal their microstructure in a layer-by-layer manner. Fig No.7.21 depicts the microstructure observed for D1 across the entire deposit (figures A and B) and layer-wise (figures C and D).

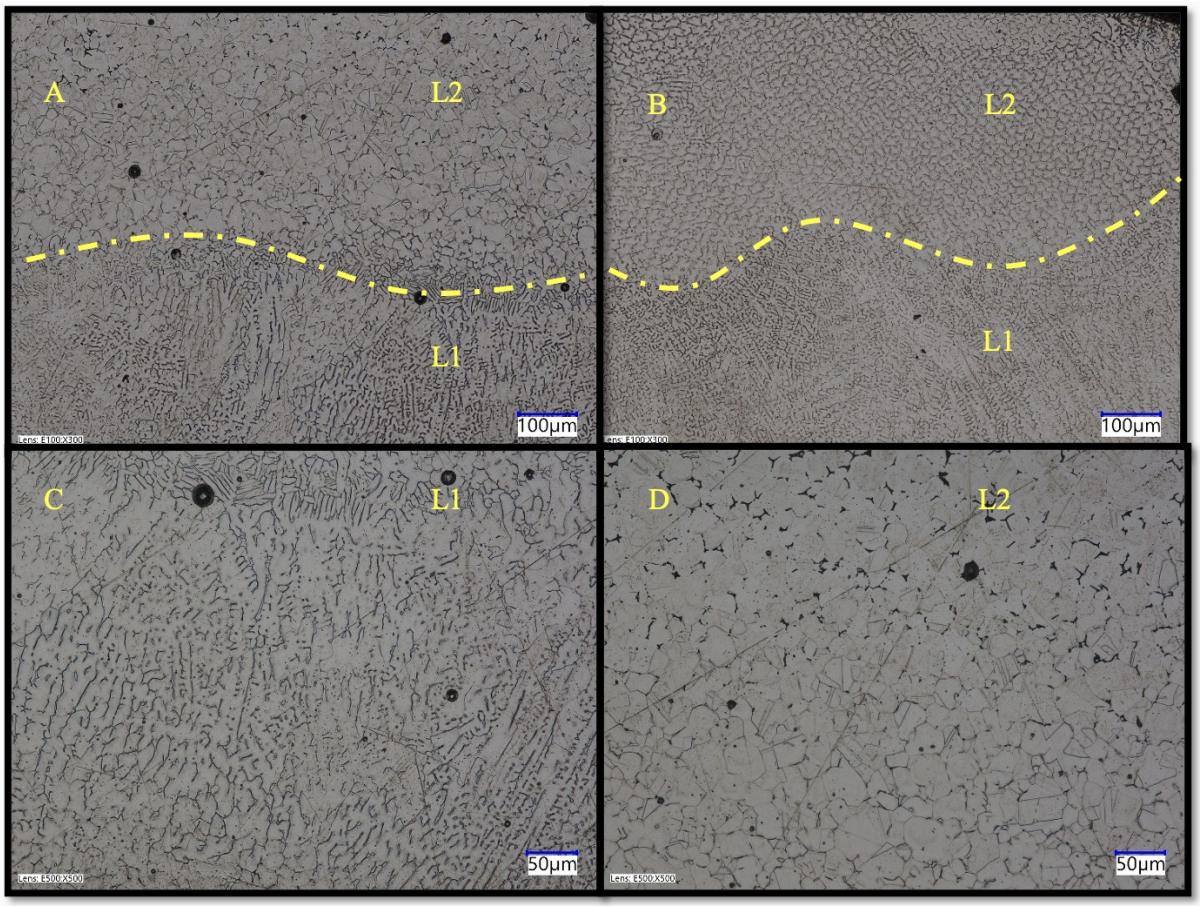

Figure 7.21: Etched SEM images of D1 (A), (B) across the deposit cross-section with line of layer fusion marked, (C) microstructure of layer 1and (D) microstructure of layer 2

The dendritic growth mechanism as explained above was seen in layer 1 of sample D1. This aligns well with the general structure usually observed in L-PBF fabricated stainless steels, as discussed above. However, this also validated the absence of the added auxiliary energy input, regulating thermal gradient defining the microstructure, through the ISLM coil. It was also observed through the analytical study carried out for single layer ISLM samples for perpendicular orientation

scanning (same as that for both layers of sample D1) that with the variation of scan speeds and laser power with fixed induction current resulted in higher values of Vickers hardness validating the poor induction effect in the deposition of the sample. The solidification in the SLM process is complex in nature given the presence of higher cooling rates and high thermal gradients. These higher cooling rates usually lead to a decrease in the equiaxed grain sizes. According to the classic theory of growth kinetics, the ratio of the thermal gradient, G and the growth rate, V regulate the morphology of the growing solid. A steady decrease in the G/V ratio leads to a change of growth mode from planar to dendritic and further modifies the grain morphology from columnar to equiaxed. A relatively high G value with a much slower velocity of the Solid / Liquid line further restricts the morphology of the grains to be columnar. As a result of this, large portion of fine equiaxed structures through SLM processes becomes difficult [70]. Maintaining the thermal cycle in the melt pool to lower the thermal gradient and controlling the scanning speed helps in controlling the cooling rate, T which for a unidirectional heat flow at the solidifying interface is given as [71] [72]

$$T = G \times V. \qquad (6)$$

The growth rate V is related to the laser scan velocity (V_L) under the consideration of a longitudinal section through the centerline of the laser track is given as [73]

$$V = V_L \cos\text{Ø}. \qquad (7)$$

Where Ø is the angle between V and V_L as shown in Fig 7.22.

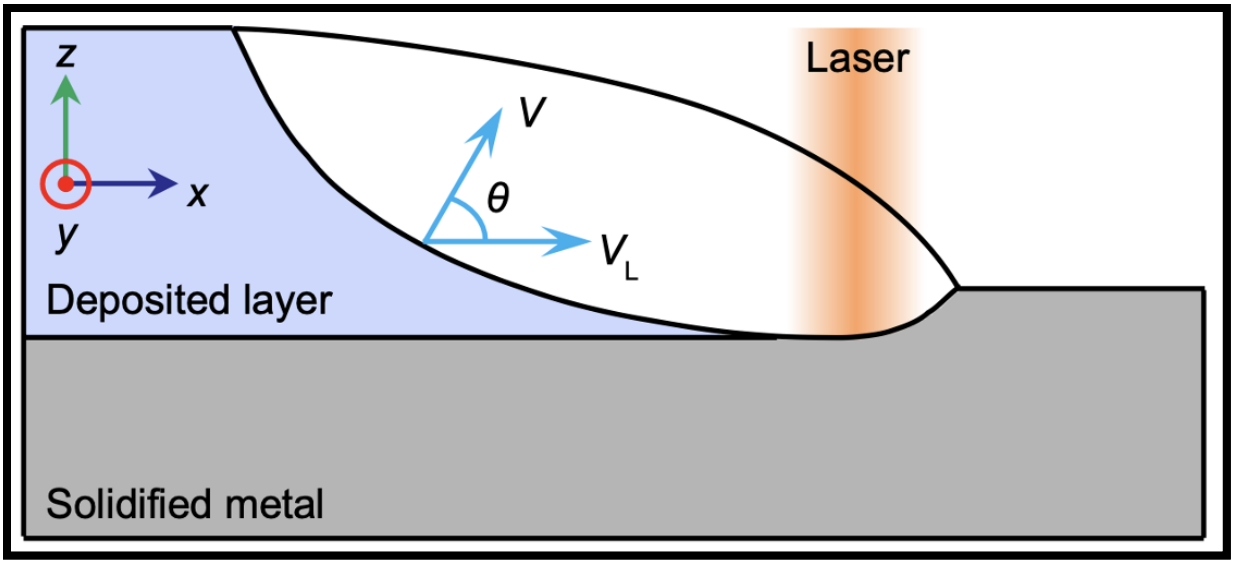

Figure 7.22: The typical form of a melt pool in AM [73]

The deposition of the second layer sample D1 as shown in Fig 7.21 showed a more equiaxed grain growth. This change in the microstructure can be well explained by the discussion above. The lowering of the T value by controlling the thermal gradient with the incorporation of the ISLM coil while running the deposits at comparatively lower scan velocities further regulated the growth rate V, helped in forming the necessary condition favorable for equiaxed grain growth. The deposited first layer formed a very good starting point for the induction to couple more effectively inducing more magnetic flux while simultaneously melting the newly spread powder along with the laser source.

The etched SEM images of sample D2 showed a completely different starting microstructure as compared to layer 1 of D1.

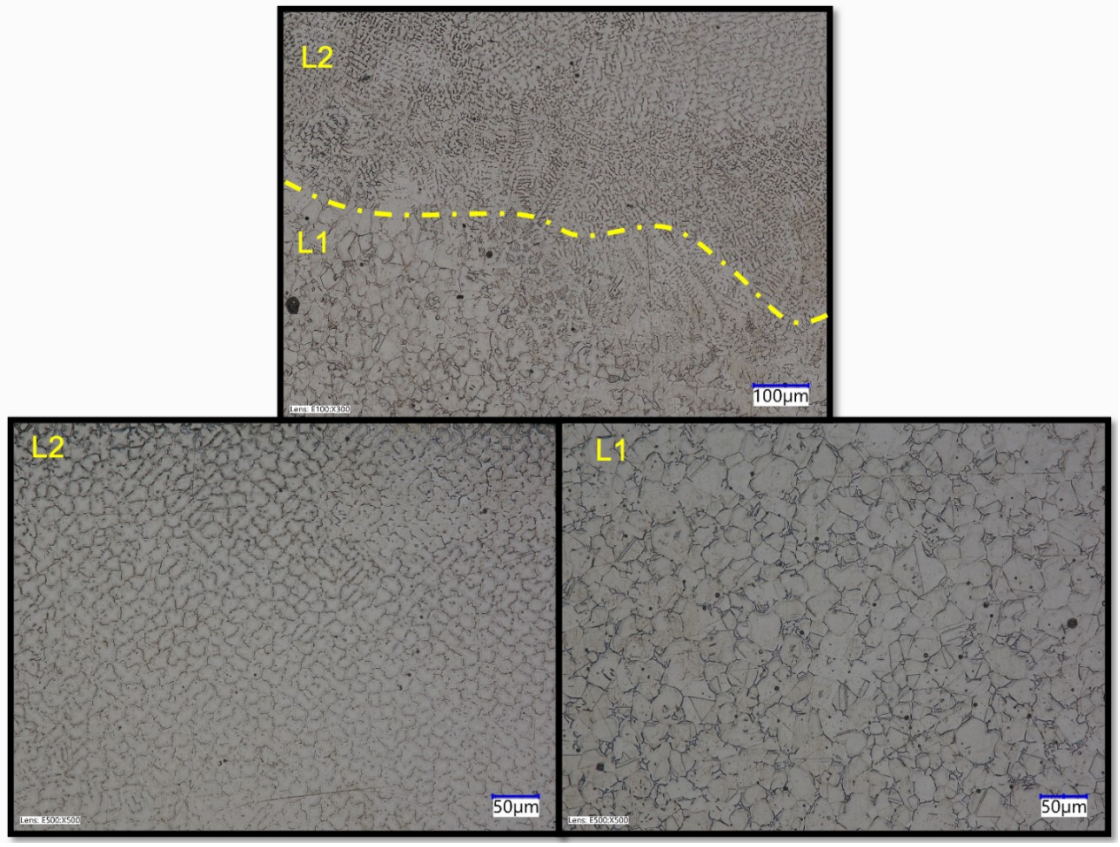

Figure 7.23: Etched SEM images of D2 (Top) across the deposit cross-section with line of layer fusion marked, (lower left) microstructure of layer 2 and (lower right) microstructure of layer 1

The prominent equiaxed structures in L1 and L2 signified the effective control of the cooling rate in sample D2, deposited with the parallel scanning strategy, for both the layers through the incorporation of the ISLM system.

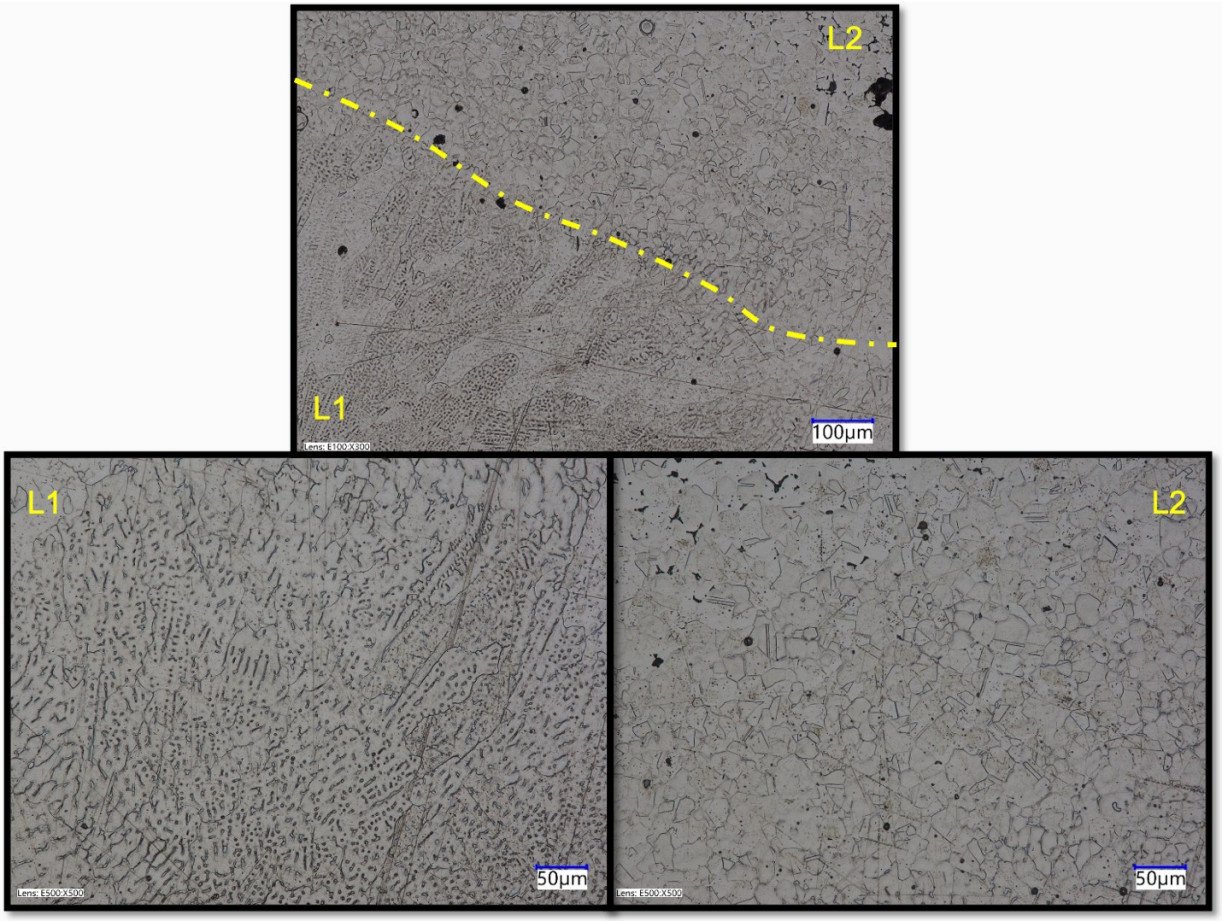

Figure 7.24: Etched SEM images of D3 (Top) across the deposit cross-section with line of layer fusion marked, (lower left) microstructure of layer 1 and (lower right) microstructure of layer 2

Sample D3 was deposited with a mix of perpendicular and parallel scanning orientations with 60A of induction current, 100W of laser power for L1 and 150W for L2 at a 2mm/s scan speed. The microstructural pattern was similar to that of D1 with the first layer exhibiting dendritic growth and the second layer showing equiaxed structures. This further validated the effectively of the ISLM coil to be more favorable in the parallel scanning orientation than in perpendicular orientation.

The variations observed in the microstructures of these samples was further analyzed through their Vickers hardness measurements for each layer and are represented in Fig. 7.25.

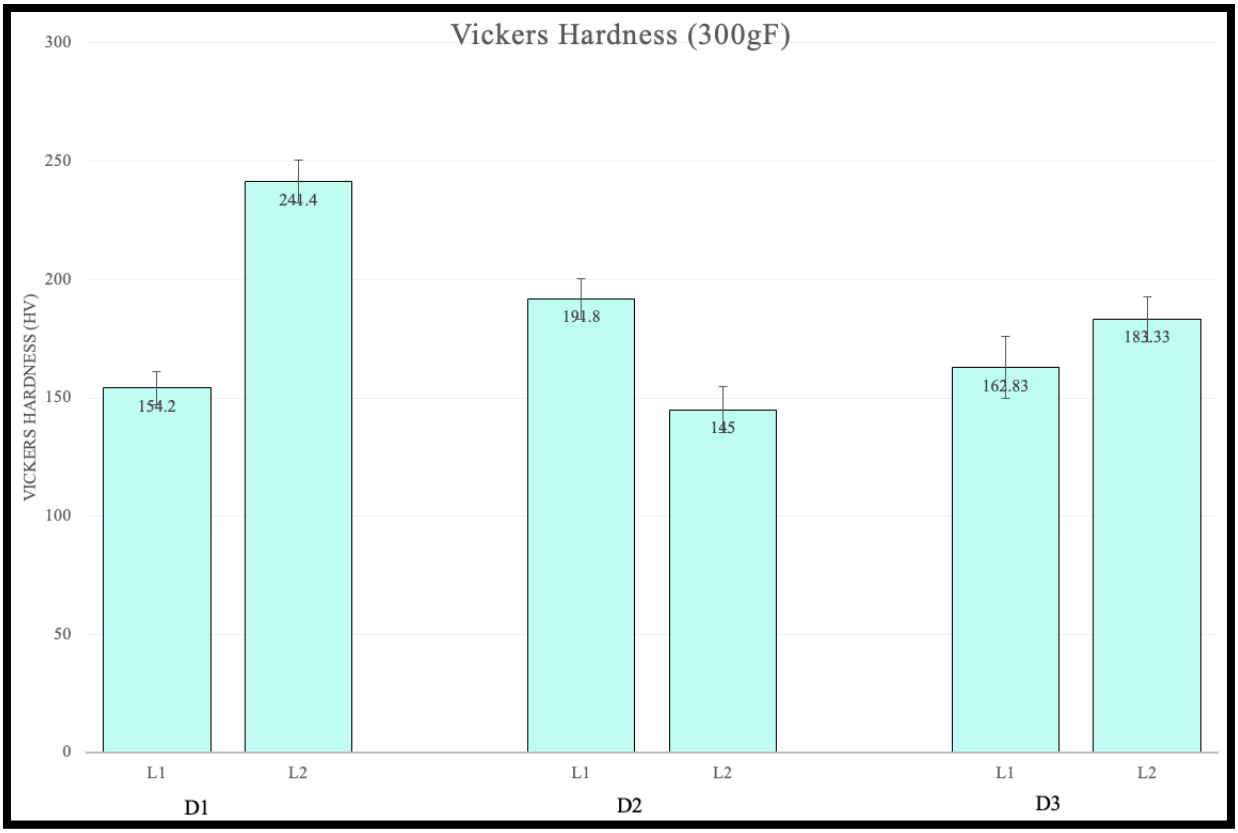

Figure 7.25: Vickers Hardness for ISLM deposits D1, D2 and D3 layer by layer

L1 for sample D1 proved to be softer as compared to L2 of D1 for the perpendicular orientation. On the other hand, the combination of L1 and L2 for D2 turned out to be a softer hardness value given the parallel orientation helped the ISLM coil couple better. Sample D3, a mix of perpendicular and parallel orientation scanning strategies for L1 and L2 depicted similar hardness values for both the layers. A summary of the average Vickers hardness values for samples D1, D2 and D3 can be seen in Table No. 7.5.

Sample	Average Hardness (HV)
D1	197.8
D2	168.4
D3	173.08

Table 7.5: Average Vickers Hardness values for ISLM two-layer deposits

The average hardness values for D1 and D2 samples aligned well with the conclusions from the single layer deposit characterization study. Perpendicular scans usually fabricated harder deposits as compared to the deposits with parallel orientation. The lower hardness values are well reflected by the equiaxed microstructure observed in D2. D3 lies in between D1 and D2 and shows a good combination of microstructure and hardness with the mix of scanning orientations. On plotting the hardness for all samples across the lengths of their respective layers, it is observed that D1 shows the highest variance in transition from layer 1 to layer 2 as compared to D2 and D3.

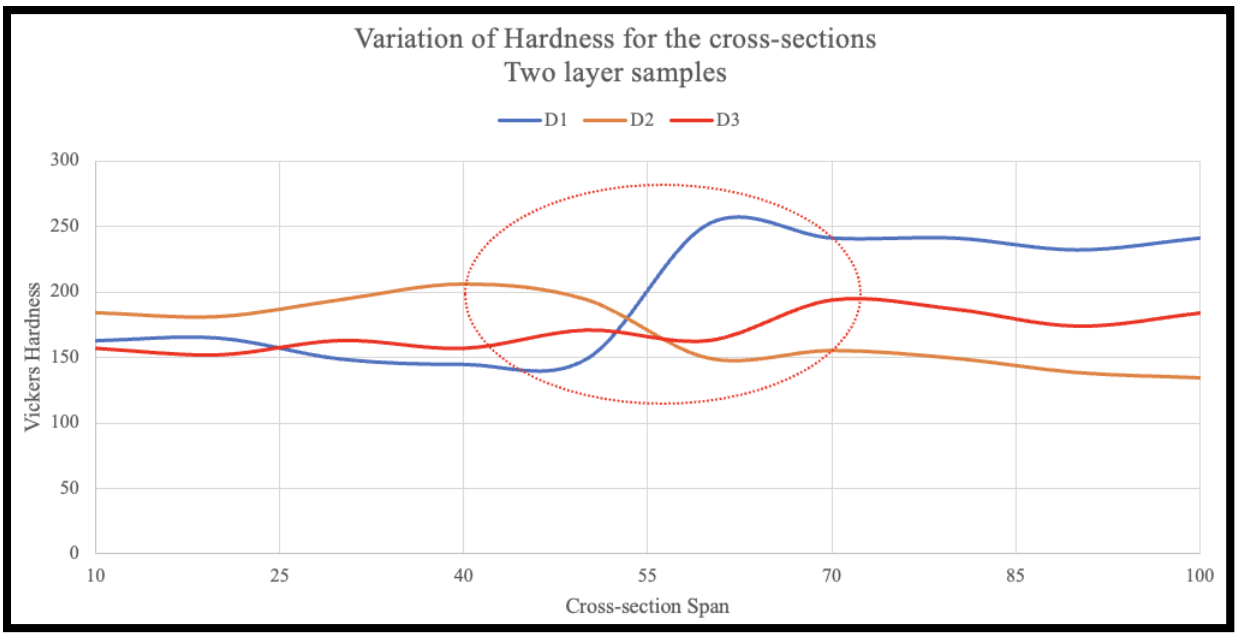

Figure 7.26: Vickers Hardness across cross-section of ISLM two-layer deposits

Chapter 8. ISLM Digital Twin

Process control and monitoring are often implemented in real time to overcome the concerns of quality and consistency in metal AM. In order to obtain more consistent process outputs, efficient alternatives such as the implementation of Machine Learning (ML) platforms have become a field of growing research interest [74]. ML platforms are based on the utilization of an Artificial Intelligence (AI) framework through extraction of essential information from raw data by identifying patterns for addressing complex problems. Machine learning works on the basic principle of advancement of computer programs designed to extract, refine, and use data to learn independently while predicting accurate results through the learning experience. The impact of machine learning has been felt extensively across a range of companies and industries, focusing on data-intensive issues, such as consumer services, control of logistics chains, process optimization, etc. With a reliable training data set, the ML models help in detecting a pattern in the training set and make conclusive inferences based on these extracted patterns [75].

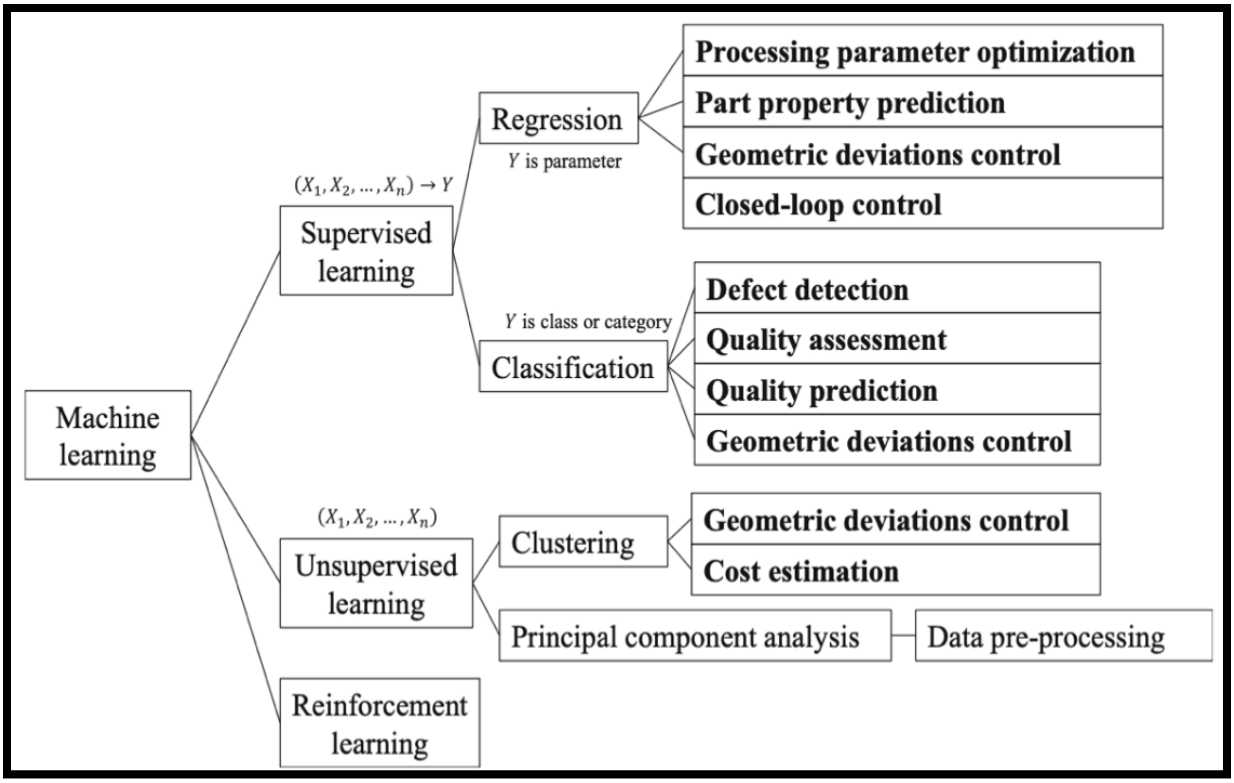

Figure 8.1: Distribution of ML applications in the AM field [75]

The processing parameters in SLM have a very complex and significant effect on the resulting build and its microstructure. Owing to this, the very initiative of constructing a Procedure-Structure-Property Performance (PSPP) prediction model becomes a very difficult task. Also, the AI (ML) strategy has become a substantial method to perform regression analysis and complex pattern recognition without building and fathom the underlying physical models [76] [77]. There are several reasons that limit the prediction of the entire AM process based on any material science driven approach in shorter time spans. It is here where the data driven ML approach finds a good application.

Machine learning works on the development and investigation of frameworks that learn correlations and patterns from the training data information. They are used for a variety of

applications such as defect detection, prediction, classification, regression, or forecasting [77]. However, the data used in such ML models is what define the effectiveness of the model itself. The “No Free Lunch” theorem often used in field of machine learning and optimization imply that there is no single best optimization algorithm, and all optimization algorithms perform equally well with their performances averaged across all problem statements [78]. Given the complex relationship and inter-dependency of the processing parameters of SLM, the dataset size and structure, etc. multiple approaches towards addressing the same research question should be tested. The primary goal of the study is to build a framework for the Digital Twin of the ISLM system to better optimize the process through predictive learning and validation. The layer-by-layer process put to use with different parameters provides a potential source of data at every layer that is processed with the system during the characterization of the built deposits. This dataset includes, but is not restricted to, the porosity / density of the deposit being built, the microstructural characteristics of the material after the layer is processed, residual stresses and the thermal history leading to these stresses being induced in the deposit, the solidification rates and mechanisms, overall mechanical behavior of the part defined by the layer-to-layer modification of the material due to the processing parameters, etc. While some of these outcomes are difficult to be characterized, it only shows the immense digital control the end-user can obtain if the resources to extract such data are easily achievable.

The scope of this study lies in addressing or initiating contributory work towards unlocking this potential of digital control of the ISLM process. The flowchart in Fig 8.2 shows an overview of the approach by dividing the entire process into different stages and highlighting the significance of each of these with a data driven perspective.

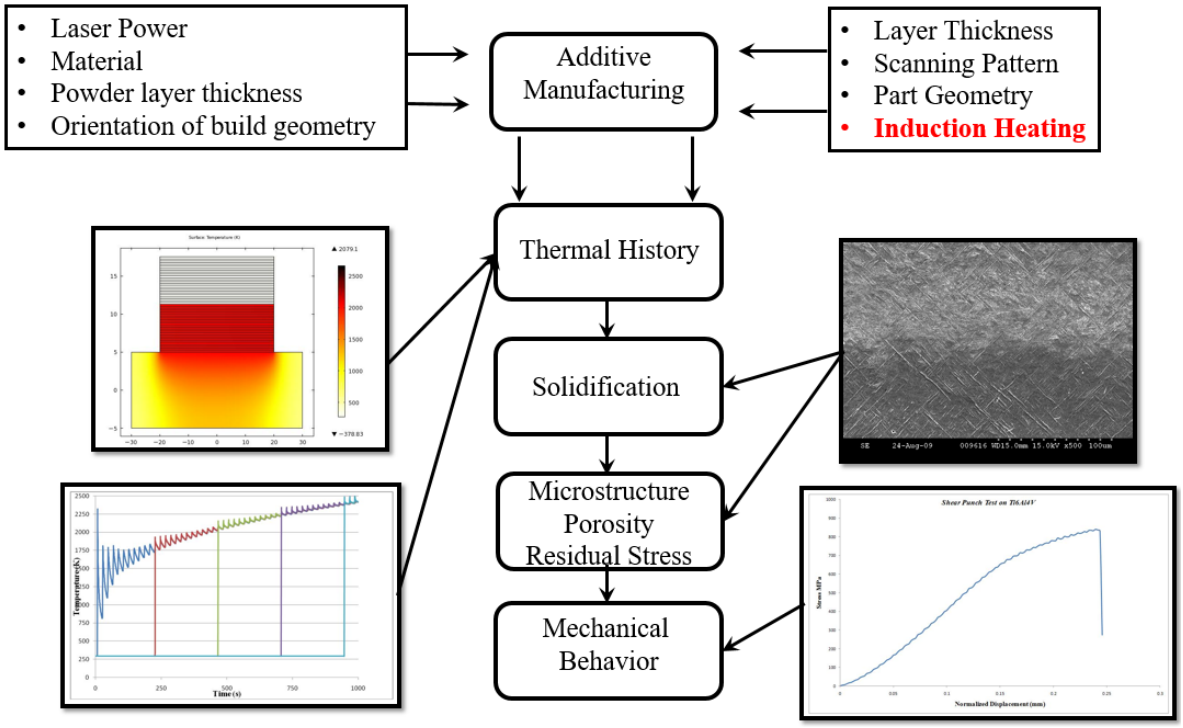

Figure 8.2: ISLM flowchart for a data driven ML approach

Traditionally, design of experiments and physical simulation models are used to optimize the process parameters to additively manufacture new materials or builds. However, the approach is heavily dependent on "trial-and-error" which proves to be expensive in terms of time and the resources used [44] [79] [80] [81]. Physics based simulations can help understand the mechanisms behind the formation of certain features such as melt pool geometry, microstructure, etc. However, these simulation results face macroscopic level discrepancies with the experimental results, at times, due to the oversimplifications by assuming of certain relationships between the processing parameters and the resulting outputs [82]. For various AM processes, ML can be implemented on two levels to relate the process parameters, one on the mesoscale (porosity, relative density, melt pool geometry, etc.) and macroscale (mechanical properties). ML has also been used to serve as a visualization tool in identifying the process windows for various AM processes. At the mesoscale,

single layers form the building blocks of any AM process and can have a direct effect on the final output of the build in terms of melt pool morphology, geometry, continuity, and uniformity [83]. To better understand this significance, Gaussian process (GP) based surrogate models, have been reported, used to construct and highlight the 3D response maps of melt pool depth versus process parameters [84]. Completely dense builds have been the primary objective of all AM studies since porosity significantly affects the mechanical performance of the builds. Multi-Layer Perceptron (MLP) has successfully demonstrated modelling of complex non-linear relationships. Also, even if GP models can estimate the uncertainties in prediction outcomes, the process is more computationally expensive with the same amount of input data as required for the MLP approach. Hence, MLP as well as GP are usually adopted to predict the porosity based on the combinations of process parameters in selective laser melting (SLM) based on the computational resources available [83] [85].

Within the scope of this study is the discussion and application of four approaches towards addressing the mesoscale significance of porosity in ISLM builds. A GP based model, a Neural Network model, a Random Forest Classifier and a Linear Regression model are used to process, train and test the data to predict the porosity based on the characterization data obtained and discussed in Chapter No.7 As discussed, the characterization data obtained through the SEM / BSE images of the single-layer deposits is used to determine the porosity at a fixed magnification scale for each of the deposit. This is achieved by collecting several images of the cross-section and linking each one of them to the respective process parameter of the deposit. This is repeated for both, the ISLM and the laser-only deposits to further quantify the effect of the use of ISLM as compared to SLM. A comprehensive dataset of 295 cross-sectional SEM images were obtained through the characterization study. These images were processed through developed algorithms to

obtain porosity percentages based on the threshold evaluation of the pixels in each given image against the total area of the image. As the magnification of each of these images were set to be constant, the uncertainty of the relative porosity in the deposit based on the scale factor of the images was eliminated. Basic steps of the entire process of converting the image data into numeric values is represented as shown in Fig 8.3. The three-step conversion process started by first getting rid of the data label bar on the SEM images while maintaining a defined crop factor. In the second step, the grayscale image was converted into a high contrast black and white image. The third step included converting the high contrast image's high pixel density count into a numeric value i.e., calculating the contrast tone percentage for a defined area of the image. This percentage value was essentially associated with the process parameters with which the sample was deposited. This step was repeated for the entire data set of 295 images spanning across M1 to M17.1 as mentioned in Table No.7.2. This data was then split in a 80-20 ratio randomly and used as the training and testing data sets respectively. A snippet of the testing data can be seen in Fig 8.5.

Furthermore, the intent of the study was to predict the porosity of the deposit based on the process parameters used for the ISLM and standard SLM processes respectively. Porosity regulation through prediction of process parameters was not included as a part of this study.

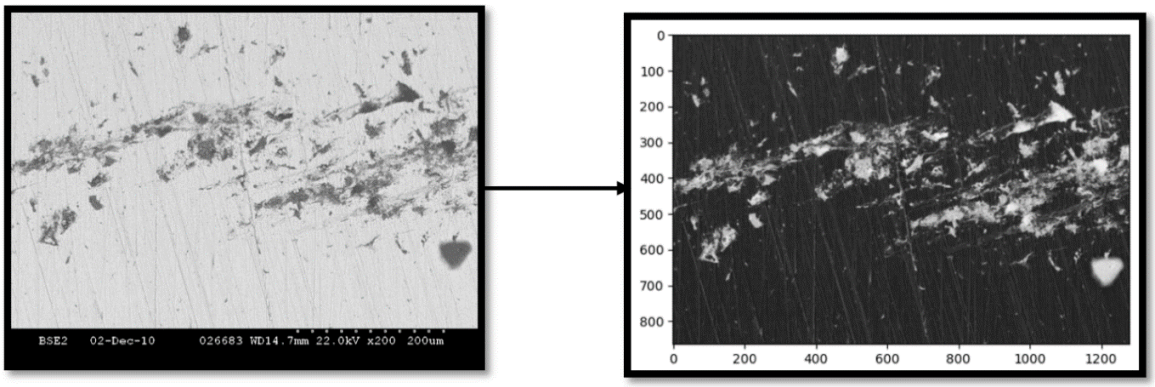

Figure 8.3: Three step data generation from SEM images to numeric percentage porosity values

In the following sections, each of the four approaches have been discussed briefly and their results for porosity prediction have been compared for better understanding of the algorithm for the ISLM process.

8.1 Gaussian Processes

In a simple linear regression approach, a dependent variable y is assumed to be modelled as function of an independent variable x along with a consideration of an irreducible error. The function, thus obtained, however, assumes a linear relationship with the parameters solving a linear function as the output. The GP approach, on the other hand, is a non-parametric approach as it always finds a distribution over all the possible functions arising from the correlations of the variables x and y that is also consistent with the provided dataset. A prior distribution that gets updated on the observation of new data points is needed similar to all other Bayesian methods producing a posterior distribution over functions. The prior defines the distribution of the functions based on possibly how the data may be interpreted. This helps in achieving a smoother function. This smoother function is regulated using a covariance matrix to ensure that the values that are close in the input set will result in output values that are also close together. This covariance matrix along with a mean function to generate the output value of the defined function collectively is known as the Gaussian Process [86].

As discussed, the data was randomly split into a 80-20 ratio for training and testing purposes and each of the mentioned approaches were tested. For the GP approach, the comparison of the actual porosity vs the predicted porosity is represented in Fig 8.4. The extreme outliers were eliminated from the testing data set to reduce the variance in the prediction model and a total of 57 data points

were tested across all the approaches. An absolute mean error of 3.30% was achieved using the GP approach for porosity prediction.

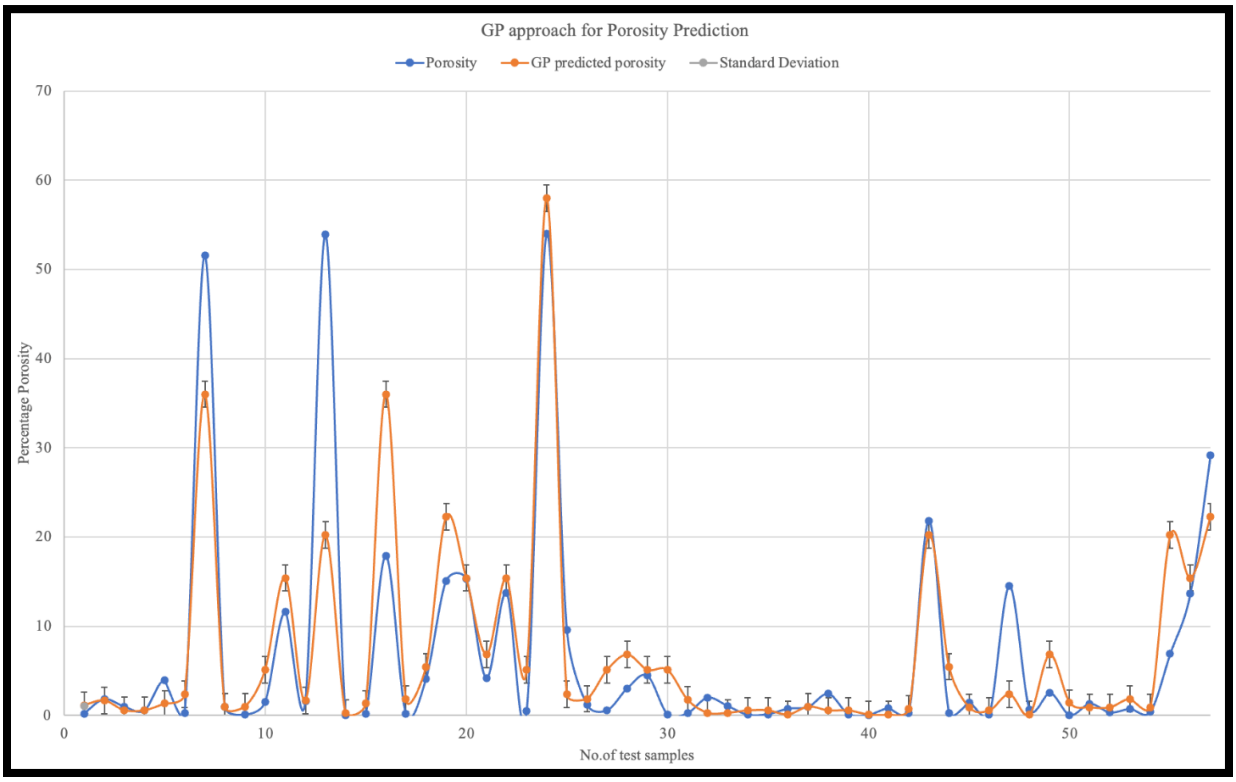

Figure 8.4: Actual porosity vs predicted porosity using the GP approach

8.2 Linear Regression Model

For all is simplicity, linear regression is the most basic and widely used approach in ML. In the case of a single predictor, the least squares fit is the line that minimizes the sum of the squared distances between the observed and predicted values i.e., it minimizes the Residual Sum of Squares (RSS). The function for the predicted observation can then be given as

$$y_i = C_0 + C_1 x_i. \qquad (8)$$

whereas the actual value and the function can be written as follows.

$$y_i = C_0 + C_1 x_i + e. \qquad (9)$$

The residual or the error, e, between the actual and the predicted values become important for how the model is reasoned. In the case of multiple regression scenarios consisting of n predictors, the outcome is modelled as

$$y_n = C_0 + C_1x_1 + C_2x_2 + C_3x_3 + \ldots\ldots + C_nx_n. \qquad (10)$$

In such a setting, the derivations of the co-efficients of the parameters isn't as straight-forward as that for the single case predictors. Usually, calculus is used to derive the partial derivative of the function w.r.t each parameter and then solved for that particular parameter by setting its derivative equal to 0 [87].

Similarly, the co-efficients for each of the parameters in the ISLM process namely Laser Power (W), Induction current (A), Scan speed (mm/s) and scan orientation (perpendicular or parallel) were calculated to finally estimate the porosity as a linear function of the sum of the product of the parameters and their respective co-efficients. The co-efficient values turned out to be as follows:

$C_0 = -0.038$, $C_1 = -0.1159$, $C_2 = -0.1608$, $C_3 = 0.1839$ and $C_4 = -0.2323$.

The major limitation of the linear regression model is the overfitting of data because of the fixed assumption of a linear relationship even for non-linear dependencies. As a result of this, an absolute mean error for the linear regression approach was obtained to be 7.39%. Visual representation of the actual porosity vs the predicted porosity through the Linear Regression model is as shown in Fig 8.5. The same testing data used for the GP approach was used for the linear regression model.

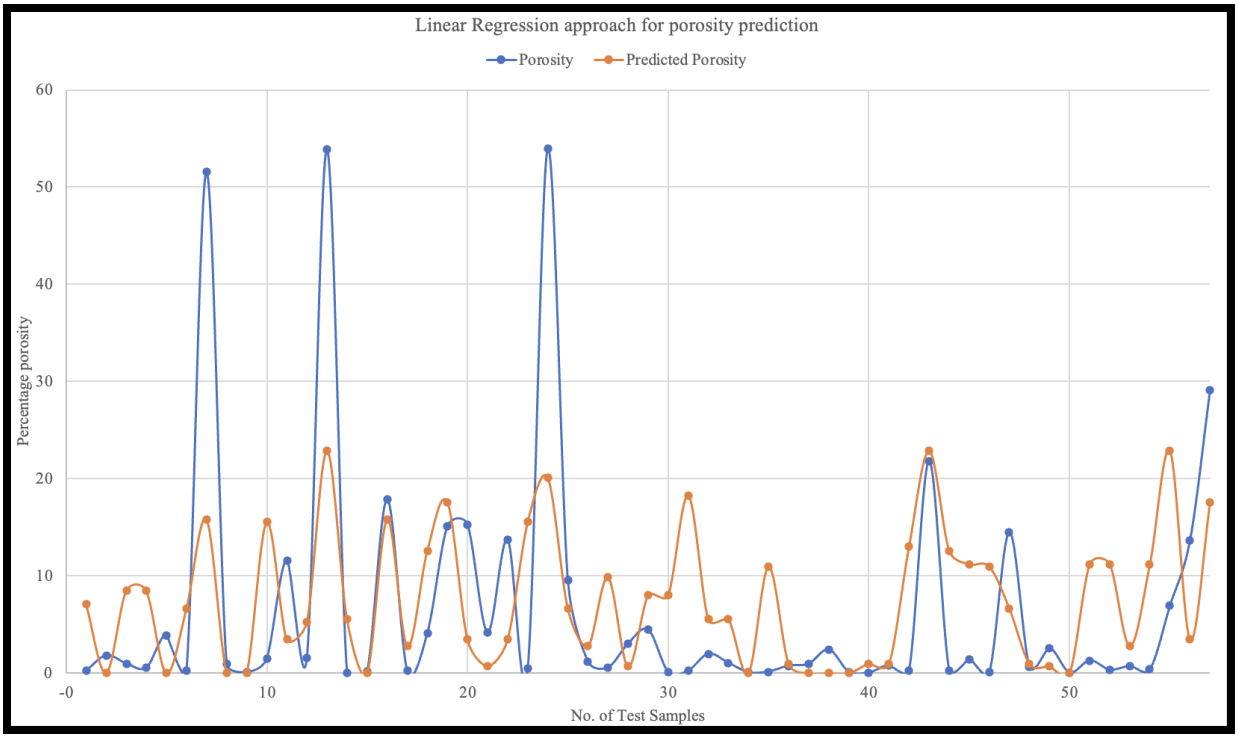

Figure 8.5: Actual porosity vs predicted porosity using Linear Regression

8.3 Feed Forward Neural Networks

An artificial neural network in which the connections between the different nodes does not form a cycle is known as a Feed Forward Neural Network. As information is only processed in one direction, it is the most simplest form of a neural network. Even if the data may pass through multiple hidden layers, it never moves backwards.

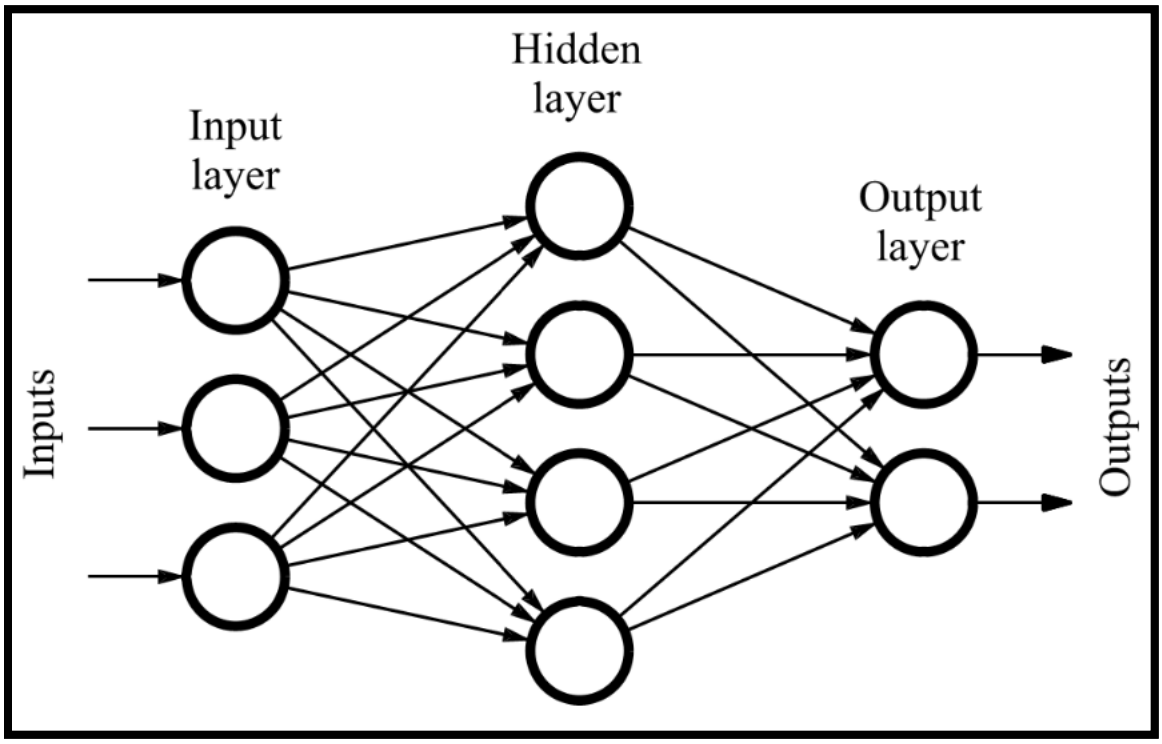

Figure 8.6: Sample of a feed forward Neural Network [88]

Most commonly seen in its simplest form as a Single Layer Perceptron, a Feed Forward Neural Network consists of a series of inputs that enter the layer are multiplied by the weights. The weighted input values are then added together. If this sum is above a specific threshold, the value often produced is 1. However, if the sum lies below the specific threshold, the value produced is -1. The process of updating weights is almost analogous in multi-layered perceptrons. Given their simplified architecture, Feed Forward Neural Networks, being straightforward, can be used with added advantages in several ML applications. For example, setting up a series of feed forward neural networks by running them independently from each other, but with a mild intermediate provision for moderation. Like the human brain, the process banks on several individual neurons to process larger tasks. As the individual networks perform their tasks independently, the results can be combined at the end to produce a synthesized, and cohesive output [89].

With an Adam Optimizer with 200 Epochs, a 3-layer Feed Forward Neural Network was formulated with a batch size of 16. After several comprehensive trials of different architectures, only the best were chosen to be presented as the final results for this approach. Care was taken to avoid any over-fitting by inherently designing the neural network. An absolute mean error of 3.99% was achieved through this approach. The results for this approach can be seen in Fig 8.7

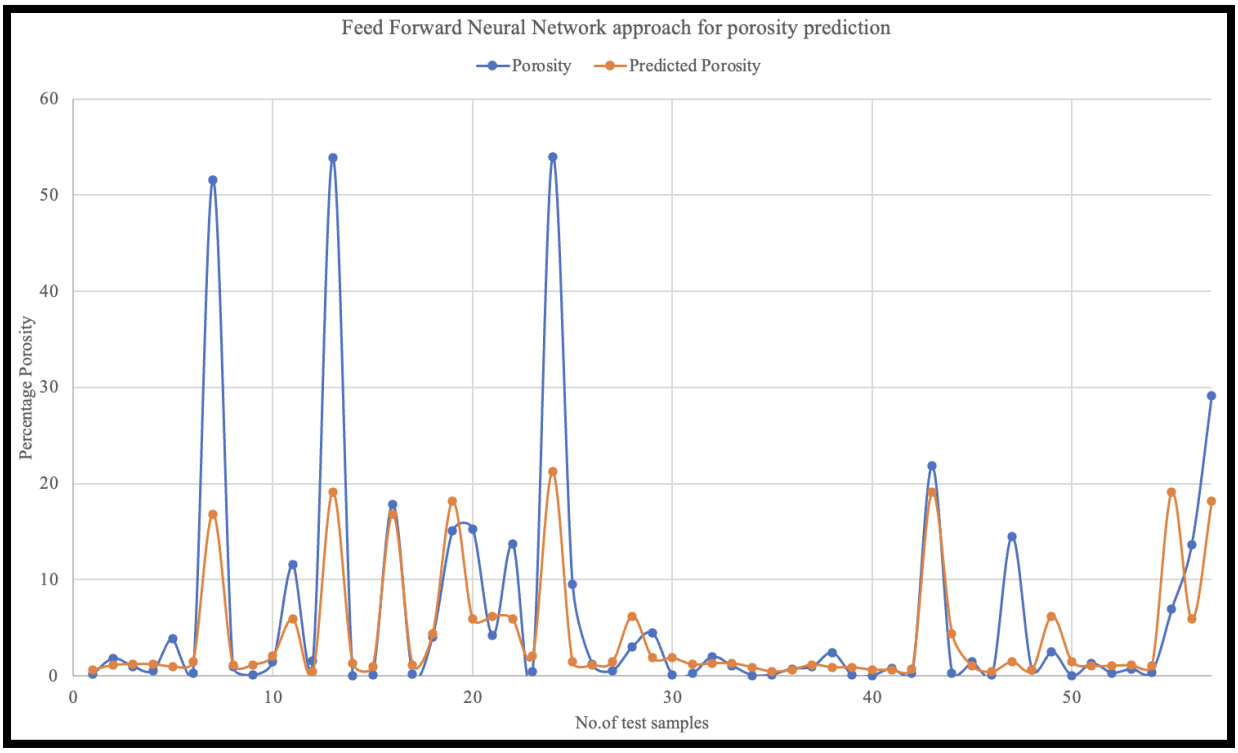

Figure 8.7: Actual porosity vs predicted porosity using Feed Forward Neural Network

8.4 Random Forest Regressors

Random Forest, a commonly used ML algorithm works on the combination of multiple decision trees to reach to a single output. The three main hyper parameters of the Random Forest algorithms that need to be set before training are the node size, number of trees and the number of features

sampled. After this is done, a random forest can either be used to address classification or regression problems.

As mentioned above, random forests are a collection of decision trees each of which is comprises of a data sample drawn from the training set with replacement, called the bootstrap sample. Of this training sample, one third is set aside as test data, also known as the out-of-bag (oob) sample. One more instance of randomness is then added through feature bagging thus allowing more diversity in the dataset and minimizing the correlation among the decision trees. Depending on the nature of the application, the determination of the prediction will vary [90].

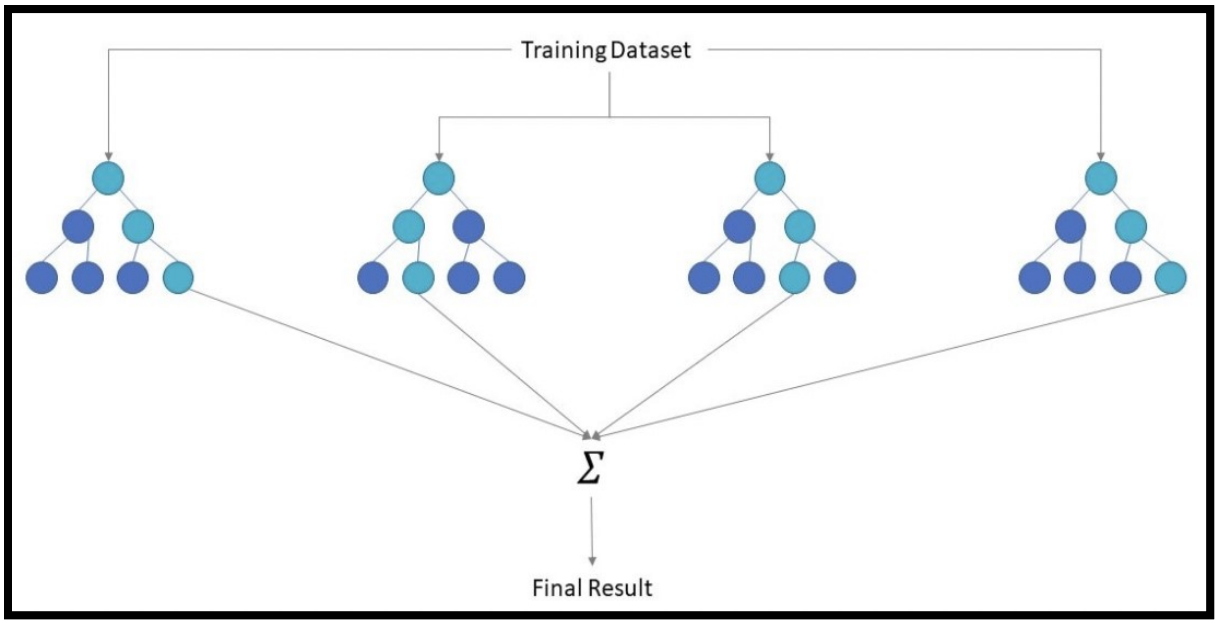

Figure 8.8: Diagram of a Random Forest Regressor [90]

Some of the benefits of running Random Forest are the reduced risk of overfitting as the robust number of trees in the random forest don't let the classifier overfit the model as the averaging number of uncorrelated decision trees lower the variance and the overall prediction error. They

provide flexibility in terms of their use for classification or regression problems and are easy to determine feature importance to the model [90].

For the Digital Twin application, a grid search was carried out to find the optimal tree parameters. Sample image of the random forest individual tree used for the Digital Twin is as shown in Fig.8.9. The predicted porosity results through a Random Forest Regressor are shown in Fig.8.10. An absolute mean error of 3.24% was obtained for this approach.

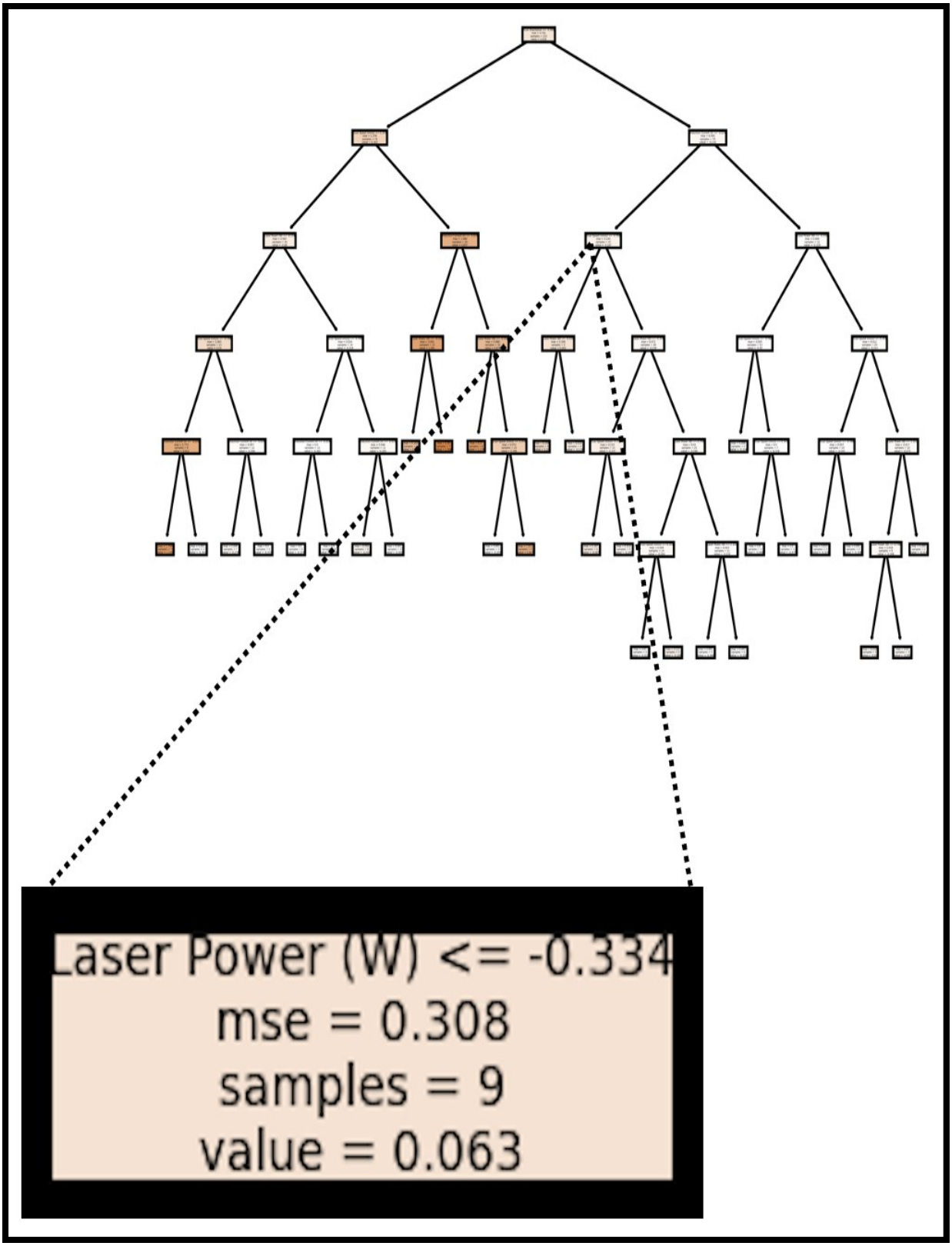

Figure 8.9: Diagram of a sample of Random Forest Individual Tree

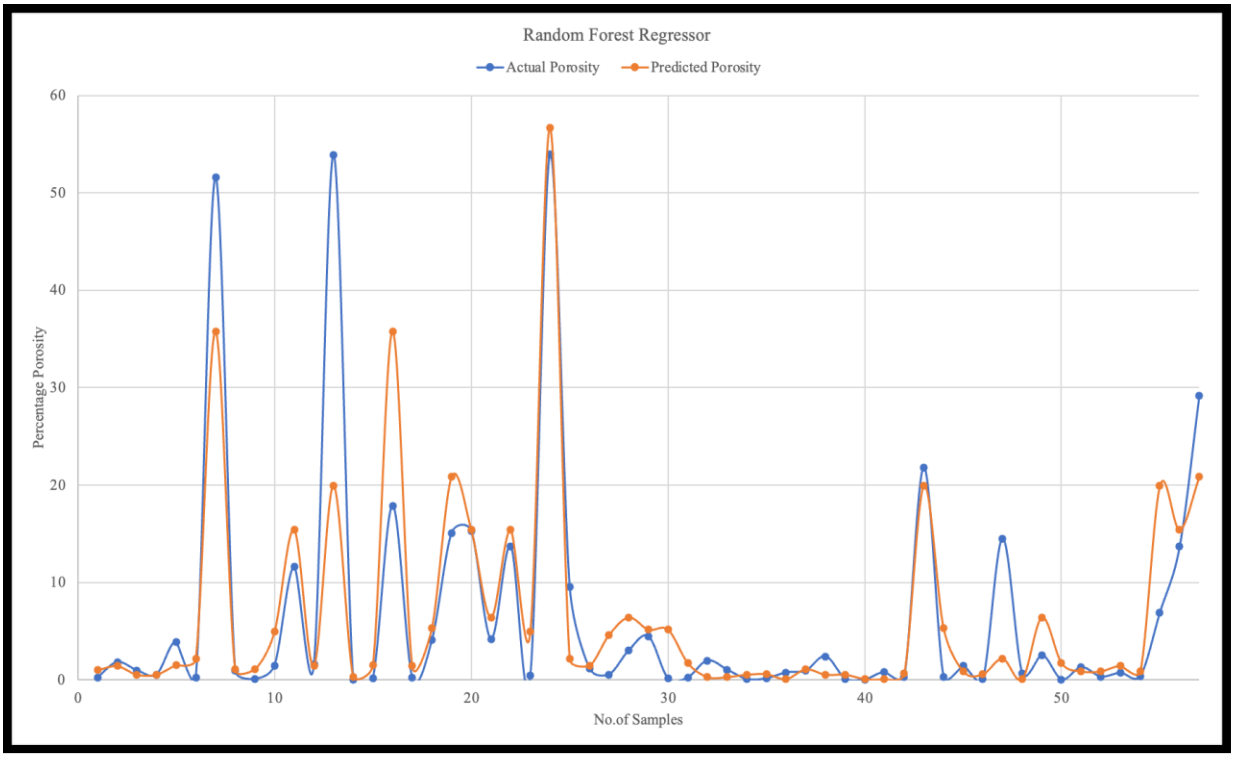

Figure 8.10: Actual porosity vs predicted porosity using a Random Forest algorithm

This concludes the initial framework of the Digital Twin by addressing four approaches for predicting the porosity. As can be seen throughout the discussion, three out of the four approaches had similar absolute mean errors while the Linear Regression models proved to have a higher error. This is given the very nature of trial of linear overfitting of the data even for non-linear relationships between the input and the output parameters. The next step for the Digital Twin is proposed in the future scope of the project. Considerable tuning of the data needs to be conducted while increasing the size of the dataset itself. This can help in addressing the uncertainty factor involved in prediction of porosity through these models.

Chapter 9. Conclusion and Future Scope

The conclusion of this proposed study could be classified in the merits of its concept and the broader impact it imposes w.r.t the potential opportunities of research it opens up. A brief discussion of each of these sections follows

9.1 Intellectual Merit

Growing demands and increasing industrial inclination towards the field of metal Additive Manufacturing in the recent years has come at a cost of more research questions in the field of its quality and process control. The transition of these research questions into effective solutions has often been with a trade-off to expensive technological advances. This study aims at addressing a few of these research questions with relatively simpler yet theoretically supported solutions. In summary, the use of an auxiliary heating source with a means to control the thermal distribution in the powder bed comes across as a much simpler approach to control and/or tailor resulting physical properties. This helps in keeping the standard layout of a typical Powder Bed Fusion Process in place with minimal changes comparatively. It also helps towards minimizing the laser dependency while not compromising in the final properties of the builds. While the quantification of its efficiency in terms of power consumption savings, reduced post-process treatments, etc. are still under works, the intellectual merit lies in its more practical approach to address concerns of

obtaining desired end-products. The addition of a ML prediction model to the concept helps in optimizing the overall process even prior to conducting any physical experiments.

9.2 Broader Impacts

Additive Manufacturing is a rapidly evolving field. With researchers trying to address different issues across different families and stages of AM, there is still more window for optimization. The scope of this study limits itself primarily to a PBF process and the use of 316SS powder as the raw material owing to the timeline chalked for the project, available resources and research inclination towards a particular family of AM given its challenges. However, the concept proposed through this study finds wider applications in terms of material usage, type of AM processes, design improvement for better efficiency and highlighting different solutions to more issues the AM field faces currently. Also, optimization of the process itself based on the data gathered through this study would help in making the concept more suitable to different applications in the field of laser processing of metals.

9.3 Manuscripts Under Preparation

The proposed study can contribute to the field of metal AM on the following topics:

Paper 1: Control of Thermal Distribution in Additive Manufacturing-An overview of the mechanism for thermal distribution in a typical AM process and the significance of its control will be proposed through an auxiliary heating technique. Modelling and numerical simulation analysis for the same will be discussed.

Paper 2: Microstructure and mechanical property control in Selective Laser Melting of metals-Process development and sample deposition for comparative analysis of properties obtained through Induction assisted Selective Laser Melting (SLM) and traditional SLM will be discussed and reviewed.

Paper 3: Porosity prediction for Selective Laser Melting of metals through Machine Learning-Use of Artificial intelligence to predict porosity and optimize process parameters through numerical data input will be discussed and reviewed.

The literature database for Additive Manufacturing keeps increasing everyday as more progress is made towards making the field of AM more reliable and consistent with its outcome. However, for all the topics addressed above, not much has been discussed and published exactly in line with the intent of the respective studies mentioned briefly under each potential publication.

9.4 Future Scope

As discussed briefly in the sections above, the study possesses great potential and window for more optimization and wider application. A few of them are discussed below.

9.4.1 Stand-alone ISLM 3D Printer

The entire span of the study was focused on generating a proof-of-concept for the use of selective induction in the L-PBF process. As a result of this, various sub-systems such as the Trumpf laser, Nachi robot, the LACS optic setup and the Pillar MK-20 system were integrated to communicate with each other in a manner that helps with the smooth working of the ISLM printer. However, the bigger goal of the project would be is to develop a desktop sized ISLM printer through a

rigorous Product Development cycle. Initial efforts have already been taken towards this. An assembly design is proposed for the manufacturing of this ISLM 3D printer as can be seen in Fig 9.1.

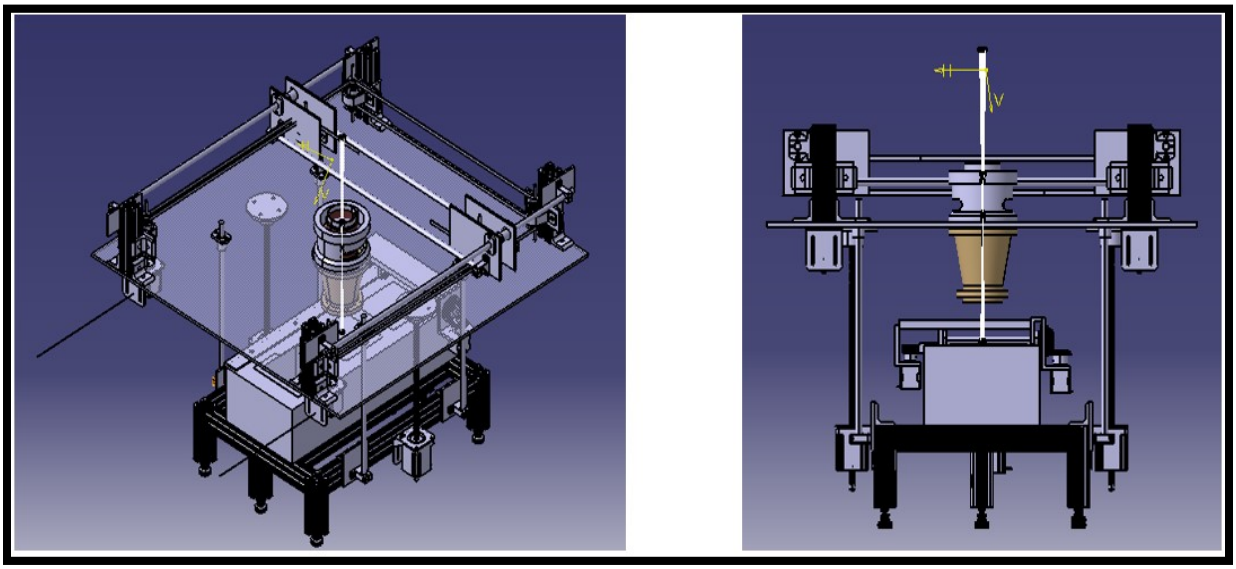

Figure 9.1: Assembly design of the desktop sized 3D printer

The proposed design uses the same geometric dimensions of the powder bed system that was used to generate the proof-of-concept for this study. The building platform dimensions being 4.5 x 4.5in the X-Y directions and 8in in the Z-direction respectively. A completely optimized lens optic setup is also proposed for the same. The entire assembly would sit in an enclosed chamber that will provide for an inert environmental working and better process control by eliminating uncertainties in the input parameters. A completely redesigned power supply system specifically designed for the ISLM system is also proposed. This would help in achieving more optimized control on the effect of induction in the building of SLM samples. Also, as can be clearly seen that the scanning patterns define the output of the ISLM process, different orientations and scanning strategies need to be tested to study an in-depth effect of the proposal on standard SLM processes.

9.4.2 ISLM Add-on Nozzle

The very of the study lies in the efficient design of the ISLM nozzle that regulates the resulting properties of the builds. The ISLM nozzle also finds great potential as an addition kit to already existing systems across different families of Additive Manufacturing processes. One such nozzle design was proposed for the Direct Metal Deposition process for the POM DMD 105D system at use in the Additive Manufacturing Processes Laboratory at the University of Michigan-Dearborn. The design proposal makes use of the standard setup of the system by making small modifications to it. A visual representation for the same can be seen in Fig 9.2.

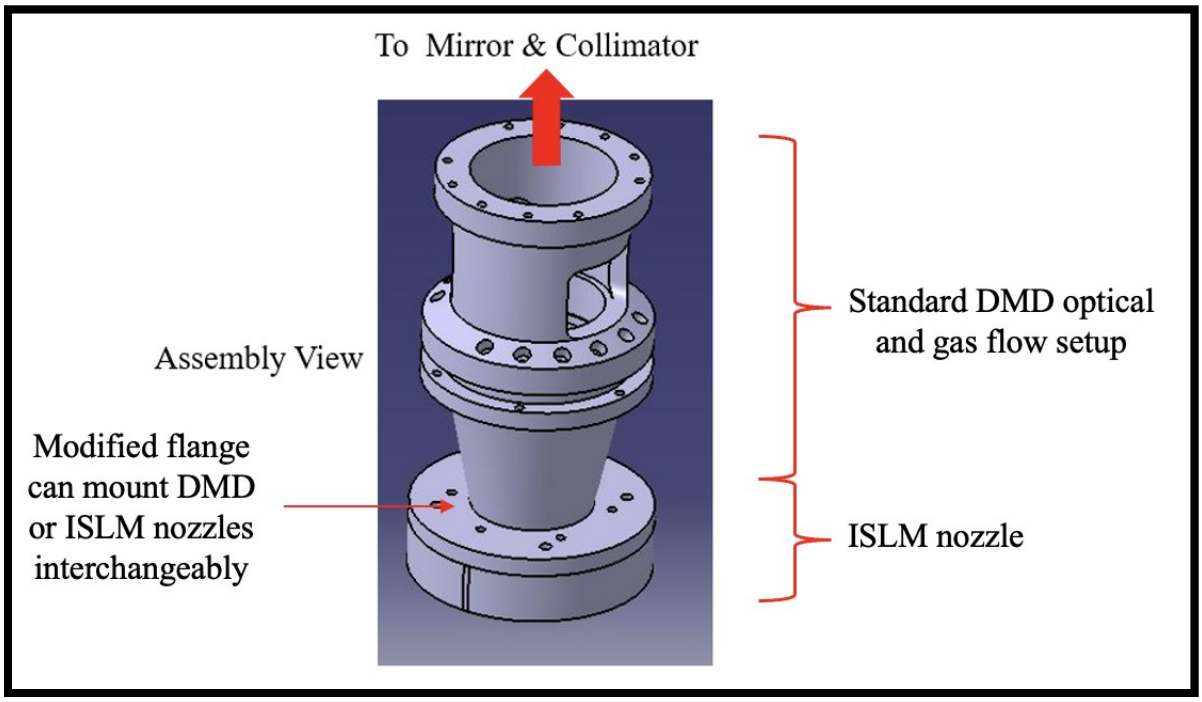

Figure 9.2: Assembly design view of the DMD ISLM nozzle setup

9.4.3 ISLM Coil

The coil design for the ISLM was confined to a simpler geometry for its ease of use. However, various other iterations and geometries were tried as a part of the coil design optimization. Depending on the application, more research can be carried out w.r.t this aspect of the coil design. Moreover, the use of field shapers can also be incorporated to simplify the coil design and magnify the effect of induction to much smaller Heat Affected Zones. Some of the early testing of such field shapers can be seen through Fig 9.3 and Fig 9.4 respectively.

Figure 9.3: Field shaper design (left) and fabricated field shaper for ISLM coil (right)

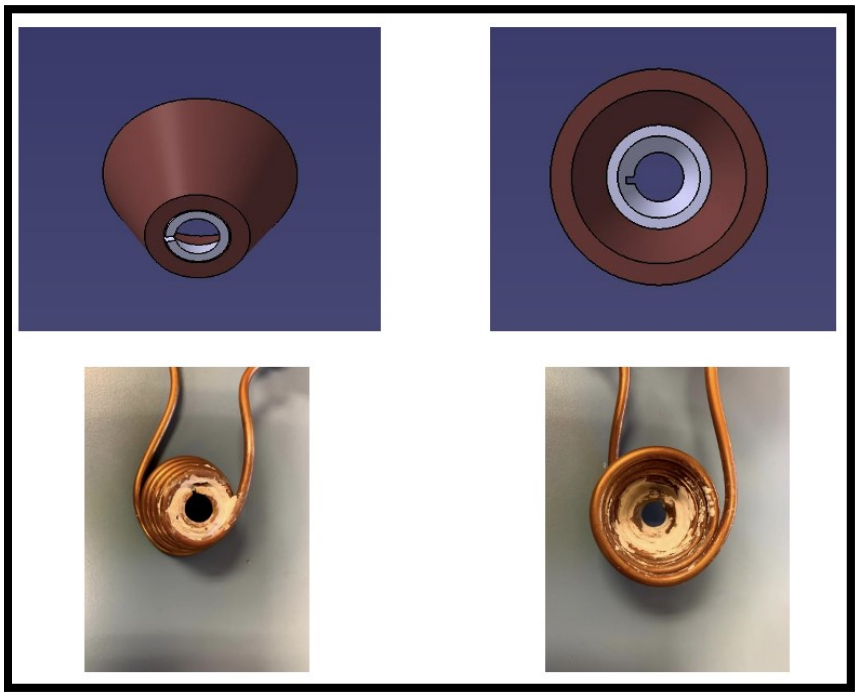

Figure 9.4: Field shaper design with the ISLM coil (top) and fabricated field shaper cured to the ISLM coil with a ceramic adhesive (bottom)

9.4.4 ISLM Material Applications

The entire scope of the study was confined to SS 316 given the wider applications of the alloy in the field of AM and the easy availability of the starting raw material for the process. The coil design also revolved around this material system. However, with the advent of the AM, the field is witnessing an ever-growing adaption of the technology to different material systems and their applications. Metals like Copper, Aluminum, Titanium and their alloys have been a subject of research interest in metal AM. As a part of the future research scope, advancements could be made in the system and design optimization of ISLM so that popular AM metals could be put to test.

9.4.5 ISLM Digital Twin

The study rather provides a roadmap and initial efforts towards building a more robust digital replica focusing towards the betterment of the ISLM system as a whole. The primary limitation of the Digital Twin is the limited dataset to tune the model for a more reliable output. With a more comprehensive experimental data achieved as a part of a dedicated design of experiments specifically for the Digital Twin, complex factors can be added to the data pool to better refine the output of the system. These additions could be testing of the deposits at various Induction currents and different scan strategies, different coil geometries, different material applications, etc.

9.4.6 Laser Beam Profiles and Their Integration with ISLM

While the choice of laser system for the study and development of ISLM was confined to a Gaussian beam profile, the variation of the lower order Transverse Mode (TEM_{00}) selected for the emission of the laser (non-Gaussian Beam profiles) also regulate and can play an important role in the thermal distribution of the powder bed fusion process system. This future scope of the study for the ISLM system also lies in determining the end-result effects of these changes in the primary energy source after its integration with the ISLM nozzle in terms of the evolution of the microstructure in the built components. This opens up an entirely new area of application for the ISLM system and the significant advantages it brings along.

9.5 Outcome of the Study

The intent of the study has been to enhance an already advanced manufacturing technique for better reliability and consistency. The major highlights and outcomes of this study can be noted as follows:

1. A functional application specific induction coil design.
2. Process development and assembly of Induction assisted Selective Laser Melting (ISLM) system.
3. Parameter optimization for ISLM and data generation for ML model training and testing.
4. Comparative analysis of laser deposited (PBF-SLM) samples with ISLM samples.
5. Machine learning model buildup for ISLM and PBF processes.
6. Study of the effect of induction assisted SLM on the microstructure of deposited samples and resulting physical properties.
7. Potential opportunities for application of a designed induction system to different families of metal Additive Manufacturing.

Bibliography

[1] "Standard Terminology for Additive Manufacturing – General Principles – Terminology," ISO, 2021.

[2] D. Wetzel, "Additive or Subtractive prototyping: Which is best?," [Online]. Available: https://www.protomatic.com/additive-or-subtractive-prototyping-which-is-best-2. [Accessed 04 March 2022].

[3] B. Berman, "3-Dprinting:The new industrial revolution," *Business Horizons,* vol. 55, no. 2, pp. 155-162, 2012.

[4] I. Yadroitsev, I. Yadroitsava, A. Plessis and E. MacDonald, Fundamentals of Laser Powder Bed Fusion of Metals, Additive Manufacturing Materials and Technologies, 2021.

[5] Y. Shi, C. Yan, Z. Yan, J. Wu, Y. Wang, S. Yu and Y. Chen, Materials for Additive Manufacturing, Academic Press, 2021.

[6] "The History of 3D Printing," All That 3D, [Online]. Available: https://www.allthat3d.com/3d-printing-history/. [Accessed 04 03 2022].

[7] V. Bhavar, P. Kattire, V. Patil, S. Khot , K. Gujar and R. Singh, "A review on powder bed fusion technology of metal additive manufacturing," in *4th International conference and exhibition on Additive Manufacturing Technologies-AM-2014*, Bangalore, 2014.

[8] J.-P. Kruth, G. Levy, R. Schindel, T. Craeghs and E. Yasa, "Consolidation of Polymer Powders by Selective Laser Sintering," in *Proceedings of the 3rd international conference on polymers and moulds innovations*, 2008.

[9] S. Kumar, "Selective laser sintering: A qualitative and objective approach," *The Journal of The Minerals, Metals & Materials Society,* vol. 55, pp. 43-47, 2003.

[10] Y. Shen, D. Gu and Y. Pan, "Balling Process in Selective Laser Sintering 316 Stainless Steel Powder," *Key Engineering Materials,* Vols. 315-316, pp. 357-360, 2006.

[11] I. Yadroitsev, I. Yadroitsava and A. Plessis, "Basics of Laser Powder Bed Fusion," in *Fundamentals of Laser Powder Bed Fusion of metals*, Additive Manufacturing Materials and Technologies, 2021, pp. 15-38.

[12] J. Kruth, G. Levy, F. Klocke and T. Childs, "Consolidation phenomena in laser and powder-bed based layered manufacturing," *CIRP Annals Manufacturing Technology,* vol. 56, no. 2, pp. 730-759, 2007.

[13] S. P. Edwardson, J. Griffiths, G. Dearden and K. Watkins, "Temperature Gradient Mechanism: Overview of the Multiple Pass Controlling Factors," *Physics Procedia,* vol. 5, pp. 53-63, 2010.

[14] C. Yap, C. Chua, Z. Dong, Z. Liu, D. Zhang, L. Loh and S. Sing, "Review of selective laser melting: Materials and applications:," *Applied Physics Reviews,* vol. 2, 2015.

[15] B. Vrancken, "Study of Residual Stresses in Selective Laser Melting," Ph.D. dissertation, KU Leuven, Leuven, 2016.

[16] A. Dezfoli, W. Hwang, W. Huang and T. Tsai, "Determination and controlling of grain structure of metals after laser incidence: Theoretical approach," *Scientific Reports,* 2017.

[17] P. Krakhmalev and N. Kazantseva, "Microstructure of L-PBF alloys," in *Fundamentals of Laser Powder Bed Fusion of Metals*, Additive Manufacturing Materials and Technologies, 2021, pp. 215-243.

[18] R. Visveswaran, "Microstructural characterization of Thin and Thick directional Ti-6Al-4V structures using Laser Deposition Process," M.S.thesis, Dept. Mech. Eng., University of Michigan-Dearborn, Dearborn, 2011.

[19] K. Saeidi, "Stainless steels fabricated by laser melting," Department of Materials and Environmental Chemistry, Sweden, 2016.

[20] Outokumpu, *Outokumpu Handbook of stainless steel*, 2013.

[21] P. Bajaj, A. Hariharan, A. Kini, P. Kurnsteiner, D. Raabe and E. Jagle, "Steels in additive manufacturing: A review of their microstructure and properties," *Materials Science and Engineering,* vol. 772, 2019.

[22] J. Dong, Z. Zhao, J. Cui, F. Yu and C. Ban, "Effect of low-frequency electromagnetic casting on the castability, microstructure, and tensile properties of direct-chill cast Al-Zn-Mg-Cu alloy," *Journal of Metallurgical and materials transactions A,* vol. 35, pp. 2487-2494, 2004.

[23] J. Shouxun, Q. Ma and Z. Fan, "Semisolid Processing Characteristics of AM Series Mg Alloys by Rheo-Diecasting," *Metallurgical and Materials Transactions A,* vol. 37A, no. 3, pp. 779-787, 2006.

[24] T. Atamanenko, D. Eskin, L. Zhang and L. Katgerman, "Criteria of Grain Refinement Induced by Ultrasonic Melt Treatment of Aluminum Alloys Containing Zr and Ti," *Metallurgical and Materials Transactions A,* vol. 41, pp. 2056-2066, 2010.

[25] D. Zhang, A. Prasad, M. Bermingham, C. Todaro, M. Benoit, M. Patel, D. StJohn and M. Easton, "Grain Refinement of Alloys in Fusion-Based Additive Manufacturing Processes," *Metallurgical and Material Transactions,* vol. 51, pp. 4341-4359, 2020.

[26] O. Rios, W. Carter and S. Ulrich, "Additive Manufacturing Consolidation of Low-Cost Water Atomized Steel Powder Using Micro-Induction Sintering," U.S Department of Energy Office of Scientific and Technical Information, 2018.

[27] W. Huang, C. Chuang, C. Lin, C. Wu, D. Lin, S. Liu, W. Tseng and J. Horng, "Microstructure-controllable laser additive manufacturing process for metal products," in *8th International Conference on Photonic Technologies LANE*, 2014.

[28] A. Jones, "ThoughtCo.," 07 July 2019. [Online]. Available: https://www.thoughtco.com/electromagnetic-induction-2699202.

[29] Fives Group, "Fives Group," [Online]. Available: http://induction.fivesgroup.com/our-expertise/induction-heating/the-concept-of-induction-heating.html. [Accessed 04 03 2022].

[30] V. Rudnev, D. Loveless, M. Black and R. Cook, Handbook of Induction Heating, CRC Press, 2017.

[31] Fluxtrol, "Alphaform MF," [Online]. Available: https://fluxtrol.com/alphaform-MF. [Accessed 19 07 2018].

[32] H. Flesch and J. Mottin, "Sintering and Laser Fusion Device, comprising a means for heating powder by induction". United States of America Patent US 9,616,458 B2, 17 07 2018.

[33] M. Alimardani, V. Fallah, A. Khajepour and E. Toyerskani, "The effect of localized dynamic surface preheating in laser cladding of Stellite 1," *Surface and Coatings Technology,* vol. 204, no. 23, pp. 3911-3919, 2010.

[34] L. Caprio, A. Demir, G. Chiari and B. Previtali, "Defect-free laser powder bed fusion of Ti–48Al–2Cr–2Nb with a hightemperature inductive preheating system," *Journal of Physics:Photonics,* vol. 2, 2020.

[35] S. Zinn and S. Semiatin, "Coil design and fabrication:basic design and modifications," *Physics,* 1988.

[36] C. Nataraj, S. Khan and M. Habaebi, "Coil geometry models for power loss analysis and hybrid inductive link for wireless power transfer applications," *Sadhana,* vol. 43, 2018.

[37] Fluxtrol, "Fluxtrol Alphaform," Fluxtrol, [Online]. Available: https://fluxtrol.com/alphaform-MF. [Accessed 28 02 2022].

[38] Trumpf, Trumpf TruDisk 3302 Operator Manual, Trumpf.

[39] P. Induction, Pillar MK-20 Operator Manual, Pillar Induction.

[40] T. M. Powders, "Additive Manufacturing Powders by TruForm Metal Powders," TruForm Metal Powders, [Online]. Available: https://www.praxairsurfacetechnologies.com/en/materials-and-equipment/materials/additive-manufacturing-powders/?tab=truform-product-portfolio. [Accessed 04 03 2022].

[41] E. Liverani, S. Toschi, L. Ceschini and A. Fortunato, "Effect of selective laser melting (SLM) process parameters on microstructure and mechanical properties of 316L austenitic stainless steel," *Journal of Materials Processing Technology,* vol. 249, pp. 255-263, November 2017.

[42] M. Lodhi, K. Deen and W. Haider, "Corrosion behavior of additively manufactured 316L stainless steel in acidic media," *Materialia,* vol. 2, pp. 111-121, 2018.

[43] K. Saeidi, X. Gao, Y. Zhong and Z. Shen, "Hardened austenite steel with columnar sub-grain structure formed by laser melting," *Materials Science and Engineering: A,* vol. 625, pp. 221-229, 2015.

[44] Z. Sun, X. Tan, S. Tor and W. Yeong, "Selective laser melting of stainless steel 316L with low porosity and high build rates," *Materials & Design,* vol. 104, pp. 197-204, 2016.

[45] S. Leuders, M. Thone, A. Riemer, T. Niendorf, T. Troster, H. Richard and H. Maier, "On the mechanical behaviour of titanium alloy TiAl6V4 manufactured by selective laser melting: Fatigue resistance and crack growth performance," *International Journal of Fatigue,* vol. 48, pp. 300-307, 2012.

[46] Y. Kok, X. Tan, S. Tor and C. Chua, "Fabrication and microstructural characterisation of additive manufactured Ti-6Al-4V parts by electron beam melting," *Virtual and Physical Prototyping 10th Anniversary,* vol. 10, no. 1, pp. 13-21, 2015.

[47] V. Varadaraajan, "Development of a novel iron-manganese alloy and its application," Ph.D. dissertation, Dept. Mech. Eng., University of Michigan-Dearborn, Dearborn, 2015.

[48] Prevey, P.S; Hornbach, D.J, "X-Ray Diffraction Residual Stress Techniques," in *Metals Handbook*, Cleveland, American Society for Metals, 1986, pp. 380-392.

[49] Z. Sun, X. Tan, S. Tor and W. Yeong, "Selective laser melting of stainless steel 316L with low porosity and high build rates," *Materials & Design,* vol. 104, pp. 197-204, 2016.

[50] K. Saeidi, L. Kvetkova, F. Lofaj and Z. Shen, "Austenitic stainless steel strengthened by the in situ formation of oxide nanoinclusions," *RSC Advances,* no. 27, 2015.

[51] M. Kamariah, W. Harun, N. Khalil, F. Ahmad, M. Ismail and S. Sharif, "Effect of heat treatment on mechanical properties and microstructure of selective laser melting 316L stainless steel," in *4th International Conference on Mechanical Engineering Research, ICMER 2017*, Kuantan, Pahang, Malaysia, 2017.

[52] W.-S. Shin, B. Son, W. Song, H. Sohn, H. Jang, Y.-J. Kim and C. Park, "Heat treatment effect on the microstructure, mechanical properties, and wear behaviors of stainless steel 316L prepared via selective laser melting," *Materials Science and Engineering,* vol. 806, 2021.

[53] A. Yadollahi, N. Shamsaei, S. Thompson and D. Seely, "Effects of process time interval and heat treatment on the mechanicaland microstructural properties of direct laser deposited 316L stainless steel," *Materials Science & Engineering: A,* vol. 644, pp. 171-183, 2015.

[54] L. Darken, R. Gurry and M. Bever, Physical Chemistry of Metals, New York: McGraw-Hill Book Company, 1953.

[55] Q. Chao, V. Cruz, S. Thomas, N. Birbilis, P. Collins, A. Taylor, P. Hodgson and D. Fabijanic, "On the enhanced corrosion resistance of a selective laser melted austenitic stainless steel," *Scripta Materialia,* vol. 141, pp. 94-98, 2017.

[56] G. Sander, S. Thomas, V. Cruz, M. Jurg, N. Birbilis, X. Gao, M. Brameld and C. Hutchinson, "On The Corrosion and Metastable Pitting Characteristics of 316L Stainless Steel Produced by Selective Laser Melting," *Journal of the Electrochemical Society,* vol. 164, 2017.

[57] M. Lodhi, K. Deen, Z. Rahman, A. Farooq and W. Haider, "Electrochemical characterization and thermodynamic tendency of β-Lactoglobulin adsorption on 3D printed stainless steel," *Journal of Engineering and Chemistry,* vol. 65, pp. 180-187, 2018.

[58] K. Kakaei, M. Esrafili and A. Ehsani, "Graphene and Anticorrosive Properties," in *Graphene Surfaces-Particles and Catalysts*, Academic Press, 2019, pp. 303-337.

[59] J. Elmer, S. Allen and T. Eagar, "Microstructural development during solidification of stainless steel alloys," *Metallurgical Transactions A,* vol. 20, pp. 2117-2131, 1989.

[60] J. Brooks, M. Baskes and F. Greulich , "Solidification modeling and solid-state transformations in high-energy density stainless steel welds," *Metallurgical Transactions A,* vol. 22, pp. 915-926, 1991.

[61] H. Yu, J. Yang, J. Yin, Z. Wang and X. Zeng, "Comparison on mechanical anisotropies of selective laser melted Ti-6Al-4V alloy and 304 stainless steel," *Materials Science and Engineering: A,* vol. 695, pp. 92-100, 2017.

[62] E. Yasa and J. Kruth, "Microstructural investigation of Selective Laser Melting 316L stainless steel parts exposed to laser re-melting," *Procedia Engineering,* vol. 19, pp. 389-395, 2011.

[63] J. Suryawanshi, K. Prashanth and U. Ramamurty, "Mechanical behavior of selective laser melted 316L stainless steel," *Materials Science and Engineering A,* vol. 696, pp. 113-121, 2017.

[64] Y. Zhong, L. Liu, S. Wikman, D. Cui and Z. Shen, "Intragranular cellular segregation network structure strengthening 316L stainless steel prepared by selective laser melting," *Journal of Nuclear Materials,* vol. 470, pp. 170-178, 2016.

[65] B. Blinn, M. Klein, C. Glabner, M. Smaga, J. Aurich and T. Beck, "An investigation of the microstructure and fatigue behavior of additively manufactured AISI 316L stainless steel with regard to the influence of heat treatment," *Additive Manufacturing of Ferrous Materials,* vol. 8, no. 4, 2018.

[66] A. Riemer, S. Leuders, M. Thone, R. H.A., T. Troster and T. Niendorf, "On the fatigue crack growth behavior in 316L stainless steel manufactured by selective laser melting," *Engineering Fracture Mechanics,* vol. 120, no. 2014, pp. 15-25, 2014.

[67] T. Niendorf, S. Leuders, A. Riemer, H. Richard, T. Troster and D. Schwarze, "Highly anisotropic steel processed by selective laser melting," *Metallurgical and Materials Transactions B,* vol. 44, pp. 794-796, 2013.

[68] S. Gorsse, C. Hutchinson, M. Goune and R. Banerjee, "Additive manufacturing of metals: a brief review of the characteristic microstructures and properties of steels, Ti-6Al-4V and high-entropy alloys," *Engineering and Structural Materials,* pp. 584-610, 2017.

[69] C. Todaro, M. Easton, D. Qiu, D. Zhang, M. Bermingham, E. Lui, M. Brandt, D. StJohn and M. Qian, "Grain structure control during metal 3D printing by high-intensity ultrasound," *Nature Communications,* vol. 11, 2020.

[70] D. Zhang, A. Prasad, M. Bermingham, C. Todaro, M. Benoit, M. Patel, D. StJohn and M. Easton, "Grain Refinement of Alloys in Fusion-Based AdditiveManufacturing Processes," *The Minerals, Metals & Materials Society and ASM International,* 2020.

[71] W. Kurz and D. Fisher, Fundamentals of Solidification, Trans Tech Publications, 1986.

[72] C. Todaro, M. Easton, D. Qiu, M. Brandt, D. StJohn and M. Qian, "Grain refinement of stainless steel in ultrasound-assisted additive manufacturing," *Additive Manufacturing,* vol. 37, no. 101632, 2021.

[73] M. Gremaud, M. Carrard and W. Kurz, "The microstructure of rapidly solidified Al-Fe alloys subjected to laser surface treatment," *Acta Metallurgica et Materilia,* vol. 38, no. 12, pp. 2587-2599, 2003.

[74] G. Tapia and A. Elwany, "A Review on Process Monitoring and Control in Metal- Based Additive Manufacturing," *Journal of Manufacturing Science and Engineering,* vol. 136, no. 6, 2014.

[75] L. Meng, B. McWilliams, W. Jarosinski, H.-Y. Park, Y.-G. Jung, J. Lee and J. Zhang, "Machine Learning in Additive Manufacturing: A Review," *The Journal of Minerals, Metals & Materials Society,* vol. 72, pp. 2363-2377, 2020.

[76] X. Qi, G. Chen, Y. Li, X. Cheng and L. Changpeng, "Applying Neural- Network-Based Machine Learning to Additive Manufacturing: Current Applications, Challenges, and Future Perspectives," *Engineering,* vol. 5, no. 4, pp. 721-729, 2019.

[77] P. Dhage, "Predicting porosity and microstructure of 3D printed part using Machine Learning," M.S.thesis, Dept. Mech. Eng., University of Michigan-Dearborn, Dearborn, 2020.

[78] . J. Brownlee, "No Free Lunch Theorem for Machine Learning," 17 February 2021. [Online]. Available: https://machinelearningmastery.com/no-free-lunch-theorem-for-machine-learning/. [Accessed 7 March 2022].

[79] C. Wang, X. Tan, E. Liu and S. Tor, "Process parameter optimization and mechanical properties for additively manufactured stainless steel 316L parts by selective electron beam melting," *Materials & Design,* vol. 147, no. 5, pp. 157-166, 2018.

[80] E.O.Olakanmi, R.F.Cochrane and K.W.Dalgarno, "Densification mechanism and microstructural evolution in selective laser sintering of Al–12Si powders," *Journal of Material Processing and Technology,* vol. 211, no. 1, pp. 113-121, 2011.

[81] C. Wang, X. Tan, Z. Du, S. Chandra, Z. Sun, C. Lim, S. Tor, C. Lim and C. Wong, "Additive manufacturing of NiTi shape memory alloys using pre-mixed powders," *Journal of Material Processing and Technology,* vol. 271, pp. 152-161, 2019.

[82] M. Mozaffar, A. Paul, R. Al-Bahrani, S. Wolff, A. Choudhary, A. Agrawal, K. Ehmann and J. Cao, "Data-driven prediction of the high-dimensional thermal history in directed energy deposition processes via recurrent neural networks," *Manufacturing Letters,* vol. 18, pp. 35-39, 2018.

[83] C. Wang, X. Tan, S. Tor and C. Lim, "Machine learning in additive manufacturing: State-of-the-art and perspectives," *Additive Manufacturing,* vol. 36, no. 101538, 2020.

[84] G. Tapia, S. Khairallah, M. Matthews, W. King and A. Elwany, "Gaussian process-based surrogate modeling framework for process planning in laser powder-bed fusion additive manufacturing of 316L stainless steel," *International Journal of Advanced Manufacturing Technology,* vol. 94, pp. 3591-3603, 2017.

[85] K. Aoyagi, H. Wang, S. Sudo and A. Chiba, "Simple method to construct process maps for additive manufacturing using a support vector machine," *Additive Manufacturing,* vol. 27, pp. 353-362, 2019.

[86] K. Bailey, "Gaussian Processes for Dummies," 9 August 2016. [Online]. Available: https://katbailey.github.io/post/gaussian-processes-for-dummies/. [Accessed 08 March 2022].

[87] K. Bailey, "From both sides now: the math of linear regression," 2 June 2016. [Online]. Available: https://katbailey.github.io/post/from-both-sides-now-the-math-of-linear-regression/#fn:calculusfootnote. [Accessed 8 March 2022].

[88] R. Quiza and J. Davim, "Computational methods and optimization," in *Machining of Hard Materials*, 2011, pp. 3-4.

[89] "Feed Forward Neural Network," [Online]. Available: https://deepai.org/machine-learning-glossary-and-terms/feed-forward-neural-network. [Accessed 08 March 2022].

[90] IBM Cloud Education, "Random Forest," 07 December 2020. [Online]. Available: https://www.ibm.com/cloud/learn/random-forest. [Accessed 08 March 2022].

[91] O. Rios, W. Carter and S. Ulrich, "Additive Manufacturing Consolidation of Low-Cost Water Atomized Steel Powder Using Micro-Induction Sintering," U.S Department of Energy Office of Scientific and Technical Information, 2018

[92] C. Nataraj, S. Khan and M. H. Habaebi, "Coil geometry models for power loss analysis and hybrid inductive link for wireless power transfer applications," *Sadhana*, vol. 43, pp. 1-11, 2018.

[93] I. Baturynska, O. Semeniuta and K. Martinsen, "Optimization of process parameters for powder bed fusion additive manufacturing by combination of machine learning and finite element method: A conceptual framework," in *IRP Conference on Intelligent Computation in Manufacturing Engineering*, 2017.

[94] R. Haimbaugh, Practical Induction Heat Treating, ASM International, 2015.

[95] D. Herzog, V. Seyda, E. Wycisk and C. Emmelmann, "Additive Manufacturing of Metals," *Acta Materialia,* p. 22, 2016.

[96] K. Hoejin, Y. Lin and T.-L. Tseng, "A review on quality control in Additive Manufacturing," *Rapid Prototyping Journal,* vol. 24, no. 3, 2018.

[97] D. Rosen, B. Stucker and I. Gibson, Additive Manufacturing Technologies 3D Printing, Rapid Prototyping, and Direct Digital Manufacturing, Springer, 2010.

[98] P.-N. Tan, M. Steinbach, A. Karpatne and V. Kumar , Introduction to Data Mining (Second Edition), Pearson, 2005.